

Designing self-assembly Routes to colloidal gyroids

By

Wesley Flavell

A thesis submitted to
the University of Birmingham
for the degree of
DOCTOR OF PHILOSOPHY

School of Chemistry
College of Engineering and Physical Sciences
University of Birmingham
September 2022

UNIVERSITY OF
BIRMINGHAM

University of Birmingham Research Archive

e-theses repository

This unpublished thesis/dissertation is copyright of the author and/or third parties. The intellectual property rights of the author or third parties in respect of this work are as defined by The Copyright Designs and Patents Act 1988 or as modified by any successor legislation.

Any use made of information contained in this thesis/dissertation must be in accordance with that legislation and must be properly acknowledged. Further distribution or reproduction in any format is prohibited without the permission of the copyright holder.

ABSTRACT

Colloidal self-assembly has shown great potential as a bottom-up route to the fabrication of functional materials. An area of focus in this regard is the self-assembly of 3D photonic crystals which operate in the visible region of the spectrum. To this end, there has been much work on devising self-assembly routes to cubic diamond-related structures, since they possess some of the largest known 3D photonic band gaps. Largely ignored in this respect, is the single network gyroid structure, which also possesses a large 3D photonic band gap as well as offering additional applications relating to its chirality. Despite its natural appearances, the direct self-assembly of a single gyroid structure remains elusive.

In this thesis, a reverse engineering approach is employed in order to transform the single network gyroid structure into single gyroid colloidal crystal structures built from discrete spherical building blocks. In this approach, the three-fold connectivity of the network is encoded into triblock patchy spheres with two equal-size circular patches. Crystal structure prediction for triblock patchy particles *via* the basin-hopping technique, then identifies what this thesis refers to as the "single colloidal gyroid" crystal, in addition to a library of competing trimer-based colloidal crystal structures. Monte Carlo simulations demonstrate, however, that these triblock patchy particles with circular patches are inadequate to self-assemble a single colloidal gyroid crystal. A method of crystal structure selection is then devised based on encoding the selective formation of specific inter-trimer dihedral angles into synthetically reasonable building blocks *via* the use of rectangular patch coverages at controlled relative orientations. A pair potential is developed in order to model the inter-

actions between such patchy particles. Monte Carlo simulations of these designer chiral patchy spheres then demonstrate the enantiomorphic self-assembly of single colloidal gyroid for a wide parameter space. Alternatively, patchy particles of a fundamentally similar design with four circular patches are also shown to self-assemble single colloidal gyroid *in silico*. Further simulations demonstrate that both routes are robust, and it is established that an appropriate selection of target patch parameters yields an impressive tolerance for patch dispersity in both coverage and orientation – lending these bottom-up routes to the prospect of experimental realisation. Finally, self-assembly routes to double colloidal gyroid crystals are established *in silico*, employing racemic mixtures of chiral patchy particles with modified interaction matrices.

ACKNOWLEDGEMENTS

Firstly, I gratefully thank my supervisors Dr Dwaipayan Chakrabarti and Prof Tim Albrecht for their guidance and support. Tim has helped shape this work for the better by providing an alternative perspective. Additionally, this thesis would simply not exist without Dwaipayan, who saved me from a life of lab work with his excellent undergraduate courses. It has been a pleasure to work with you both.

General thanks also go to members of the Chakrabarti, Albrecht, and Johnston groups past and present. Of note: (This) John Hey for his Python support, and company in the office after hours; Dr (Mr) James Shaw for his guidance during the start of my PhD, and perhaps more importantly his frequent supply of cake for the office; Dr Christopher Avins (san) for our many enjoyable arguments, and for ensuring I was always topped up with perfectly brewed lukewarm water; Andreas Neophytou for our frequent discussions throughout my PhD, and for remaining reasonably calm while I try to convey my thoughts; Jay Morris for his free regional translation services (also still up for that fight if you want it); and Helen Abbott for putting up with my antics, and introducing me to someone very special.

I would like to thank Andreas Neophytou again for in-depth discussions relating to the development of the pair potential for particles with rectangular patches, and for carrying out the photonics calculations for single colloidal gyroid (not included in this thesis), which the manuscript titled "Programmed Self-Assembly of Single Colloidal Gyroid for Chiral Photonic Crystals" benefits greatly from.

I thank the EPSRC and the School of Chemistry for funding.

And finally, I must thank Pardis for her loving support.

PUBLICATIONS

(as of 6$^{\text{th}}$ March 2023)

- "Programmed Self-Assembly of Single Colloidal Gyroid for Chiral Photonic Crystals" Wesley Flavell, Andreas Neophytou, Angela Demetriadou, Tim Albrecht & Dwaipayan Chakrabarti, *Advanced Materials*, https://doi.org/10.1002/adma.202211197 (2023).

- "Programmed Self-Assembly of Alternating and Double Gyroid Crystals from Patchy Particles" Wesley Flavell, Tim Albrecht & Dwaipayan Chakrabarti, (*Manuscript in preparation*).

Contents

Page

1 Introduction **1**

1.1 Colloidal self-assembly 1

1.2 3D photonic crystal structures 2

1.3 Patchy colloidal building blocks 4

1.4 Targeted self-assembly of colloidal open crystals 11

1.5 Gyroid structures and their fabrication 17

1.6 Thesis outline 19

2 Methodology **20**

2.1 Models 20

2.1.1 Kern-Frenkel 20

2.1.2 Continuous patchy pair potential 22

2.2 Basin-hopping global optimisation 23

2.2.1 Crystal structure prediction 25

2.3 Monte Carlo simulations 26

2.4 Bonding analysis 27

2.4.1 Constructing bonding graphs 27

2.4.2 Trigonal unit identification 30

2.4.3 Dihedral angle analysis 31

2.4.4 Rings 33

2.5 Steinhardt order parameters 33

3 Reverse Engineering Single Network Gyroid & a Library of Trimer-Based Colloidal Open Crystals 35

3.1 Introduction 35

3.2 Results and discussion 37

3.2.1 Reverse engineering single network gyroid 37

3.2.2 Corner-shared trimer crystal structures 39

3.2.2.1 Colloidal gyroid and double colloidal gyroid 40

3.2.2.2 Kagome 42

3.2.2.3 Fddd 43

3.2.2.4 Cccm 44

3.2.2.5 C2/m 44

3.2.3 Analogous crystal structures 45

3.2.4 Monte Carlo simulations 46

3.3 Conclusions 50

4 Developing a Pair Potential for Spheres With Rectangular Patches & Investigating Their Self-Assembly 51

4.1 Introduction 51

4.2 Results and discussion 52

4.2.1 Enforcing trimer formation at a specific dihedral angle 52

4.2.2 Rectangular Kern-Frenkel 54

4.2.2.1 Parametrising rectangular patches 54

4.2.2.2 Defining two rectangular patches on the particle surface . . 57

4.2.2.3 The modified angular component and its computation . . . 58

4.2.2.4 Extending this model to more complex patch geometries . . 60

4.2.3 Parametrisation of particles with two rectangular patches 61

4.2.4 Self-assembly of particles with two rectangular patches at various skew angles (χ) . . . 61
4.2.4.1 Kagome . . . 64
4.2.4.2 Helical . . . 66
4.2.4.3 9-oid . . . 67
4.2.4.4 8-oid . . . 68
4.3 Conclusions . . . 70

5 Self-Assembly Routes to Single Colloidal Gyroid 71
5.1 Introduction . . . 71
5.2 Results and discussion . . . 72
5.2.1 Self-assembly of colloidal gyroid using two rectangular patches . . . 72
5.2.1.1 Rectangular patch parameter space for crystallisation . . . 74
5.2.1.2 Effects of number density on crystallisation . . . 77
5.2.1.3 Polydispersity in rectangular patch coverage . . . 79
5.2.1.4 Polydispersity in rectangular patch orientation . . . 81
5.2.1.5 Polydispersity in rectangular patch coverage and orientation 83
5.2.2 Self-assembly of colloidal gyroid using four circular patches . . . 84
5.2.2.1 Patch-pair separation angle parameter space for crystallisation 86
5.2.2.2 Polydispersity in circular patch coverage . . . 87
5.3 Conclusions . . . 89

6 Self-Assembly Routes to Double Colloidal Gyroid 91
6.1 Introduction . . . 91
6.2 Results and discussion . . . 92
6.2.1 Stabilising double colloidal gyroid using a racemic mixture . . . 92
6.2.2 Self-assembly *via* DNA-mediated interactions . . . 96
6.2.3 Self-assembly *via* a hierarchy of interactions . . . 98

6.2.4 Templated self-assembly from particles with circular patches 102
6.3 Conclusions 106

7 Summary and Outlook **109**

References **113**

List of Figures

1.1 Five largest 3D photonic band gap structures 3
1.2 Multi-patch particles *via* vapour deposition and stamping 5
1.3 Patchy particle attributes with which to control self-assembly behaviour . . . 6
1.4 Multi-patch particles *via* sequential tilted depositions 7
1.5 Patchy particles *via* colloidal fusion 9
1.6 Non-circular patches *via* glancing angle vapour deposition 10
1.7 Targeted self-assembly of a kagome colloidal crystal 12
1.8 Five generations of colloidal building blocks 12
1.9 Targeted self-assembly of a cubic diamond colloidal crystal 15
1.10 The gyroid structures 17

2.1 Basin-hopping global optimisation 24
2.2 Constructing directed bonding graphs 29
2.3 Dihedral angle determination 32

3.1 Reverse engineering of single network gyroid 38
3.2 Per-particle energy of dimer, trimer, and tetramer clusters as a function of patch half-opening angle θ 39
3.3 Cubic unit cell of right-handed single colloidal gyroid 41
3.4 Cubic unit cell of double colloidal gyroid 41
3.5 Rectangular supercell of kagome 42
3.6 Orthorhombic supercell of Fddd 43

3.7 Orthorhombic supercell of Cccm 44
3.8 Monoclinic supercell of C2/m 45
3.9 Cubic supercell of right-handed quadruple trigonal K_4 46
3.10 Optimising circular patches to form trimers 47
3.11 Self-assembly of stacked kagome planes 48
3.12 Self-assembly of stacked kagome planes snapshots 49

4.1 Inter-trimer dihedral angle selection using rectangular patches 53
4.2 Defining rectangular patches using latitudinal and longitudinal lines 55
4.3 Two distinct patch geometries corresponding to two pairs of half-opening angles where the values are swapped 56
4.4 Fully labelled schematics of a patchy particle with two rectangular patches . 57
4.5 Orientational criteria for rectangular patches 60
4.6 Parametrisation of particles with two rectangular patches 61
4.7 Structures self-assembled from particles with two rectangular patches at various skew angles (χ) 63
4.8 Kagome region of skew angle space for particles with two trimer-forming rectangular patches 64
4.9 Ring distributions at various temperatures for the kagome region of skew angle space 65
4.10 Helical regions of skew angle space for particles with two trimer-forming rectangular patches 66
4.11 9-oid regions of skew angle space for particles with two trimer-forming rectangular patches 68
4.12 8-oid region of skew angle space for particles with two trimer-forming rectangular patches 69

5.1 Self-assembly of single colloidal gyroid from particles with two staggered rectangular patches . . . 73
5.2 Robustness of rectangular patch coverage space for crystallising single colloidal gyroid . . . 75
5.3 Robustness of skew angle space for crystallising single colloidal gyroid structures 76
5.4 Single colloidal gyroid crystallization at various number densities . . . 78
5.5 Single colloidal gyroid crystallisation from particles with two rectangular patches of polydisperse coverage . . . 80
5.6 Single colloidal gyroid crystallisation from particles with two rectangular patches of polydisperse skew angle . . . 82
5.7 Single colloidal gyroid crystallisation from particles with two rectangular patches of polydisperse coverage and orientation . . . 83
5.8 Design and parametrisation of particles with four circular patches . . . 85
5.9 Self-assembly of single colloidal gyroid from particles with four circular patches 86
5.10 Robustness of patch-pair separation angle space for crystallising single colloidal gyroid . . . 87
5.11 Single colloidal gyroid crystallisation from particles with four circular patches of polydisperse coverage . . . 88

6.1 Stabilising double colloidal gyroid using a racemic mixture . . . 93
6.2 Growth of a double colloidal gyroid crystal interfaced with a racemic fluid . . 95
6.3 Self-assembly of double colloidal gyroid *via* DNA-mediated interactions . . . 97
6.4 First stage of assembly of double colloidal gyroid . . . 99
6.5 Second stage of assembly of double colloidal gyroid . . . 101
6.6 Templating colloidal gyroid self-assembly from patchy particles with two circular patches . . . 104

6.7 Probing the self-assembly pathway of templated double colloidal gyroid from patchy particles with two circular patches 105

Chapter One

Introduction

1.1 Colloidal self-assembly

Colloids are mixtures of microscopic particles of one substance suspended in another substance, where the suspended particles size can range from 1 nm to 1 µm [1]. Common examples of colloids include milk, paints, and foams. The size of the suspended particles is such that they are small enough to experience negligible gravitational effects and for thermal energy to drive their dynamics, but large enough to be visible under an optical microscope.

The random motion exhibited by colloidal particles is called 'Brownian motion' and is named after Robert Brown who reported the phenomenon in 1827 whilst observing the motion of pollen immersed in water under a microscope [2]. It wasn't until 1905 that Albert Einstein proposed that this motion was a result of many collisions with the water molecules [3], which was later verified experimentally by Jean Baptiste Perrin [4] which led to him being awarded the 1926 Nobel Prize in Physics for his work on the "discontinuous structure of matter" [5]. A major consequence of this Brownian motion is that colloidal systems strive to reach thermodynamic equilibrium structures which minimise free energy. These relatively large colloidal particles display behaviour in line with their molecular counterparts, and have

even been described as "big atoms" [6]. This "atomic" behaviour of colloids in combination with the fact that they are microscopically visible, and move on a much longer timescale than molecular systems, has led to them being used to study phenomena such as the kinetics of crystallisation [7–9] and the nature of glassy states [10, 11]. It is important to note, however, that in colloidal systems, factors such as polydispersity and the influence of hydrodynamics on dynamic processes also come into play.

Self-assembly is the organisation of components into ordered structures or patterns in the absence of human intervention. Self-assembly processes are widespread throughout nature, occur over all length scales, and can involve various different types of interactions [12]. Colloidal self-assembly has great potential as a bottom-up route to the formation of novel structures for functional materials [13, 14]. The seminal work by Pusey and van Megen in 1986 [15] demonstrated experimentally the self-assembly of hard-sphere colloidal crystals from a fluid phase, validating the claims of previous computational work [16–18]. This is a prominent example of colloidal crystallisation, since the potential energy change is zero and therefore completely driven by entropy [19]. The hard-sphere system, however, is limited to the formation of close-packed crystals (fcc and hcp), and a random stacking of close-packed layers (referred to as 'random hcp') is observed [20] due to their similar free energies [21].

1.2 3D photonic crystal structures

Though self-assembled colloidal structures have many potential applications [22–25], they are particularly appealing as photonic crystals. Photonic crystals are periodic structures of alternating high and low refractive index materials, arranged such that light in a certain frequency range is forbidden to propagate through the crystal. This range of frequencies is referred to as a photonic band gap. The low refractive index material is typically air, and

photonic crystals can be one, two, or three dimensional possessing photonic band gaps in corresponding dimensions [26].

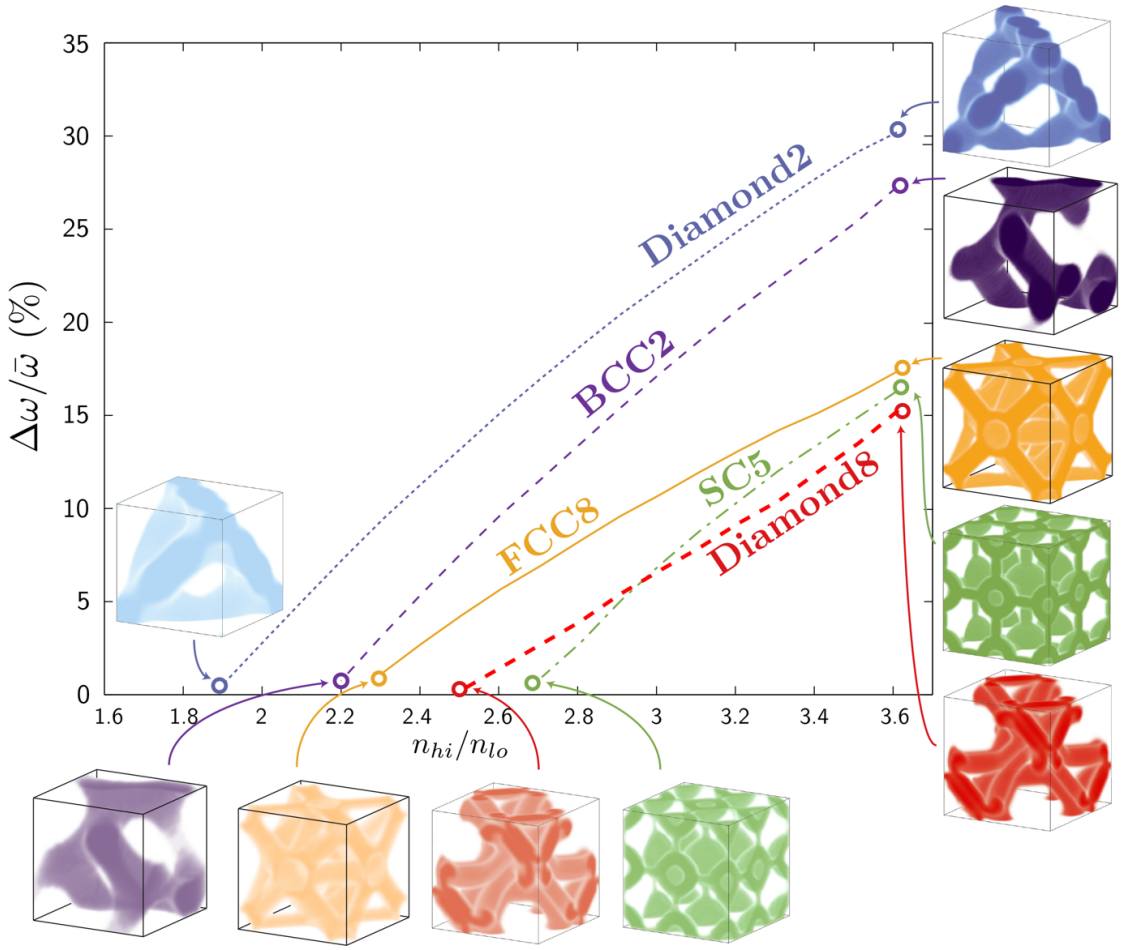


Figure 1.1: **Five largest 3D photonic band gap structures.** 3D photonic band gap ($\Delta\omega/\bar{\omega}$) vs refractive index contrast (n_{hi}/n_{lo}) for the five structures identified with the largest band gaps. The unit cells of each structures high refractive index region (n_{hi}) are shown at a refractive index contrast of 3.6, and where the band gap first opens up. Figure from [27].

1D photonic crystals are already in widespread use as coatings on lenses and mirrors [28], with 2D photonic crystals seeing use as optical fibres [29]. Top-down fabrication techniques such as lithography have failed to provide cost-effective production means regarding 3D photonic crystals, resulting in much focus on obtaining bottom-up fabrication routes to

such structures *via* self-assembly [30]. With potential applications in areas such as light-harvesting technology [31], energy storage [32], sensing [33], and optical circuits [34, 35], colloidal self-assembly offers a cost-effective and scalable fabrication method for 3D photonic crystals.

When designing routes to 3D photonic crystals, one must first identify target photonic structures. Men *et al.* performed a voxel-based optimisation in order to identify crystal structures with the largest 3D photonic band gaps [27]. The structures they identify are in line with those proposed previously with only slight improvements [36, 37]. Figure 1.1 shows the 3D photonic band gaps as a function of the refractive index contrasts for the structures identified with the five largest band gaps. The structure with the largest identified 3D band gap is rod-connected diamond (labelled here as "Diamond2"), closely followed by the single network gyroid structure (labelled as "BCC2"). The yellow, green, and red structures which then follow are rod-connected variations of FCC, simple cubic, and diamond structures respectively. It is notable that these structures are rather open and mostly low-coordinated [38, 39].

1.3 Patchy colloidal building blocks

Over time, there have been significant advances in the synthesis of colloidal building blocks. The ability to control various aspects such as shape and surface chemistry, offers diverse and tunable building blocks for the potential formation of novel functional materials [13, 40, 41]. In principle, routes to exotic structures can be devised from limitless types of building blocks, so long as suitable fabrication methods exist. In the context of self-assembly, so called 'patchy particles' – where regions of the particle surface are chemically distinct – have drawn much attention, due to their highly directional interactions which can stabilise

low-coordinated and open structures [42].

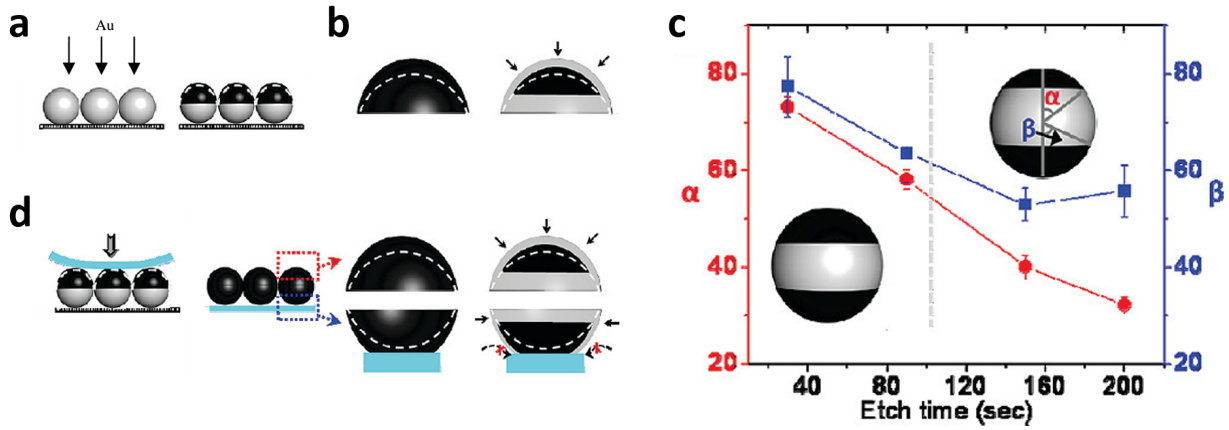


Figure 1.2: **Multi-patch particles *via* vapour deposition and stamping.** (**a**) Schematic of a monolayer of colloidal spheres being coated *via* vapour deposition. (**b**) Close up of the coating to emphasise its variable thickness which is thinner closer to the edge. A consequence of this is that uniform etching gradually reduces the size of the patch as illustrated (right). (**c**) Patch size (half-opening angle) as a function of etch time for coatings in contact with a stamp (β) and not in contact (α). (**d**) Schematic of a sticky stamp (in blue) being used to flip the monolayer to deposit another coating, with close ups (right) illustrating how the patch sizes shrink differently when etched in the presence of a stamp. Figure adapted from [43].

One method of synthesising patchy particles is to deposit metal vapour from above onto a monolayer of particles [43, 44]. Particles are first spread onto a flat substrate and a metal vapour (typically gold) is then deposited perpendicular to the substrate, resulting in the complete coating of one hemisphere as shown in Figure 1.2**a**. Spherical particles give rise to a non-uniform coating which can be exploited to control the patch coverage. The coating is thickest in the centre and gradually thins out towards the edges as demonstrated in Figure 1.2**b**, therefore when exposed to a uniform etching solution the coverage of the

patch decreases as a function of etch time (Figure 1.2**c** red line). In the case of a gold coating, gold-thiol chemistry is used to functionalise the patch surface with, for example, a hydrophobic coating giving rise to the patch-patch attraction. Vapour deposition can also be used in combination with a stamp in order to deposit another patch onto the opposite hemisphere of the particles. This is shown schematically in Figure 1.2**d**, where after the first deposition a stamp is attached on top of the monolayer and flipped in order to allow for the deposition of another coating. This stamp also acts to protect the attached coating, which is demonstrated in Figure 1.2**c** where the blue line shows the patch coverage of the stamped side as a function of etch time and there is a clear halt in etching compared with the non-stamped patch coverage (red line) which continues to decrease.

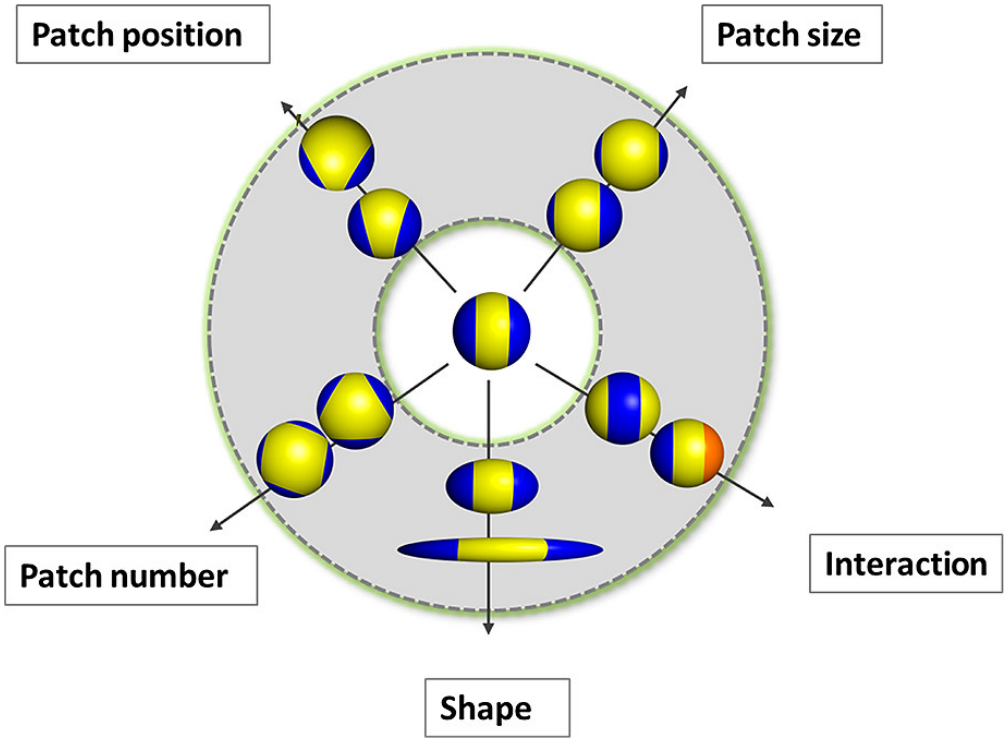


Figure 1.3: **Patchy particle attributes with which to control self-assembly behaviour.** Interaction profile, particle shape, patch size, patch number, and patch position. Figure from [45].

Chen *et al.* [45] illustrate five attributes which can be used to characterise the vast parameter space of patchy particles alone, as shown in Figure 1.3. Control over these attributes, namely interaction profile, particle shape, patch size, patch number, and patch position, is synthetically possible to various degrees and can be exploited in order to influence particle self-assembly behaviour. This section will briefly cover synthetic methods most relevant to the work in this thesis and to notable examples of colloidal self-assembly. For a more extensive summary of patchy particle fabrication methods, please see the following reviews [46–49].

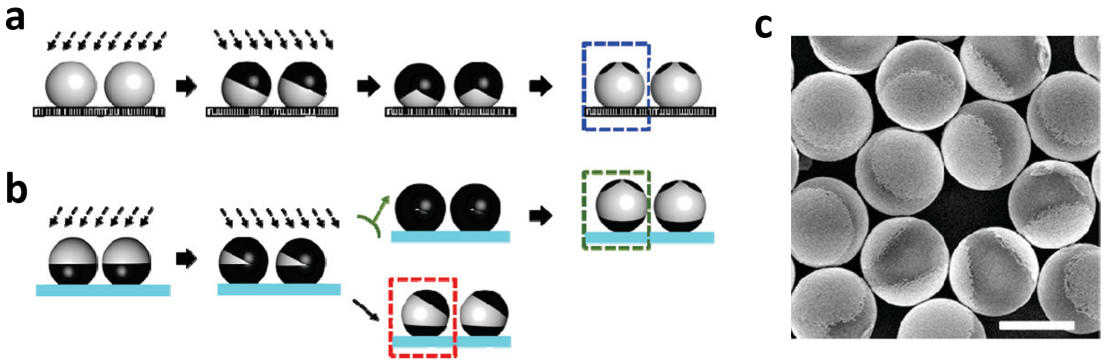


Figure 1.4: **Multi-patch particles *via* sequential tilted depositions.** (**a-b**) Schematics of how multiple tilted depositions can fabricate various multi-patch particles, where the blue substrate represents the use of a stamp. (**c**) SEM image of particles of the same nature as those within the dashed red box in **b** (scale bar represents 2 µm). Figure adapted from [43].

Deposition at an angle to the particle monolayer can give control over patch position, and patch number when multiple depositions are performed [43]. This is shown schematically in Figure 1.4, where Figure 1.4**a** demonstrates the synthesis of a circular patch pair, where the deposition angles can control each patch's position on the particle surface. Note that here the monolayer particles must be sufficiently far apart so as to avoid shadowing of the deposition. Figure 1.4**b** shows how this approach can be used in combination with a flipping of the monolayer *via* stamping to give additional control over patch position, size, and number. Figure 1.4**c** shows an SEM image of particles, of the same nature as the schematic

within the red dashed box, synthesised using this method with two depositions in total.

The functionalisation of building blocks with DNA strands gives rise to highly programmable interactions. These 'DNA-mediated' interactions are a powerful method of controlling the self-assembly behaviour of colloidal building blocks, since they are specific, reversible, and tunable [50–52]. Particles with a complete DNA coating are referred to as 'programmable atom equivalents' and the tunability of their DNA-mediated interactions, in particular their specificity, has yielded the self-assembly of a variety of multi-component crystal structures [53–56]. Through the selection of appropriate DNA strands, the interaction matrices defined by different components within a system opens up a high dimensional design space to be exploited, as the number of components increases [25]. These DNA coatings can also be applied to surface patches [57, 58] in order to combine directional bonding with specificity, and grant increased control over the patch-patch interactions within a system.

Gong *et al.* developed a method of synthesising patchy particles which they refer to as 'colloidal fusion' [59]. Their method offers scalable routes to well defined particles with control over their morphology. Figure 1.5 demonstrates how colloidal fusion can be used to synthesise multi-patch particles, where Figure 1.5**a** introduces the colloidal fusion method with an analogous macroscopic system. It shows four malleable orange spheres forming a tetrahedral arrangement around a smaller and softer purple core. When spherical pressure is applied to the cluster it gradually deforms, and as the outer cluster is compressed the purple core is extruded until a spherical particle with four well defined patches is formed. Figure 1.5**b** shows snapshots of a time-lapse of this process experimentally on the micron scale, and Figure 1.5**c** presents the resulting particles for different starting clusters.

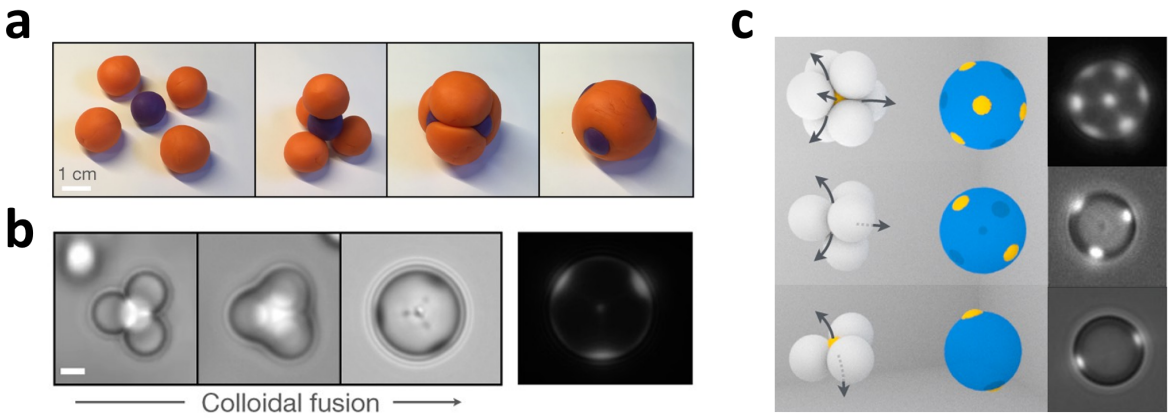


Figure 1.5: **Patchy particles *via* colloidal fusion.** (**a**) Macroscopic "play-dough" model illustrating colloidal fusion, where four malleable orange spheres form a tetrahedral arrangement around a smaller and softer purple core, which when compressed results in a spherical particle with four tetrahedrally arranged patches. (**b**) Bright-field time-lapse images of tetrahedral colloidal fusion (scale bar represents 1 µm), and a fluorescence microscopy image at the final time point (right). (**c**) Schematics of three different colloidal fusion system sizes, and optical microscopy images of corresponding particles. Figure adapted from [59].

An additional attribute, which is not encompassed in Figure 1.3, is patch shape. While control over patch shape is currently somewhat limited, computational studies have shown that if such control can be achieved it can induce significantly different self-assembly behaviour – particularly in the area of structure selection [60]. The 'colloidal fusion' method has recently been used to synthesise particles with triangular patches, but with limited control on their arrangement [61]. Pawar and Kretzschmar demonstrate the use of glancing angle vapour deposition to generate various non-circular patch geometries [62]. Their method relies upon deposition onto a close packed monolayer, at angles with respect to the plane of the monolayer and the orientation of the monolayer, such that neighbouring particles shadow the coating. Figure 1.6**a** shows this schematically to produce a rectangular patch coating (shown in blue), where the blue arrow indicates the deposition direction at a glancing angle of 2°, and the resultant shadowing by particles 2, 4, and 5 is displayed below viewed from

the deposition source. Various glancing angles in combination with different deposition directions can give rise to a range of patch geometries as demonstrated in Figure 1.6**b**. They have also demonstrated this method in combination with a flipping of the monolayer *via* stamping in order to produce particles with multiple patches [63].

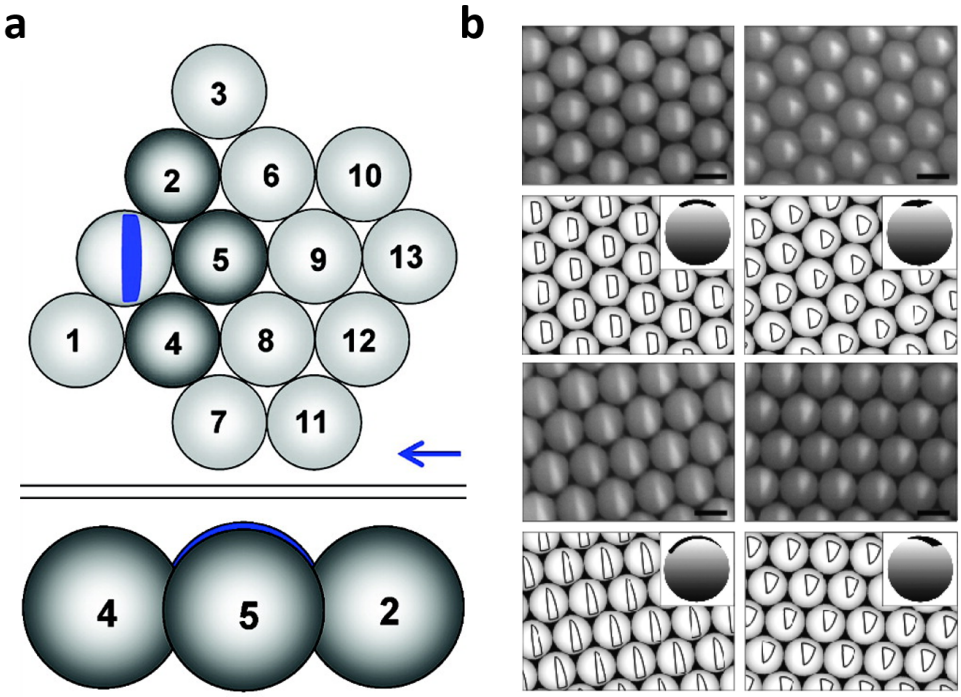


Figure 1.6: **Non-circular patches *via* glancing angle vapour deposition.** (**a**) Schematics of how glancing angle vapour deposition can fabricate particles with rectangular patches, where the deposition is at a glancing angle of 2° and the blue arrow shows its direction. The particle shadowing which gives rise to the blue rectangular patch is shown (bottom), viewed from the deposition source. (**b**) SEM images and calculated schematic representations of patch geometries resulting from various deposition directions at a glancing angle of 2° (scale bars represent 2 µm). Figure adapted from [62].

1.4 Targeted self-assembly of colloidal open crystals

Seminal experimental work by Chen *et al.* demonstrated the targeted self-assembly of a kagome colloidal crystal from 'triblock' patchy particles [64]. The building blocks, shown schematically in Figure 1.7**a** (bottom), were synthesised *via* the vapour deposition method and feature a circular patch on each hemisphere. The patches are rendered hydrophobic and their size is chosen such that each patch forms two contacts, as required by the kagome structure. Figure 1.7**b** shows a fluorescence image of the extended structure. This targeted self-assembly of an open colloidal crystal served as a proof-of-concept for the potential fabrication of novel materials *via* bottom-up routes. The tunability of colloidal building blocks offers a vast parameter space which can be exploited to this end, and increases the importance of computational studies to guide and inform experimental work. Crystal structure prediction has been performed on various patchy systems [65–67] resulting in a range of open crystals which can theoretically be stabilised *via* patchy particles.

In the context of targeted colloidal self-assembly, Kim *et al.* propose a framework which categorises colloidal building blocks into various levels of complexity which they refer to as "generations" [68]. 1$^{\text{st}}$ generation building blocks are simple spheres which are limited to the formation of close packed structures. The interactions of 2$^{\text{nd}}$ generation colloidal clusters differ from spheres due to their shape anisotropy. The 3$^{\text{rd}}$ generation are simple patchy spheres, and the 4$^{\text{th}}$ generation combines shape anisotropy with the directionality of patchy interactions to achieve directed interactions with control over bonding conformation. This control over bonding conformation is lacking in simple patchy spheres due to the free rotation of particles about patch-patch bonds. Additionally, the authors propose a 5$^{\text{th}}$ generation of building blocks, so called "asymmetric patchy clusters", which are chiral versions of the 4$^{\text{th}}$ generation that the authors foresee as potentially offering self-assembly routes to chiral colloidal structures – which have yet to be observed for previous generations [68].

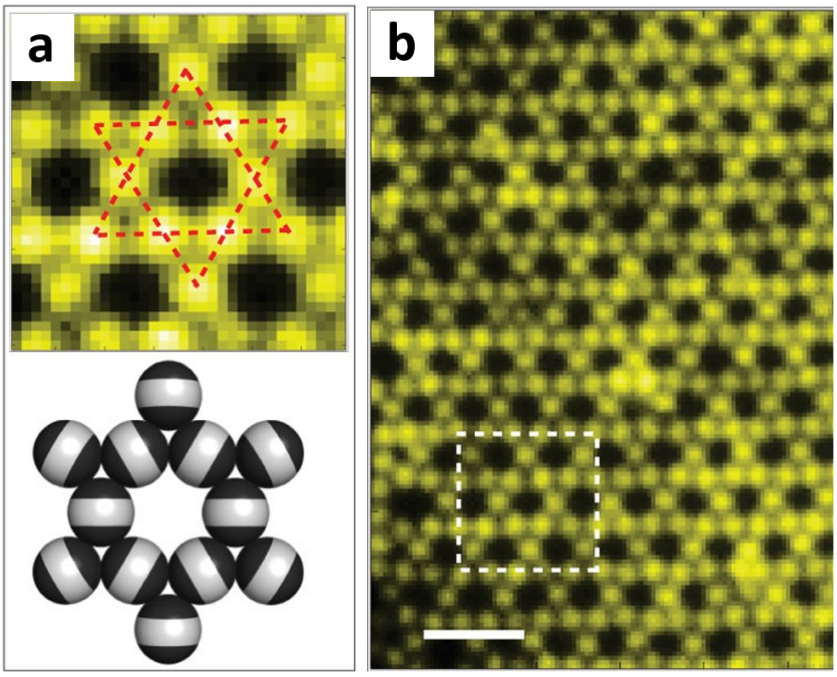


Figure 1.7: **Targeted self-assembly of a kagome colloidal crystal.** (**a**) Zoomed in fluorescence image of the crystal, where the 6-membered ring substructure is highlighted and shown schematically below. (**b**) Fluorescence image of the extended kagome crystal (scale bar represents 4 µm). Figure adapted from [64].

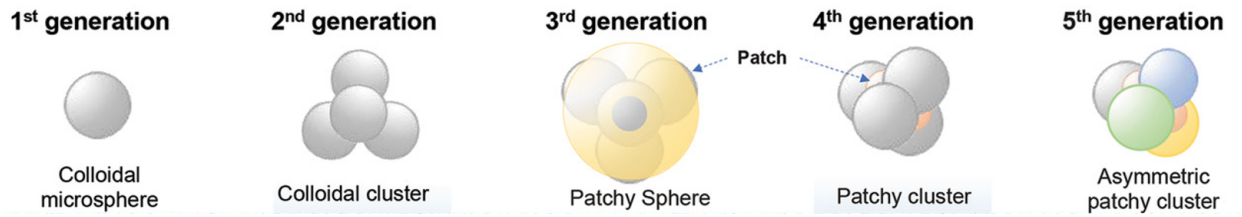


Figure 1.8: **Generations of colloidal building blocks**, as envisioned by Kim *et al.* Figure adapted from [68].

In relation to the targeted self-assembly of colloidal 3D photonic crystals, there has been a major focus on the cubic diamond structure. The fact that rod-connected cubic

diamond possesses the largest known 3D photonic band gap [27] makes the structure an obvious target. Due to their intuitive links, building blocks of tetrahedral symmetry have been extensively investigated for the self-assembly of diamond-structured crystals [69, 70].

Spherical building blocks with four tetrahedrally arranged attractive patches, so called 'tetrahedral patchy particles', have been shown to self-assemble diamond structures *in silico* [71, 72]. Crystallisation was shown to occur for narrow patch half-opening angles of approximately $10^\circ \leq \theta \leq 15^\circ$ [72], where patches which are too narrow (approximately $\theta \leq 10^\circ$) cease forming diamond and kinetic trapping *via* the formation of clathrates is observed instead [73].

Triblock patchy particles with two attractive patches have also been shown to stabilise diamond-related structures [22, 67]. Unlike tetrahedral patchy particles, the building blocks here do not directly possess tetrahedral symmetry; however they are encoded to form tetrahedral sub-units. Here the target 'tetrastack' structure [74] consists of tetrahedrally arranged tetramers of particles centred on each diamond lattice point, and like diamond of spheres [75] has been shown to possess a sizeable 3D photonic band gap [74, 76].

One of the key issues with the targeted self-assembly of diamond-related structures is the fact that the diamond structure possesses two polymorphs, cubic and hexagonal diamond. In terms of photonics, it is specifically the cubic diamond-related structures that possess large 3D band gaps [76]. This raises the issue of polymorph selection, since the free energies of cubic vs hexagonal diamond and tetrastack are almost identical [67]. The examples above which demonstrate the self-assembly of diamond and tetrastack result in random stacking of cubic and hexagonal layers. Proposed methods which demonstrate structure selection include modifying the patch geometry [60], interactions [77], or the use of structure directing agents [78]. As the number of patches increases, their interaction matrix becomes increasingly more complex, often rendering the problem of tuning interactions unmanageable. Recent work has

shown that mapping this to a Boolean satisfiability problem (SAT), can efficiently provide solutions that exclude competing structures [79–81]. Though this inverse-design approach can provide effective solutions to polymorph selection, it requires predefined patchy systems capable of stabilising the target crystal, and said solutions are often complex multicomponent systems which are synthetically challenging. The use of rod-like building blocks has also been demonstrated to potentially circumvent the need for structure selection, by making the resulting structures formed much closer in nature to rod-connected diamond such that the presence of hexagonal regions within the crystal does not close the photonic band gap [82].

Another major issue is kinetic accessibility. Thermodynamic stability alone is typically not enough to result in successful self-assembly – the target structure must also be kinetically accessible so that the system does not become kinetically trapped [83]. Potential solutions to this issue include the use of templates or crystal seeds [71, 84], however the main problem with these is fabricating the templates, and acquiring said seeds. Another method of improving the kinetic accessibility of a target structure is to follow hierarchical self-assembly pathways, which can be encoded with a hierarchy of interaction strengths. This concept of staged assembly is demonstrated for triblock patchy particles *in silico* [85], which are known to stabilise tetrastack crystals [67]. Rao *et al.* show that by making one of the two patches on the spherical building blocks have a higher interaction strength than the other, the assembly of tetrastack crystals can be split into two stages [76]. The first stage involves the formation of tetrahedral tetramers *via* the stronger patches on the elementary building blocks. These discrete tetrahedra then act as secondary building blocks and form tetrastack crystals *via* their exposed weaker patches. The authors demonstrate that this staged approach – as opposed to direct self-assembly from triblock patchy particles with two identical patches – promotes crystallisation by suppressing the formation of odd-membered ring sizes. The key here is that tetrastack crystals are comprised of 6- and 8-membered rings therefore the formation of any other ring size is a guaranteed kinetic trap, hence the secondary tetrahedral

building blocks which cannot form odd-membered rings promote crystallisation compared to the elementary particles. This concept of ring control has also been explored in relation to tetrahedral patchy particles where the use of a two-component system, in which half of the particles have no attraction to the other half, has been shown to increase the parameter space for colloidal diamond crystallisation compared to a simple one-component system [86].

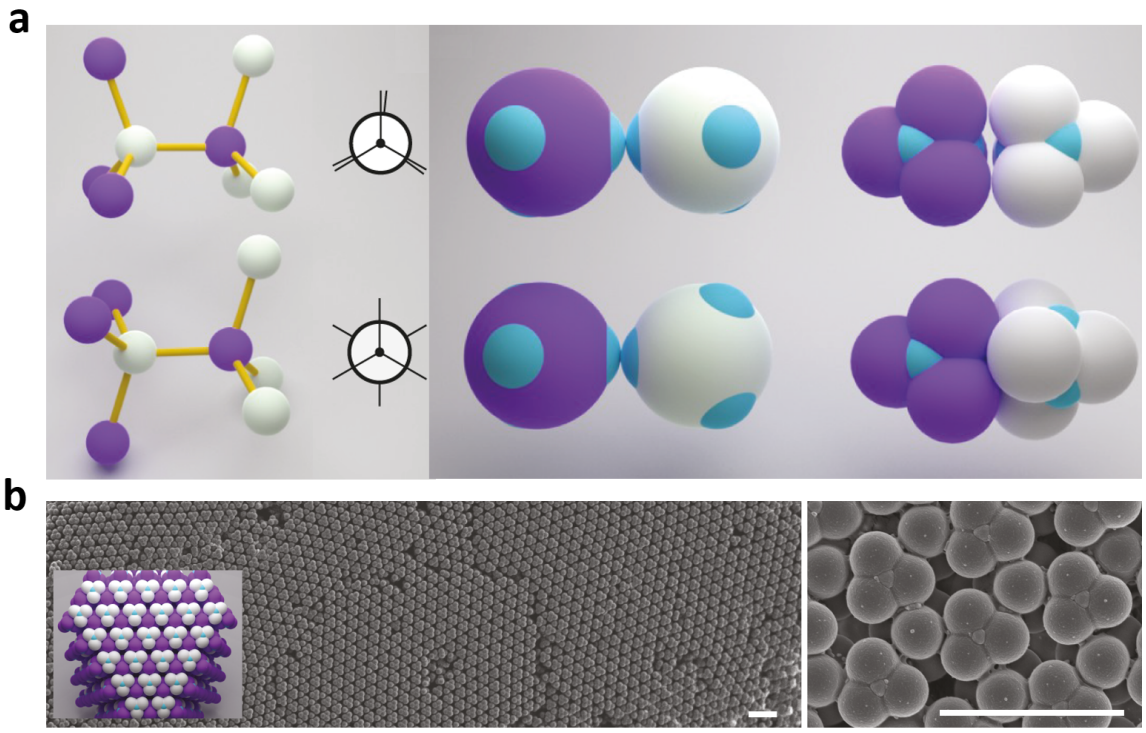


Figure 1.9: **Targeted self-assembly of a cubic diamond colloidal crystal.** (**a**) Schematics of staggered and eclipsed conformations of two adjacent tetrahedra within a diamond structure (left) and their corresponding Newman projections. Corresponding configurations of traditional patchy particles (middle), and patchy tetrahedral clusters (right) where the attractive patches are shown in blue. (**b**) SEM images of the (111) plane of a colloidal diamond crystal (scale bars represent 5 µm). Inset schematic representation of the same plane. Figure adapted from [87].

In 2020, He *et al.* finally demonstrated the self-assembly of a cubic diamond colloidal crystal structure experimentally [87]. They achieve structure selection of the cubic polymorph over hexagonal *via* the use of "4$^{\text{th}}$ generation" building blocks (as set out in Figure 1.8). Figure 1.9**a** shows the mechanism of structure selection, where the staggered and eclipsed conformations of two adjacent tetrahedra within a diamond structure are shown (left) alongside their corresponding Newman projections. The key here is that the cubic diamond polymorph contains only staggered connections so selection for exclusively staggered arrangements results in the selective formation of cubic diamond. Traditional patchy particles (middle) possess no conformational preference due to free rotation of particles about patch-patch bonds, but with the use of patchy tetrahedral clusters (right) the conformational selection is sterically encoded into the building blocks. The particles used here consist of four partially overlapping tetrahedrally coordinated spheres which surround a patchy core, and were synthesised *via* "colloidal fusion" [59].

It was determined that both the direct and inverse structures possess a photonic band gap, where the inverse structure refers to an inversion of the high and low refractive index regions of the structure (i.e., replacing the air with material and replacing the original material with air). The authors find that, however, crystallisation can only be achieved using particles for which the inverse structure possesses a band gap and not the direct structure itself. Therefore in order to fabricate a structure with a photonic band gap the authors propose back-filling colloidal diamond with a high refractive index material followed by removal of the original crystal, however this proposed post-processing to yield the 3D photonic band gap material is not demonstrated in this work [87].

1.5 Gyroid structures and their fabrication

Gyroid is a triply periodic minimal surface that partitions 3D space into a pair of intertwined labyrinths [88]. The skeletal graphs of these labyrinths, as shown in Figure 1.10**a**, define the two enantiomorphic single networks of gyroid, which have three-fold connectivity at each node and characteristic 10-membered rings [88, 89]. The Wigner-Seitz (WS) cells of these enantiomorphs are shown in Figure 1.10**b**, each viewed along a strut to emphasise their characteristic dihedral angles. The dihedral angles between adjacent nodes for a given enantiomorph of single network gyroid are all approximately equal to either 70.5° or 109.5°, depending on the chirality [90].

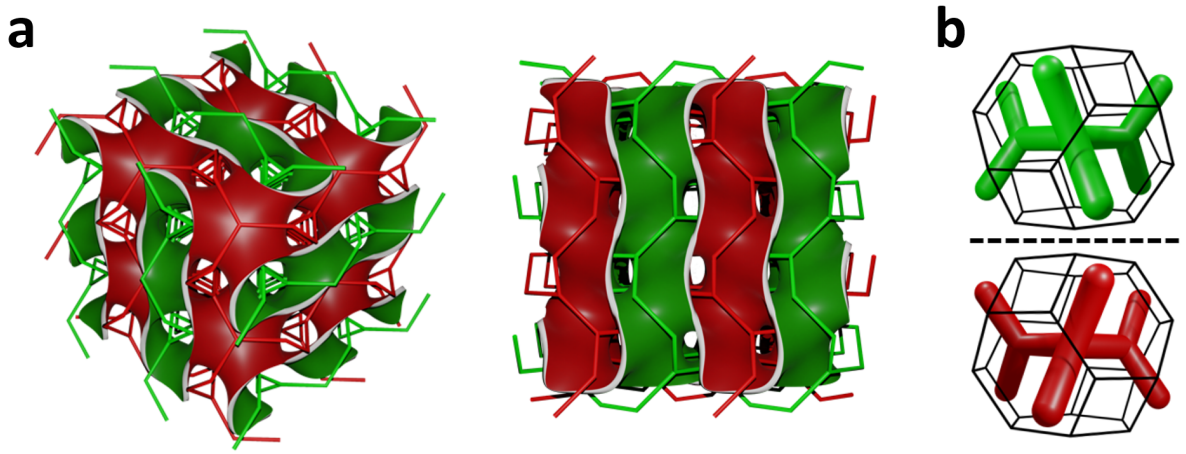


Figure 1.10: **The gyroid structures.** (**a**) $2 \times 2 \times 2$ supercells showing the gyroid minimal surface along with its two associated skeletal graphs viewed along the [111] and [100] axes. (**b**) Wigner-Seitz cells of the single-network gyroids of opposite handedness viewed along a strut to emphasise their distinct dihedral angles.

The single network gyroid structure, which has a body-centred cubic Bravais lattice with the space group $I4_132$, has the 2nd largest known 3D photonic band gap [27, 37, 91]. Despite possessing this near-champion photonic band gap, in the context of targeted self-

assembly of colloidal crystals the single gyroid structure has largely been ignored, presumably due to its structural complexity and chirality. Though the chirality of single gyroid poses challenges regarding targeted self-assembly, due to its intrinsic competing enantiomorphs which must be addressed, it is also a beneficial aspect from the perspective of potential applications as a chiral photonic crystal and metamaterial at optical frequencies [92–94].

In terms of direct self-assembly, single gyroid remains elusive [95–97]. This is in contrast to double gyroid which is common in systems with elements of frustration such as surfactants, block copolymers, and mesogens [90, 98–100]. Surprisingly single gyroid is actually observed in nature within the structure of butterfly wing scales [101] giving rise to their colourful appearance, however the formation of this structure has been found to not be the result of direct self-assembly, but instead *via* a double gyroid precursor [102]. Current self-assembly routes to single gyroid structures mimic this natural process, first assembling a double gyroid then removing one network *via* some post-processing [103]. Unfortunately, the size of most block copolymer gyroids is such that the mid-gap frequency of the resulting photonic band gap is within the UV region of the spectrum [92].

This lack of an efficient fabrication method for single gyroid photonic crystals – and 3D photonic crystals in general – which operate within the visible wavelength region [92], poses an opportunity for the self-assembly of a single gyroid structure built from colloidal particles in the size range of hundreds of nanometres to provide an efficient and cost-effective bottom-up route to chiral photonic crystals. Such a route would also provide a band gap which can be easily tuned *via* the size of the colloidal building blocks facilitating its many potential applications including photonic circuitry [34, 35].

1.6 Thesis outline

In this context, the aim of this thesis was to devise strategies for the targeted self-assembly of a single gyroid structure from colloidal building blocks. To this end, the self-assembly of various types of patchy particles was studied using computer simulations. The objectives were as follows:

1. Reverse-engineer single network gyroid into patchy colloidal building blocks;
2. Develop, if necessary, new models with which to simulate said particles;
3. Establish self-assembly routes to single gyroid colloidal crystals from minimal particle designs *in silico*;
4. Adapt these design principles to the self-assembly of double gyroid colloidal crystals.

The remainder of this thesis is organised as follows. Chapter 2 outlines the computational methods employed to carry out this body of work. Chapter 3 explores the reverse engineering of single network gyroid, exploiting its underlying three-fold connectivity, and presents single gyroid colloidal crystal structures along with a library of competing crystals. Chapter 4 details a pair potential developed in order to study particles with rectangular patches. Chapter 5 explores enantiomorphic self-assembly routes to single gyroid colloidal crystals *in silico*, and Chapter 6 details how a bottom-up route can be adapted for the self-assembly of double colloidal gyroid. Finally, Chapter 7 summarises this body of work and presents an outlook for the future.

Chapter Two

Methodology

In this chapter, a widely used model of patchy particles and a continuous counterpart are described before presenting an outline of Monte Carlo (MC) simulation which is used to carry out this body of work. Finally, a few analysis methods used herein are also described.

2.1 Models

The traditional approach of a one-component description with an effective pair potential is used in this thesis to simulate colloidal suspensions of patchy particles with implicit solvent.

2.1.1 Kern-Frenkel

Particles with circular patches were modelled using the Kern-Frenkel (KF) pair potential [104], where each particle has a hard core with diameter σ and n circular patches on its surface. The effective pair potential is defined as a combination of a hard-sphere potential (u^{hs}) and a square-well potential (u^{sw}) with an angular modulation ($f_{\mathrm{pp}\prime}$):

$$u_{ij}(\mathbf{r}_{ij}, \hat{\mathbf{\Omega}}_i, \hat{\mathbf{\Omega}}_j) = u_{ij}^{\mathrm{hs}}(r_{ij}) + u_{ij}^{\mathrm{sw}}(r_{ij}) \sum_{\mathrm{p}\in i}^{n} \sum_{\mathrm{p}'\in j}^{n} f_{\mathrm{pp}\prime}(\mathbf{r}_{ij}, \hat{\mathbf{\Omega}}_i, \hat{\mathbf{\Omega}}_j) \tag{2.1}$$

where $\mathbf{r}_{ij}$ is the separation vector between particles i and j ($\mathbf{r}_{ij} = \mathbf{r}_j - \mathbf{r}_i$), r_{ij} is the magnitude of the vector $\mathbf{r}_{ij}$, and $\hat{\mathbf{\Omega}}_i$ and $\hat{\mathbf{\Omega}}_j$ describe the orientations of particles i and j respectively.

u_{ij}^{hs} is the hard-sphere pair potential:

$$u_{ij}^{\mathrm{hs}}(r_{ij}) = \begin{cases} \infty & \text{if } r_{ij} < \sigma \\ 0 & \text{otherwise} \end{cases} \tag{2.2}$$

u_{ij}^{sw} is a square-well potential given by:

$$u_{ij}^{\mathrm{sw}}(r_{ij}) = \begin{cases} -\varepsilon & \text{if } \sigma \leq r_{ij} < \lambda\sigma \\ 0 & \text{otherwise} \end{cases} \tag{2.3}$$

where ε is the well-depth and λ controls the range of the attraction.

The angular component is given by:

$$f_{\mathrm{pp}\prime}(\mathbf{r}_{ij}, \hat{\mathbf{\Omega}}_i, \hat{\mathbf{\Omega}}_j) = \begin{cases} 1 & \text{if } (\hat{e}_{\mathrm{p}} \cdot \hat{\mathbf{r}}_{ij} \geq \cos\delta_{\mathrm{p}}) \text{ and } (\hat{e}_{\mathrm{p}\prime} \cdot \hat{\mathbf{r}}_{ji} \geq \cos\delta_{\mathrm{p}\prime}) \\ 0 & \text{otherwise} \end{cases} \tag{2.4}$$

where δ_{p} is the half opening angle which defines the coverage of patch p, and $\hat{e}_{\mathrm{p}}$ is the unit vector from the centre of particle i to its patch p under consideration.

Here the angular component ensures that patches on two particles i and j can only interact if the inter-particle separation vector $\mathbf{r}_{ij}$ passes through patch surface on both particles.

2.1.2 Continuous patchy pair potential

In order to perform crystal structure prediction for triblock patchy colloidal particles, a continuous pair potential is employed [85].

Each spherical particle has two circular patches A and B at opposite poles. These patches A and B can differ in terms of their surface coverage, characterised by the half-opening angles α and β respectively. The patches A and B can both interact with themselves and one another, where, ϵ_{AB} is the depth of the potential due to the patch A - patch B interaction when the two patches face each other. The effective potential for a pair of patchy particles is defined as a combination of a repulsive Yukawa potential (u_{ij}^{Yuk}) and the product of a distance (w_{ij}) and angular component ($f_{\mathrm{pp}\prime}$) of the patchy interaction:

$$u_{ij}(\mathbf{r}_{ij}, \hat{\mathbf{\Omega}}_i, \hat{\mathbf{\Omega}}_j) = u_{ij}^{\mathrm{Yuk}}(r_{ij}) + \sum_{\mathrm{p}\in i}^{n}\sum_{\mathrm{p}'\in j}^{n} w_{ij}(r_{ij}) f_{\mathrm{pp}\prime}(\mathbf{r}_{ij}, \hat{\mathbf{\Omega}}_i, \hat{\mathbf{\Omega}}_j) \tag{2.5}$$

where $\mathbf{r}_{ij}$ is the separation vector between particles i and j, r_{ij} is the magnitude of the vector $\mathbf{r}_{ij}$, and $\hat{\mathbf{\Omega}}_i$ and $\hat{\mathbf{\Omega}}_j$ describe the orientations of particles i and j respectively.

The repulsive Yukawa potential is given by:

$$u_{ij}^{\mathrm{Yuk}} = \epsilon_Y \frac{\exp[-\kappa(r_{ij} - \sigma)]}{r_{ij}/\sigma} \tag{2.6}$$

where κ is the inverse Debye screening length and ϵ_Y is the Yukawa contact potential.

The angular dependence of the patch-patch interaction is given by:

$$f_{\mathrm{pp}\prime}(\mathbf{r}_{ij}, \hat{\mathbf{\Omega}}_i, \hat{\mathbf{\Omega}}_j) = \epsilon_{\mathrm{pp}\prime}\frac{1}{4}[1 + \Phi(\mathbf{r}_{ij}, \hat{\mathbf{\Omega}}_i, \hat{\boldsymbol{p}}_i)][1 + \Phi(\mathbf{r}_{ji}, \hat{\mathbf{\Omega}}_j, \hat{\boldsymbol{p}}_j)] \tag{2.7}$$

$$\Phi(\mathbf{r}_{ij}, \hat{\mathbf{\Omega}}_i, \hat{\boldsymbol{p}}_i) = \begin{cases} -\cos\left(\frac{\pi[\cos\theta_{ijp_i} - \cos\delta]}{1-\cos\delta}\right) & \text{if } \cos\theta_{ijp_i} \geq \cos\delta \\ -1 & \text{otherwise} \end{cases} \tag{2.8}$$

where $\boldsymbol{p}_i$ is the normalised vector from the centre of the spherical particle i in the direction of the centre of patch p; $\cos\theta_{ijp_i}$ is the dot product of the vectors $\hat{\boldsymbol{r}}_{ij}$ and $\hat{\boldsymbol{p}}_i$; and δ is the half-opening angle of the patch under consideration (α or β).

The distance dependence of the patch-patch interaction is given by:

$$w_{ij}(r_{ij}) = \begin{cases} -1 & \text{if } (r_{ij} - \lambda) < 0 \\ -\frac{1}{2}[1 + \cos(\pi(r_{ij} - \lambda)s)] & \text{if } 0 \leq (r_{ij} - \lambda) \leq s^{-1} \\ 0 & \text{otherwise} \end{cases} \tag{2.9}$$

where λ is the largest separation at which the patch p - patch p′ attraction is at its strongest, and the parameter s controls the range over which this attraction vanishes. In this study, λ was set to 1.01σ.

2.2 Basin-hopping global optimisation

In this thesis global optimisation is performed, a process in which the potential energy surface is explored with the purpose of identifying global minima. The potential energy surface is a multi-dimensional surface that shows how the potential energy of a system changes as a function of the positional and orientational coordinates that define said system. If $\mathbf{x}$ is a vector that contains all the positional and orientational coordinates required to define a system, then $u(\mathbf{x})$ is the potential energy function that defines the potential energy surface.

To explore the potential energy surface a method called "basin-hopping" is used [105]. This method deforms the potential energy surface into a series of "basins" such that:

$$u^b(\mathbf{x}) = \min\{u(\mathbf{x})\} \tag{2.10}$$

where each point $\mathbf{x}$ is mapped to its corresponding local minimum energy following a local optimisation min{}. Note that this local minimisation necessitates the use of a continuous potential. Random Monte Carlo-like "hops" in configurational space are then used to explore the basins of this deformed surface – hence the name basin-hopping. Figure 2.1 shows this process schematically on a 1D energy surface (black line) where local minimisation is indicated with green arrows, a basin hop is shown in red, and the dotted black line shows the deformed surface of basins.

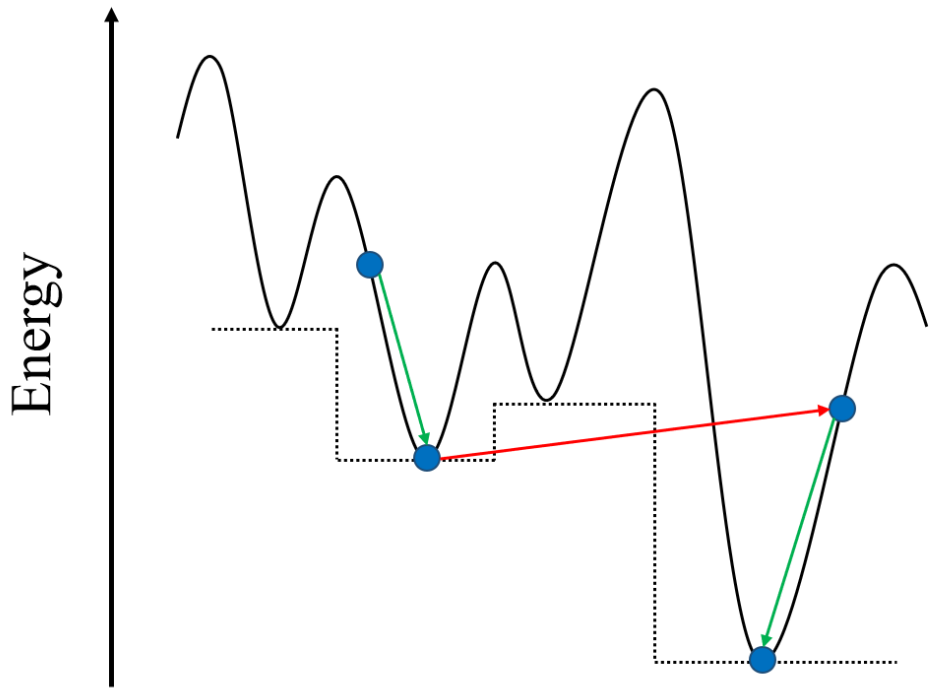


Figure 2.1: **Basin-hopping global optimisation.** Schematic of a 1D energy surface, where local minimisations are indicated by green arrows, the red arrow represents a basin hop, and the deformed energy surface of basins is shown in dotted black.

The specific protocol employed in this thesis, as implemented in the software GlOSP (developed in-house), is as follows:

1. Perform local minimisation of starting configuration.
2. Propose a random perturbation $\Delta\mathbf{x}$ from current minimum $\mathbf{x}_a$ with energy u_a.
3. Locally minimise the perturbed configuration $\mathbf{x}_a + \Delta\mathbf{x}$ to give $\mathbf{x}_b$ with energy u_b.
4. Accept or reject the new configuration $\mathbf{x}_b$ (if $u_b < u_a$ then accept, otherwise accept with a probability of $\exp[-\Delta u/(k_\mathrm{B}T)]$ where Δu is the difference in energy $u_b - u_a$ and T is a fictitious temperature used to tune the acceptance of uphill steps).
5. End after a set number of iterations or go to step 2.

where local minimisation is performed using the limited-memory Broyden–Fletcher–Goldfarb–Shanno (L-BFGS) algorithm [106].

2.2.1 Crystal structure prediction

Global minima on the potential energy surface correspond to stable configurations and represent a system's most thermodynamically favourable forms at a temperature of absolute zero. For a finite system of N anisotropic particles the underlying potential energy surface is a function of $6N$ variables (3 translational coordinates and 3 orientational variables for each particle). Crystal structures, however, are by definition infinitely repeating configurations and therefore require the further consideration of a unit cell in order to explore the crystal energy landscape. This results in 6 additional parameters relating to the cell under consideration (the cell lengths a, b, c and the angles between them α, β, γ) resulting in $6N + 6$ total parameters which define the potential energy surface. Additionally, since crystal systems are

infinite, the lattice energy requires the calculation of an infinite sum which is therefore truncated using an appropriate radial cutoff beyond which pair interactions are neglected. Here, crystal structure prediction is performed by optimising unit cells with predefined numbers of particles *via* random Monte Carlo-like moves through configurational space (including cell parameters). This is different from common molecular crystal structure prediction methods [107], which use molecular configurations to generate sets of candidate structures by packing molecules according to the symmetry operations of a pre-selected set of space groups.

2.3 Monte Carlo simulations

Metropolis Monte Carlo simulations are widely employed in order to study systems at thermal equilibrium, and are performed extensively throughout this thesis. Simulations of N particles are initialised from the relevant crystals unless stated otherwise, and are carried out under periodic boundary conditions in the canonical ensemble (with fixed N, V, and T). Particle orientations are represented by quaternions.

The Metropolis Monte Carlo method aims to efficiently sample configuration space, and relies upon the construction of a Markov chain in which the probability of accepting a proposed random move only depends on the current state. This Markov chain of configurations is constructed such that the probability of visiting a particular point $\mathbf{x}_1$ is proportional to its Boltzmann factor $\exp[-\beta u(\mathbf{x}_1)]$. The algorithm is as follows:

1. Within the current configuration of energy u_a, a particle i is selected at random.
2. Propose a random perturbation (with an equal probability of either a translational or rotational move) of particle i and calculate the new energy u_b.
3. Accept or reject the move (if $u_b < u_a$ then accept, otherwise accept with a probability

of $\exp[-\beta\Delta u]$ where Δu is the difference in energy $u_b - u_a$).

4. End after a set number of iterations or go to step 1.

Note each Monte Carlo cycle consists of N trial moves, of which the maximum step sizes are fixed, in order to obey detailed balance. Rotational moves are performed by generating a random unit vector and a random angle (up to a predefined maximum step size), then quaternion multiplication is used to rotate about this axis by the random angle.

2.4 Bonding analysis

The following sections detail analysis that is performed in relation to the bonding within systems of patchy particles. The nature of these patchy particles – with their highly directional interactions – make them well-suited to this type of analysis since a given structure can be readily and unambiguously converted into a well-defined network. In this work, a negative pairwise interaction energy ($V_{ij} < 0$) is used define a bond between two particles.

2.4.1 Constructing bonding graphs

The first step of any bonding analysis involves the construction of bonding graphs, in which particles and the bonds between them are considered as nodes and edges respectively. The bonds within these graphs are defined as pair interactions with negative potential energy ($V_{ij} < 0$). These graphs contain information related to any structure or lack thereof within a system.

The bonding graphs are represented as adjacency matrices, and for systems of particles where each particle has n patches, n adjacency matrices are constructed – one for each patch.

Note that whether any of the n patches are identical or not is irrelevant, the importance of constructing multiple matrices is to obtain information about bonds formed not only by a given particle but by a given patch.

The following example considers two-patch particles, each with one red and one blue patch, and as such two adjacency matrices G and H are constructed representing directed graphs of the red and blue patch bonding respectively. Figure 2.2**a** shows an example system of particles where bonds are shown in black. Figure 2.2**b** shows its constituent red and blue patch directed bonding graphs and their corresponding adjacency matrices, along with the complete bonding matrix C which represents an undirected graph of all bonds in the system – which is simply obtained by summing the patch specific matrices together ($G + H = C$).

A convention is followed such that for the adjacency matrix A, the element $A_{i,j}$ represents edges/bonds from i to j, where i is the row and j is the column. The bonding between particles 3 & 7 demonstrates the directed nature of these bonding graphs, since the bond between 3 & 7 is formed from the red patch on 3 and the blue patch on 7 (Particle 3 is bonded to 7 *via* its red patch, so in the red bonding matrix $G_{3,7} = 1$, but 7 does not bond to 3 *via* its red patch therefore $G_{7,3} = 0$ and $G_{3,7} \neq G_{7,3}$). Under this convention the out-degree of a given node i (i.e., the number of bonds particle i participates in with respect to a specific patch), is given by the sum of row i in that patches adjacency matrix:

$$\sum_{j=1}^{N} A_{i,j} \tag{2.11}$$

where N is the number of particles in the system. It follows that the total number of bonds i participates in is simply the sum over all patch matrices.

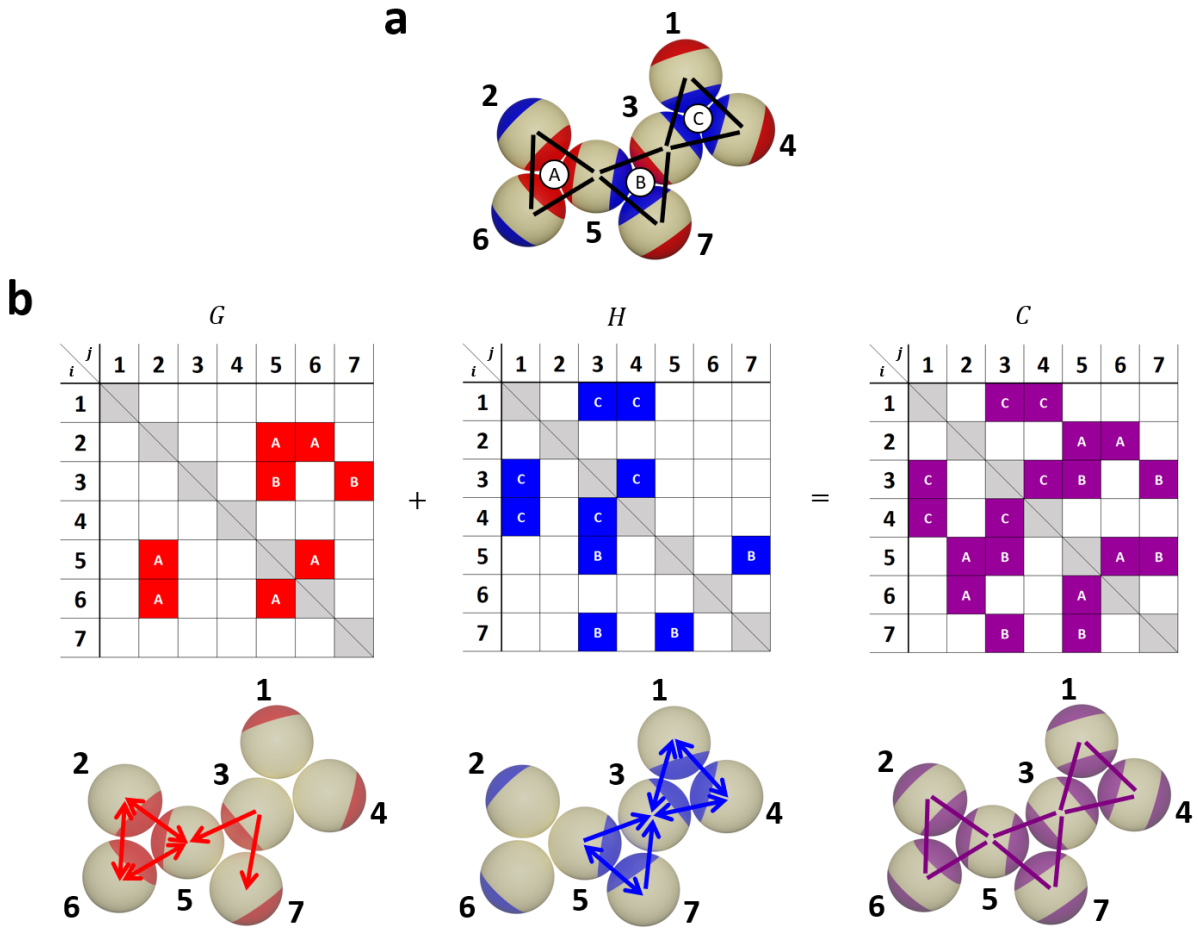


Figure 2.2: **Constructing directed bonding graphs.** (**a**) Example system of numbered 2-patch particles, each with one red and one blue patch, where bonds are shown in black and the three trigonal units formed are labelled A, B and C. (**b**) Substituent directed bonding graphs, G and H, along with their corresponding adjacency matrices for red and blue patches respectively. The sum $G + H$ gives the complete bonding matrix C, which is also shown with its corresponding graph.

2.4.2 Trigonal unit identification

In terms of trimer-forming patches, trigonal units are defined as 3-membered rings in the bonding graph, which are formed from 3 patches, where each patch participates in exactly 2 bonds. Trigonal units are therefore identified using the following criteria:

1. Particles form a 3-membered ring *via* 3 patches.

$$A^{\mathrm{p}}_{i,j} = A^{\mathrm{p}}_{i,k} = 1, \quad A^{\mathrm{p}'}_{j,i} = A^{\mathrm{p}'}_{j,k} = 1, \quad A^{\mathrm{p}''}_{k,j} = A^{\mathrm{p}''}_{k,i} = 1 \tag{2.12}$$

2. Each patch participates in exactly 2 bonds.

$$\sum_{x=1}^{N} A^{\mathrm{p}}_{i,x} = \sum_{x=1}^{N} A^{\mathrm{p}'}_{j,x} = \sum_{x=1}^{N} A^{\mathrm{p}''}_{k,x} = 2 \tag{2.13}$$

where A^{p} is the patch p adjacency matrix. Note p, p′, and p″ need not be different.

The criterion of each participating patch forming exactly 2 bonds is necessary to avoid over-counting due to larger clusters such as tetramers, where a tetrahedral arrangement results in four fused 3-membered rings.

The treatment outlined here is appropriate for "two-bond" patches (e.g., circular patches in Section 3.2.4 and rectangular patches in Section 4.2.4), whereas one-bond patches such as those considered in Section 5.2.2 are subject to alternative criteria. These alternative criteria are that 3-membered rings are formed *via* 6 patches and each patch participates in 1 bond.

2.4.3 Dihedral angle analysis

Throughout this thesis the measurement of dihedral angles is used to analyse the local structure of corner-shared trimer networks. The first step of this analysis is to calculate the bonding graph corresponding to the system under consideration, where each node represents a particle, and edges represent direct bonds between these particles (using the criteria of a pairwise interaction energy < 0 to define a bond between two particles).

The dihedral angles of specific interest are those defined by the planes of two adjacent trimers – the inter-trimer dihedral angles. In a perfect gyroid crystal this angle is equivalent to that of the dihedral angle defined by any three consecutive edges in its corresponding enantiomorph of Laves graph, and is given by $\cos^{-1}(1/3) \approx 70.5°$ [96]. To define these dihedrals, the edges within the would-be equivalent to Laves graph defined by trimer centres alone are not considered since this approach would require a 13-particle motif to calculate each dihedral angle. Instead dihedrals are defined using 5-particle motifs which only require the consideration of the directly bonded neighbours of a given particle, hence allowing for a more local characterisation.

If a particle has 4 bonds and is involved in the direct formation of two trimer units it satisfies the requirement for calculation of its associated dihedral angle. Figure 2.3**a** shows how the dihedral angles are defined for a given such particle X. Six points are defined in total with each of the four neighbours considered points A, B, C, and D; as well as the centres of mass of the two trimers T and R. These six points are then used to define four dihedral angles $ATRC$, $ATRD$, $BTRC$, and $BTRD$ about the inter-trimer axis $\overrightarrow{TR}$. Note that due to the deformations present in thermalised systems, four distinct dihedrals must be defined to characterise each particle since if A, B, T, and R or T, R, C, and D are not coplanar then the four dihedrals are not equivalent.

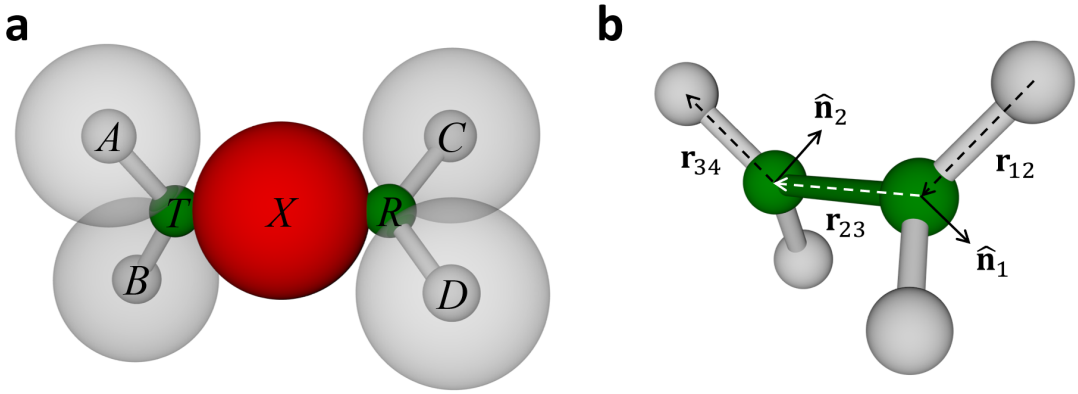


Figure 2.3: **Dihedral angle determination.** (**a**) Schematic illustrating how dihedral angles are defined for a four-coordinated particle X involved in two trimers, shown in red. The four neighbours of X, namely A, B, C and D, are shown in translucent gray, along with T and R (shown in green), which are the geometric centres of trimers formed by A, B and X, and by C, D and X, respectively. (**b**) Schematic showing the vectors associated with the calculation of a dihedral angle defined by a set of four sequential points.

Each particle is therefore characterised by an average of these four angles, and each angle is defined by three vectors $\mathbf{r}_{12}$, $\mathbf{r}_{23}$, and $\mathbf{r}_{34}$ as shown in Figure 2.3**b**. The dihedral angle defined by these vectors is calculated using the normals $\hat{\mathbf{n}}_1$ and $\hat{\mathbf{n}}_2$ to the planes defined by $\mathbf{r}_{12}$, $\mathbf{r}_{23}$ and $\mathbf{r}_{23}$, $\mathbf{r}_{34}$ respectively.

$$\hat{\mathbf{n}}_1 = \frac{\mathbf{r}_{12} \times \mathbf{r}_{23}}{|\mathbf{r}_{12} \times \mathbf{r}_{23}|}, \quad \hat{\mathbf{n}}_2 = \frac{\mathbf{r}_{23} \times \mathbf{r}_{34}}{|\mathbf{r}_{23} \times \mathbf{r}_{34}|} \tag{2.14}$$

The dihedral angle ω_i is then given by:

$$\sin(\omega_i) = (\hat{\mathbf{n}}_1 \times \hat{\mathbf{n}}_2) \cdot \hat{\mathbf{r}}_{23} \tag{2.15}$$

$$\cos(\omega_i) = \hat{\mathbf{n}}_1 \cdot \hat{\mathbf{n}}_2 \tag{2.16}$$

By defining every dihedral in the same manner and considering both $\sin(\omega_i)$ and $\cos(\omega_i)$, the

chirality of a given environment can be extracted [108]. Averaging over the four dihedrals for a given particle, as appropriate for circular data [109], gives the dihedral angle ω as:

$$\omega = \tan^{-1}\left(\frac{\sum_{i}^{4}\sin(\omega_i)}{\sum_{i}^{4}\cos(\omega_i)}\right) \tag{2.17}$$

2.4.4 Rings

Distributions of the number of rings (N_{R_l}) with sizes $l \in [5-12]$, in systems of patchy particles were computed from their bonding graphs. Rings are defined as closed paths in this graph (i.e., paths whose first and final vertices are the same), and, for each vertex in the graph, all such distinct paths are determined using a depth-first search (DFS) traversal up to the chosen maximum ring size. Paths with edges between non-adjacent vertices along the path are rejected to ensure any potential ring does not contain any internal edges, however the rings identified are not necessarily base rings (i.e., rings that cannot be broken into smaller rings). In order to avoid over-counting the number of rings in the system and improve the efficiency of the analysis, following the extraction of all relevant paths starting from a given vertex, all edges connected to that vertex are removed from the graph prior to initiating the DFS traversal from the next vertex. Finally the double counting of rings, which arises due to the undirected nature of the complete bonding graph, is accounted for.

2.5 Steinhardt order parameters

In order to determine the crystallinity of a system the global Steinhardt bond-order parameter Q_l is used [110, 111]. Q_l is commonly used to distinguish between liquid-like and

crystalline phases because typically for liquid-like phases $Q_l \approx 0$ and for crystalline phases $Q_l > 0$.

First the local environment of each particle is characterised by:

$$q_{lm}(i) = \frac{1}{N_{\mathrm{B}}(i)} \sum_{j=1}^{N_{\mathrm{B}}(i)} Y_{lm}(\mathbf{r}_{ij}) \tag{2.18}$$

where $N_{\mathrm{B}}(i)$ is the number of first nearest-neighbours of particle i, $\mathbf{r}_{ij}$ is the vector connecting the centres of particles i and j, and Y_{lm} is the spherical harmonic with total angular momentum l and projection $-l \leq m \leq l$. The global bond-orientational order parameter is then defined as:

$$Q_{lm} = \frac{\sum_{i \in N} N_{\mathrm{b}}(i) q_{lm}(i)}{\sum_{i \in N} N_{\mathrm{b}}(i)} \tag{2.19}$$

where rotationally invariant combinations [112] can then be constructed:

$$Q_l = \sqrt{\frac{4\pi}{2l+1} \sum_{m=-l}^{l} |Q_{lm}|^2} \tag{2.20}$$

Chapter Three

Reverse Engineering Single Network Gyroid & a Library of Trimer-Based Colloidal Open Crystals

3.1 Introduction

Colloidal particles with modified surface chemistry in the form of attractive patches have proven to be versatile building blocks for realising diverse open crystals [64, 66, 67]. In colloidal open crystals, the colloidal particles are rather low-coordinated, corresponding to a density that is significantly lower than what is achieved at close packing. The tunability of colloidal interactions can be exploited for the design of bottom-up routes to colloidal open crystals, which have a variety of potential applications ranging from photonic crystals to bio-separation [113, 114]. The sheer variety of building blocks increases the need and importance of computational studies to guide and inform experimental work. In the context of colloidal crystals, much work has been done on predicting the resulting structures and self-assembly behaviour of various building blocks including hard [115], patchy [65–67], and

multicomponent systems [25].

In the search for bottom-up routes to 3D photonic crystals, targeted self-assembly of cubic diamond-related structures have been the major focus due to cubic diamond possessing the largest known 3D photonic band gap [27, 75] and having intuitive links to building blocks with tetrahedral symmetry [72, 86, 87]. The single gyroid structure has been thus-far ignored in this context – despite possessing the 2nd largest known 3D band gap [27] – likely due to its complex geometry and chirality which requires enantiomorph selection. This chirality however, sets gyroid apart from other photonic structures with large 3D photonic band gaps [27] and makes single gyroid an attractive and unique target structure with potential applications as a chiral photonic crystal and metamaterial at optical frequencies [92–94].

In this chapter we present our approach to reverse-engineer the single network gyroid structure, discretising it into spherical building blocks, and proposing rationally designed and synthetically viable surface modifications in the form of attractive patches which can stabilise the proposed crystal structures. Crystal structure prediction was then performed on these patchy particles to generate a library of trimer-based open colloidal crystals. Finally, Monte Carlo simulations were performed in order to investigate the self-assembly behaviour of these trimer-forming patchy particles in 3D.

3.2 Results and discussion

3.2.1 Reverse engineering single network gyroid

Figure 3.1 presents the discretisation of a single network gyroid structure into colloidal spheres. The Wigner–Seitz cell of a single network gyroid structure (Figure 3.1**a**) can be mapped onto a skeletal graph (Figure 3.1**b**), known as Laves graph, which represents the connectivity of single network gyroid. Laves graph can then be used to propose crystals comprised of discrete building blocks, which retain the core structure of single gyroid. We envisaged patchy spheres with requisite numbers of circular patches of an appropriate size as to not only stabilise these structures, but also direct the particle interactions such that these crystals could potentially be self-assembled. Figure 3.1**c** shows "colloidal K_4" [96] which is obtained by placing a sphere with three trigonally arranged patches, each forming a single patch-patch contact, at each node. Figure 3.1**d** shows "colloidal gyroid" where a triblock patchy sphere with equal-size patches on opposite poles, each forming two patch-patch contacts (trigonal units), is placed at the midpoint of each edge. Figure 3.1**e** shows "colloidal trigonal K_4" where two spheres, each with two different-size patches where one patch (blue) forms one patch-patch contact and another patch (red) forms two contacts (trigonal units), are placed on each edge such that discrete trigonal units are centred on each node.

It is important to note that the surface modifications here, in the form of attractive patches on the surface of the particles, are proposed in the context of state of the art synthetic methodology and each are experimentally viable [43, 116].

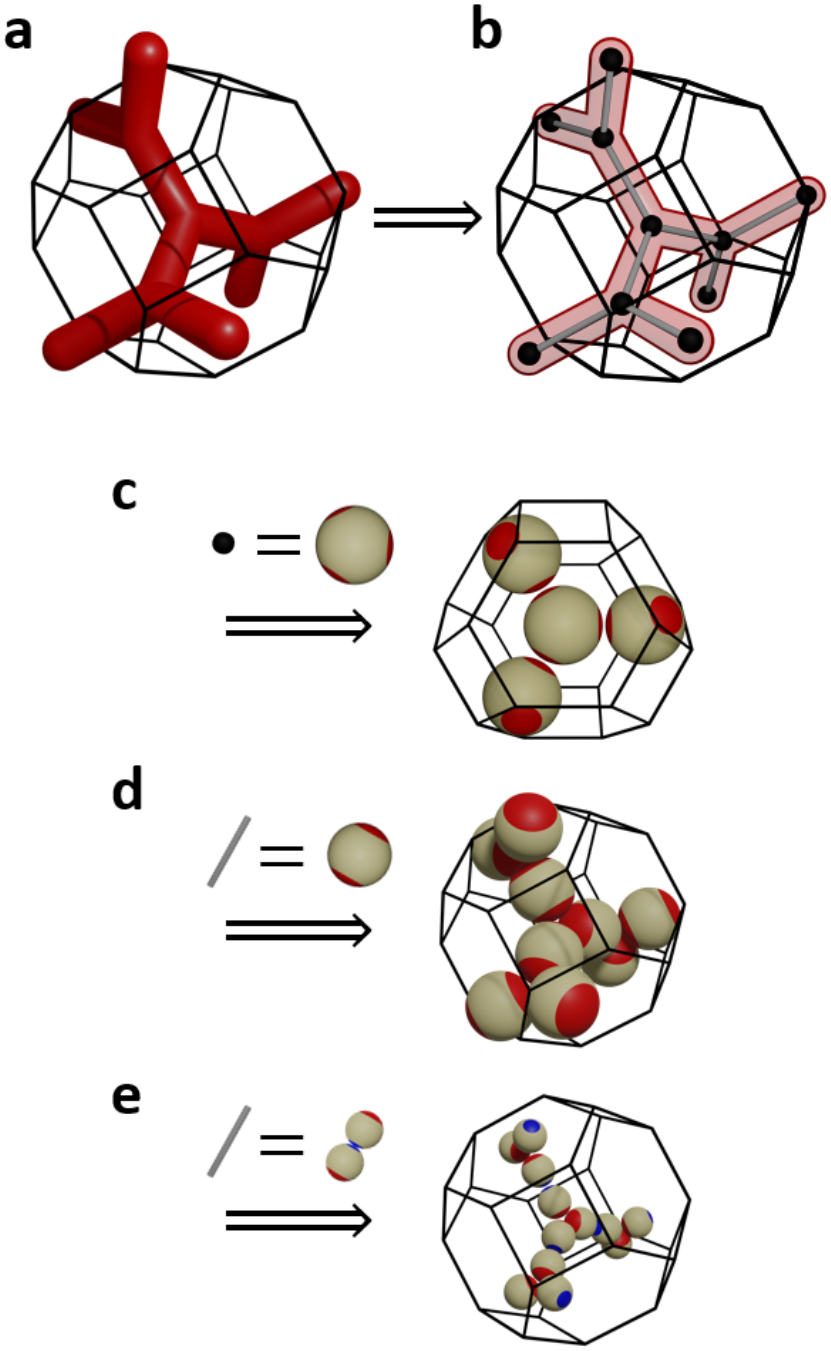


Figure 3.1: **Reverse engineering of single network gyroid.** Showing WS cells of: (**a**) single network gyroid, (**b**) Laves graph (superimposed onto single network gyroid), (**c**) "colloidal K_4", (**d**) "colloidal gyroid", and (**e**) "colloidal trigonal K_4".

3.2.2 Corner-shared trimer crystal structures

In order to determine the existence of any competing crystal structures to single colloidal gyroid, in the context of the building blocks proposed in Section 3.2.1, crystal structure prediction was performed for trimer-forming triblock patchy spheres (Figure 3.1**d**). To this end, the interactions between the triblock patchy spheres were modelled using a continuous pair potential [85] detailed in Methodology (Section 2.1.2).

Firstly, since colloidal gyroid is stabilised by patches which form trimer units, an appropriate patch coverage which energetically favours forming two patch-patch contacts was determined. Basin-hopping global optimisation [105] (see Methodology Section 2.2) was performed on finite systems of 2, 3, and 4 particles to determine the energies of correspondingly sized clusters. These clusters were then optimised with patch half-opening angles of $\theta = 50°, 60°, 70°$, and $80°$ and their energies U are plotted as a function of θ in Figure 3.2.

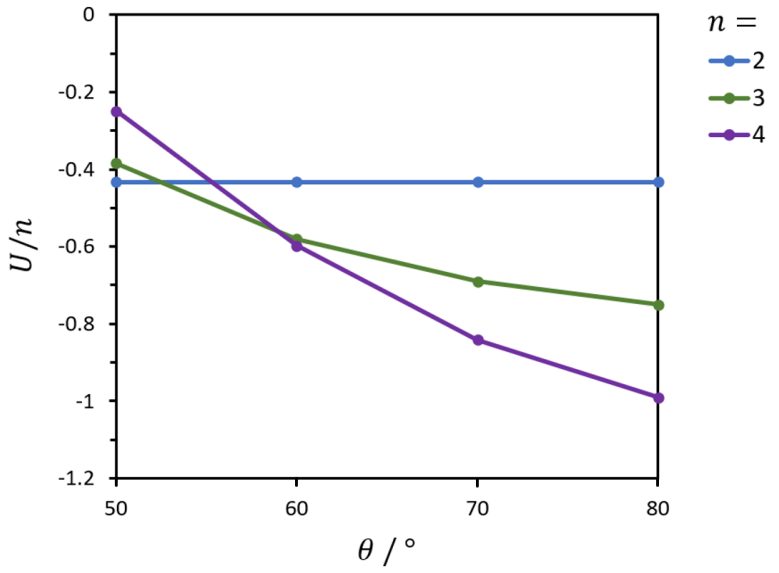


Figure 3.2: **Per-particle energy of dimer, trimer, and tetramer clusters as a function of patch half-opening angle** θ, where $\epsilon = 1$, $s = 10$, $\kappa = 100$, and n is the size of the cluster.

It then follows that patches corresponding to $\theta \approx 55^\circ$ are most suitable, in terms of energetics, for obtaining trimer-based crystal structures. Crystal structure prediction (see Methodology Section 2.2.1) was therefore performed for unit cells containing $Z = 3$, 6, 9, 12, 15, and 18 particles with $\epsilon = 1$; half-opening angles of $\theta = 55^\circ$ and 60°; $s = 5$, 8, and 10; and $\kappa = 50$, 100, and 250. Six isoenergetic crystal structures were identified: gyroid, double gyroid, kagome, Fddd, Cccm, and C2/m. These crystal structures are shown in Figures 3.3-3.8 in terms of their unit cells, and are discussed in more detail in the following subsections. Note the unit cells shown and densities quoted in the following subsections correspond to particles where $\epsilon = 1$, $\theta = 60^\circ$, $s = 10$, and $\kappa = 100$.

Since the building blocks are optimised to form trigonal units *via* their attractive patches, the connectivity of these crystals in this sense is identical, where each particle participates in the formation of a trigonal unit on each of its hemispheres (i.e., the crystals are all fully connected arrangements of corner-shared trigonal units). This section uses two effective methods of structure characterisation which can also be used to quantitatively distinguish the crystals from each other. One method calculates the distribution of rings within the crystal (see Methodology Section 2.4.4), by constructing a bonding graph where nodes represent particles and edges represent the bonds between them. The other method calculates the distribution of dihedral angles within the crystal which are formed between two adjacent trigonal units (see Methodology Section 2.4.3).

3.2.2.1 Colloidal gyroid and double colloidal gyroid

As expected, the colloidal gyroid structure was identified. Both enantiomorphs were identified and Figure 3.3 shows the cubic unit cell of the right-handed enantiomorph. The structure consists solely of fused 10-membered rings, and the dihedral angles between adjacent trigonal units are all approximately equal to either 70.5° or 109.5° (depending on the enantiomorph).

Both enantiomorphs possess the $I4_132$ space group.

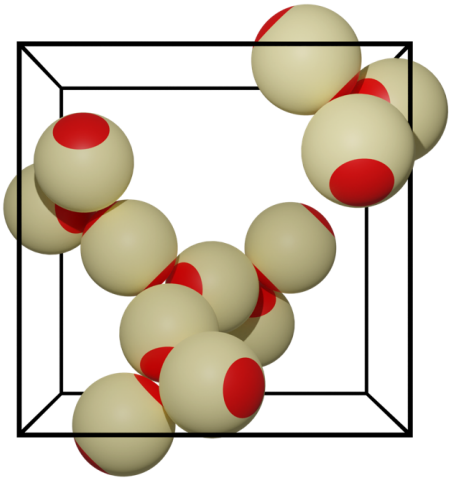


Figure 3.3: **Cubic unit cell of right-handed single colloidal gyroid**, where dihedral angles are approximately 70.5°.

The optimal density obtained from crystal structure prediction is $\rho^* \approx 0.3169$, which is low enough to support interpenetrating structures such as double gyroid. Consequently the double colloidal gyroid structure was also identified and its cubic unit cell is displayed

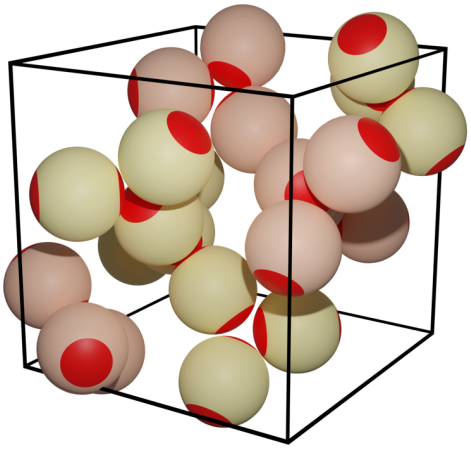


Figure 3.4: **Cubic unit cell of double colloidal gyroid**, where the left-handed and right-handed single gyroid networks with dihedral angles of approximately 109.5° and 70.5° are shaded pink and yellow respectively.

in Figure 3.4. The structure consists of two interpenetrating crystals of single gyroid, where the single networks are of opposing chirality. It therefore follows that the fused 10-membered rings are retained from the constituent single gyroid networks, the density doubles, and the overall dihedral angle distribution for double gyroid is half with 70.5° and the other half with 109.5°. The double gyroid crystal is achiral and possesses the $Ia\bar{3}d$ space group.

3.2.2.2 Kagome

A kagome crystal, equivalent to that which has been self-assembled experimentally by Chen et al. [64], was identified and a rectangular supercell of the structure is shown in Figure 3.5. The 2D crystal consists solely of fused 6-membered rings and the ideal dihedral angles are all equal to 0°. In 3D the discrete 2D kagome sheets stack to give a variable density up to $\rho^* \approx 0.9$.

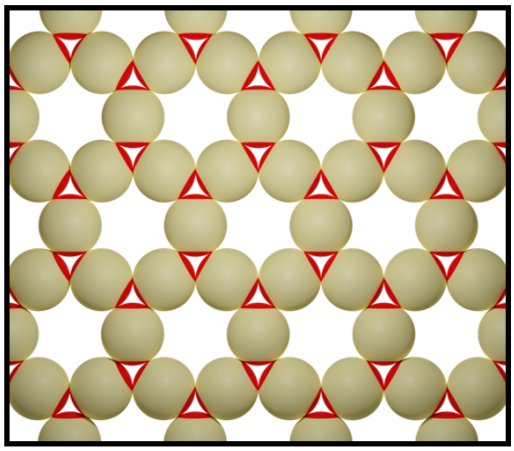


Figure 3.5: **Rectangular supercell of kagome.**

3.2.2.3 Fddd

A crystal consisting of fused 10- and 12-membered rings, possessing the $Fddd$ space group, was identified. This crystal is achiral with an ideal dihedral angle distribution of two-thirds with 0°, one-sixth with $+x$, and the remaining one-sixth with $-x$ (where $x \geq$ some critical value at which the crystal collapses onto itself). A consequence of this is that the structure has a variable density which is minimal when $+x \equiv -x$ (i.e., $x = 90°$), Figure 3.6 shows an orthorhombic supercell where $x = 60°$ corresponding to a density of $\rho^* \approx 0.4572$. The structure is achiral and x can alter continuously with zero patch-patch potential energy change, meaning that the structure can undergo significant changes in density without breaking any bonds.

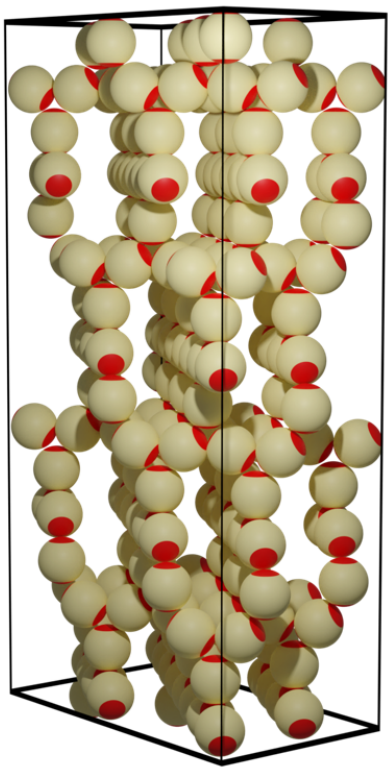


Figure 3.6: **Orthorhombic supercell of Fddd**, where $x = 60°$.

3.2.2.4 Cccm

A crystal possessing the *Cccm* space group, which consists of fused 6- and 10-membered rings, was identified. The achiral crystal has a density of $\rho^* \approx 0.7493$ and an ideal dihedral angle distribution of one-sixth with 0°, five-twelfths with approximately 15.6°, and five-twelfths with approximately −15.6°. An orthorhombic supercell of the structure is shown in Figure 3.7.

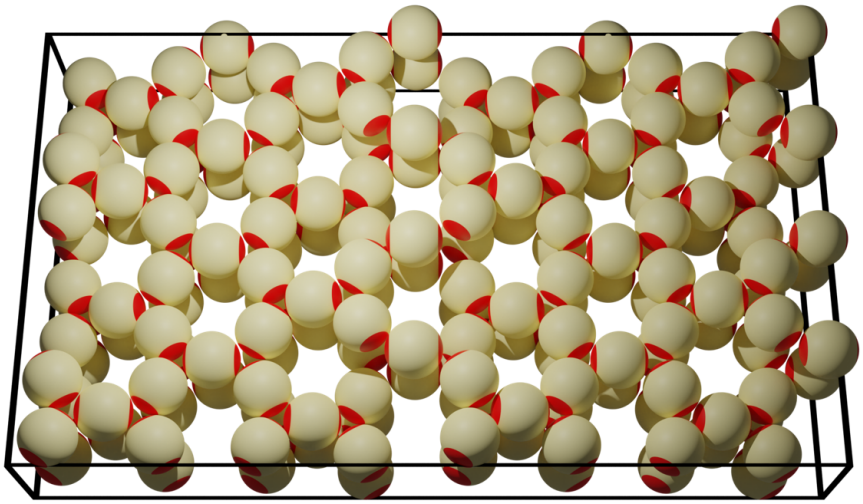


Figure 3.7: **Orthorhombic supercell of Cccm.**

3.2.2.5 C2/m

A crystal consisting of fused 6-, 8- and 10-membered rings, which possesses the $C2/m$ space group, was identified. The crystal has an ideal dihedral angle distribution of two-thirds with 0°, and one-third with 90°. The structure is achiral and has an ideal density of $\rho^* \approx 0.2898$. A monoclinic supercell is displayed in Figure 3.8.

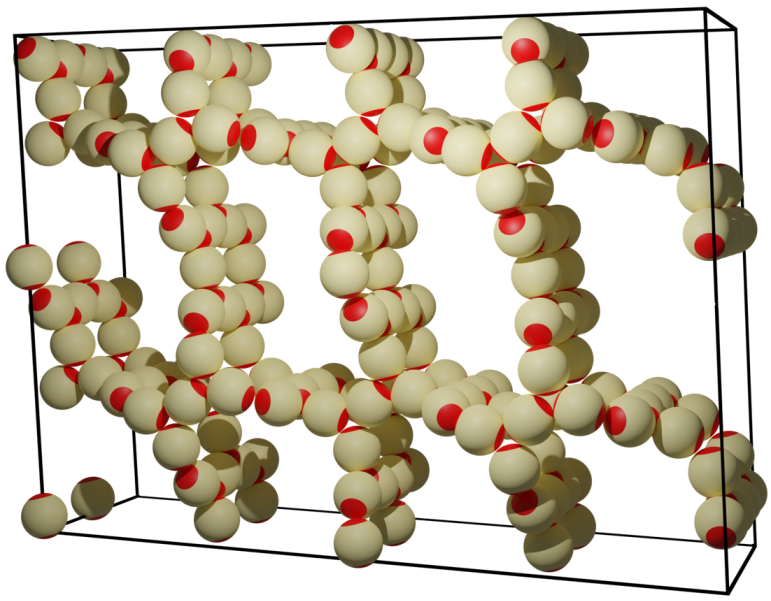


Figure 3.8: **Monoclinic supercell of C2/m.**

3.2.3 Analogous crystal structures

In the section above (Section 3.2.2), crystal structures comprised of triblock patchy spheres with two equal-size patches, as considered in Figure 3.1**d**, were explored. Since all three building blocks proposed in Figure 3.1 are fundamentally related, analogous crystal structures to those detailed for corner-shared trimers can be obtained. This conversion is demonstrated for single gyroid in Figure 3.1 itself (i.e., by replacing each particle in colloidal gyroid with two particles to obtain colloidal trigonal K_4 etc.). In other words, as long as the density permits, each crystal has analogues in the other two systems. It is worth noting that since the trigonal K_4 system (Figure 3.1**e**) has a significantly lower density, it is able to support higher levels of interpenetration, as demonstrated in Figure 3.9, which shows a cubic supercell of quadruple trigonal K_4 consisting of four interpenetrating single trigonal K_4 networks of the same chirality.

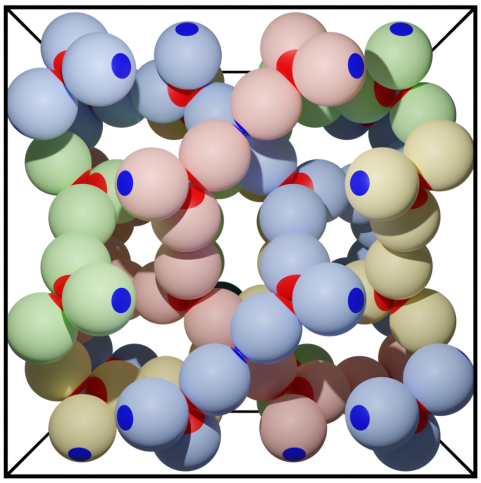


Figure 3.9: **Cubic supercell of right-handed quadruple trigonal** K_4, where dihedral angles are approximately 70.5°, and each single network is shaded in a different colour.

3.2.4 Monte Carlo simulations

In order to predict which crystal forms, if any, from the patchy particles under consideration for the targeted self-assembly of single colloidal gyroid (Figure 3.1**d**), Monte Carlo simulations were performed using the widely used Kern-Frenkel potential [104] detailed in Methodology (Section 2.1.1). Unlike the potential considered for the purpose of global optimisation for structure prediction, the Kern-Frenkel potential is computationally less intensive at the expense of discontinuous patch-patch interactions. For the Kern-Frenkel potential, the patch sizes tend to be smaller for equivalent typical coordination because of its square-well character.

First, sets of Monte Carlo simulations in the NVT ensemble were performed in order to determine optimal patch coverages for the formation of the desired bonding motif (i.e., trigonal units). Sets of $N = 1000$ one-patch particles with half-opening angles from $\theta = 30°$ to 40° with a resolution of 2°, were gradually annealed at a density of $\rho^* = 0.3$. The equilibrated fraction of particles forming trigonal clusters as a function of temperature T^*,

for each system, is displayed in Figure 3.10. From this it was concluded that patch half-opening angles from $\theta = 32°$ to $36°$ were optimal for the formation of trigonal units, and hence optimal for the formation of corner-shared trimer crystal structures.

A subsequent series of simulations were performed in order to investigate the self-assembly behaviour of corner-shared trimer-forming patchy particles – which can theoretically stabilise a single gyroid crystal. As such, sets of $N = 768$ patchy particles possessing a circular patch on each hemisphere with half-opening angles $\theta = 32°$, $34°$, and $36°$ were subjected to one-step quenching from $T^* = 1$. Self-assembly of stacked kagome planes is observed for $\theta = 34°$ and $36°$, with Figure 3.11 showing data for a $\theta = 34°$ system. To probe the progression of the self-assembly, the number of trigonal units N_{trig} is tracked and is shown along with the potential energy per particle U^*/N after the temperature is dropped in Fig-

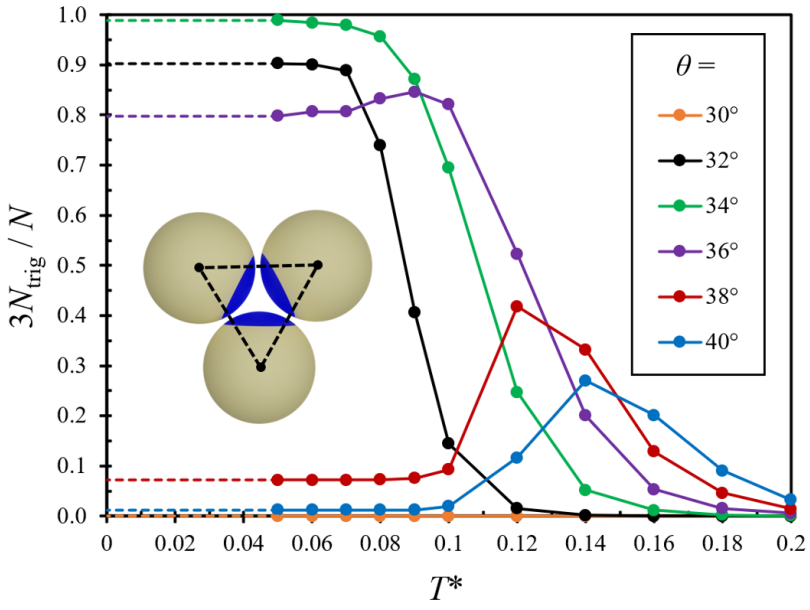


Figure 3.10: **Optimising circular patches to form trimers.** Fraction of particles forming trigonal planar clusters as a function of the temperature T^* for systems of $N = 1000$ one-patch particles at a density of $\rho^* = 0.3$ with different half-opening angles θ, where N_{trig} is the number of trigonal planar clusters.

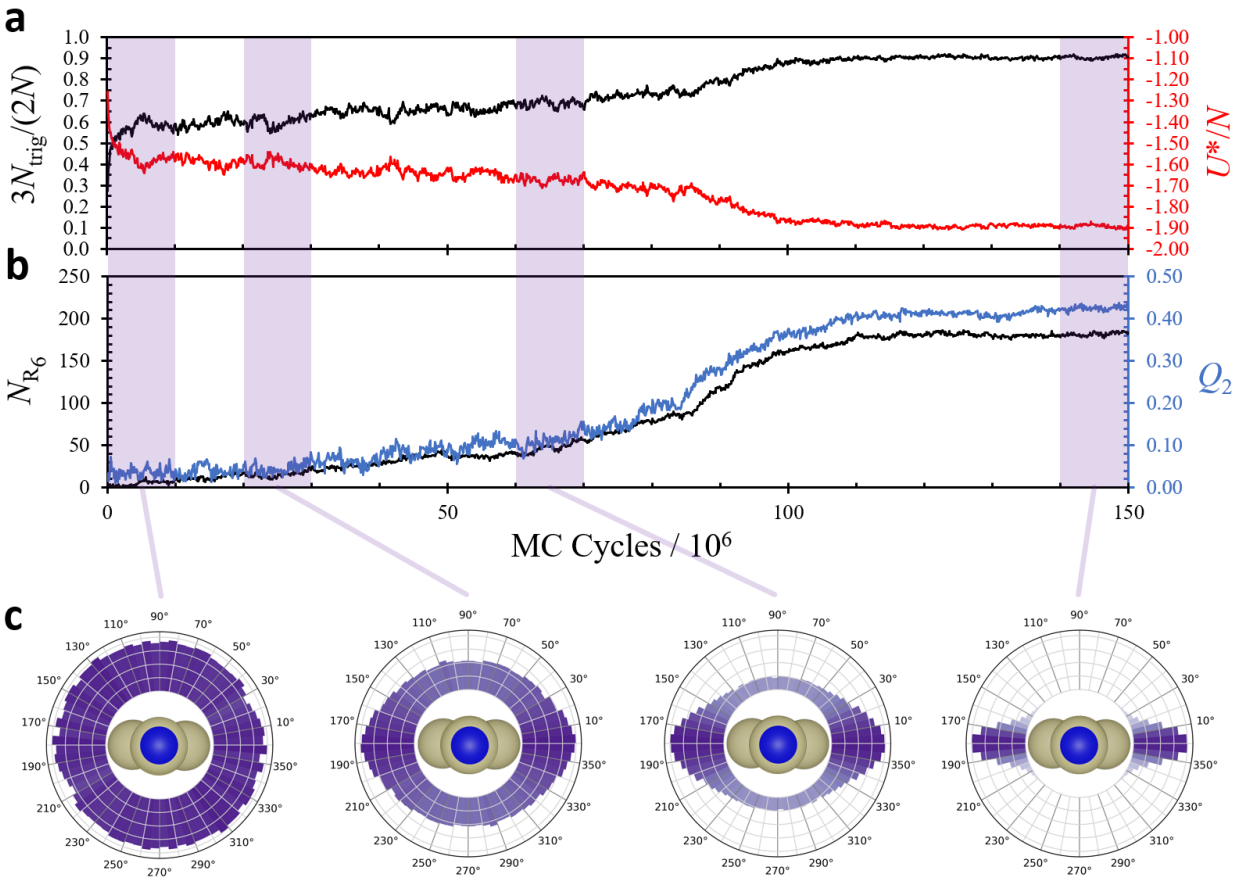


Figure 3.11: **Self-assembly of stacked kagome planes.** (**a**) Evolution of the number of trigonal planar units (N_{trig}) along with the potential energy per particle (U^*/N), for a system of $N = 768$ triblock patchy particles with patch half-opening angles of $\theta = 34°$ following a one-step quench from $T^* = 1$ to $T^* = 0.11$. (**b**) Evolution of the global Steinhardt bond-order parameter Q_2 and the number of 6-membered rings (N_{R_6}), along the same trajectory. (**c**) Polar histograms of the inter-trimer dihedral angles for four equal intervals of 10 million MC cycles along the trajectory, as indicated by the purple shading in **a** and **b**.

ure 3.11**a**. The drop in energy and corresponding rise in trigonal unit count indicated a phase transition had occurred, and the final ring distribution showed practically all 6-membered rings confirming that a kagome crystal had formed. The 6-membered ring count and global Steinhardt bond-order parameter Q_2 are effective order parameters for the transition, and their evolution is shown in Figure 3.11**b**.

To further probe the evolution of local order within the system, the dihedral angle distribution was calculated at various intervals throughout the simulation and the results of this are shown as polar histograms in Figure 3.11**c**. Initially the distribution is uniform until a slight preference for shallow angles (around 0°) appears, which then gradually becomes more pronounced as the crystal grows and the emergence of long range order limits fluctuations from the ideal kagome angle. Figure 3.12**a** shows a representative configuration pre-nucleation, displaying its interconnected structure and random dihedral angles, and Figure 3.12**b** shows a representative crystalline configuration with a zoom-in of the 6-membered ring substructure.

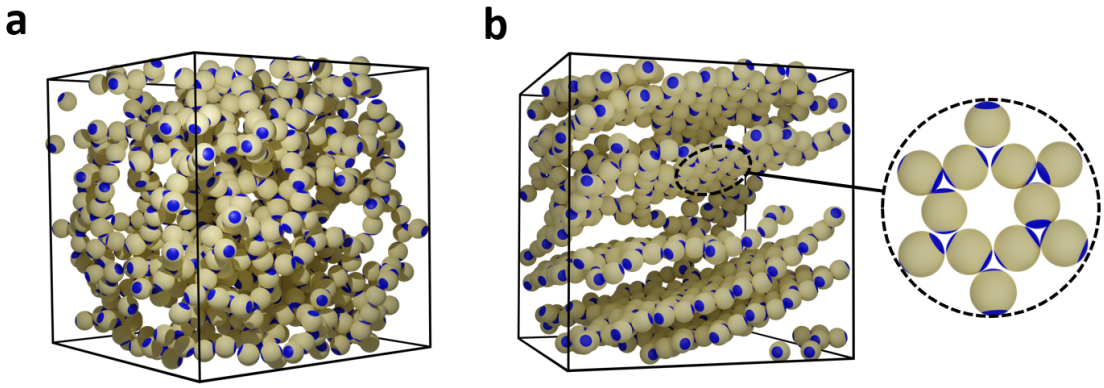


Figure 3.12: **Self-assembly of stacked kagome planes snapshots.** (**a**) Representative pre-nucleation configuration (after 10 million MC cycles) (**b**) Representative crystalline configuration comprising stacked kagome planes. The zoom-in highlights a typical 6-membered ring.

3.3 Conclusions

This chapter presents a reverse engineering approach, which proposes a transformation of the single network gyroid structure into three single gyroid colloidal crystal structures built from discrete spherical building blocks. In the context of self-assembling a single gyroid photonic crystal on the colloidal scale, surface modifications in the form of attractive patches on the surface of the spheres are proposed in order to stabilise said target colloidal crystals. These designer patchy particles are also proposed in line with experimental advancements in colloidal particle synthesis [43, 116]. The "colloidal gyroid" case, where the particles are trimer-forming triblock patchy spheres, is then used as a basis for crystal structure prediction *via* the basin-hopping global optimisation technique [105]. This crystal structure prediction identifies the colloidal gyroid structure as a minimum on the potential energy landscape along with various competing trimer-based crystal structures which are characterised. Monte Carlo simulations are then performed to predict the self-assembly behaviour of trimer-forming triblock patchy particles in 3D. It is shown that a careful selection of the half-opening angle (approximately in the range of $32^\circ \leq \theta \leq 36^\circ$) of the circular patches on each hemisphere can be optimised to overwhelmingly favour contacts with only two other patches, thereby giving rise to the trigonal unit formation required to self-assemble a corner-shared trimer-based crystal, such as colloidal gyroid. Further simulations, however, show that designer triblock patchy particles with circular patches do not self-assemble into a gyroid structure and instead form stacked kagome planes. Self-assembly of these kagome planes *in silico* is observed for systems of particles with $\theta = 34^\circ$ and 36°, additionally the formation of trigonal units, 6-membered rings, and shallow dihedral angles is identified as key to the self-assembly of the crystal structure.

Chapter Four

Developing a Pair Potential for Spheres With Rectangular Patches & Investigating Their Self-Assembly

4.1 Introduction

Motivated by the failure to self-assemble single colloidal gyroid from spherical particles with two circular patches in Chapter 3, this chapter first proposes that the use of non-circular patches in the form of rectangles can potentially restrict the dihedral angles that can form within the system – hence achieving structure selection.

Though previous work has been done regarding structure selection in the context of patchy particles [77, 78, 86], the specific use of non-circular patches is limited to those of a triangular nature [60]. Rectangular patches, whilst experimentally more challenging to synthesise than their circular counterparts, have literature precedent [63] and in fact glancing angle deposition onto a close-packed monolayer of particles can produce a variety of patch geometries [62]. In order to model rectangular attractive patches, a pair potential based

upon the principles of Kern-Frenkel [104] was developed and is detailed in this chapter. This model is then used to test the particle design principles of dihedral angle restriction and explore the self-assembly behaviour of particles with two rectangular patches at various skew angles.

4.2 Results and discussion

4.2.1 Enforcing trimer formation at a specific dihedral angle

In Chapter 3 the single network gyroid structure is reverse engineered into a discretised "colloidal gyroid" crystal consisting of spherical building blocks. With the aim of its self-assembly on the colloidal scale, synthetically feasible particles with trimer-forming circular attractive patches are proposed. Although Monte Carlo simulations investigating the self-assembly behaviour of these particles reveal that trigonal units can be readily formed, crystal structure prediction demonstrates that these particles can also stabilise a variety of trimer-based colloidal open crystals. Consequently, the resulting self-assembled structure is not colloidal gyroid but stacked kagome sheets instead.

It is identified that two key distinguishing features of the competing crystals are their ring, and inter-trimer dihedral angle distributions. It therefore follows that if control over either of these attributes can be obtained, then certain competing structures can be disfavoured.

Figure 4.1 shows a proposed method of obtaining inter-trimer dihedral angle control. Figure 4.1**a** first presents the patchy system explored in Chapter 3 where a circular patch of appropriate coverage to form trimer units sits on each hemisphere. The nature of the trimer units formed in this system are shown (middle) along with five-particle motifs (which

consist of two corner-shared trimers). A key feature of circular patches is that their rotational symmetry allows for the formation of two adjacent corner-sharing trimer units at any given dihedral angle between the trimer planes (as indicated by the dotted arrows which show the accessible states). Figure 4.1**b** shows a proposed system where the symmetry of the patches has been reduced such that they are rectangular. In this system a trimer-forming rectangular patch is centred on each hemisphere and trigonal bonding is restricted to a well-defined plane, a consequence of this is that the five-particle motifs formed in this system are restricted to a narrow range of angles as shown (right). This dihedral angle restriction is controlled directly by the relative orientation of the patches with respect to each other.

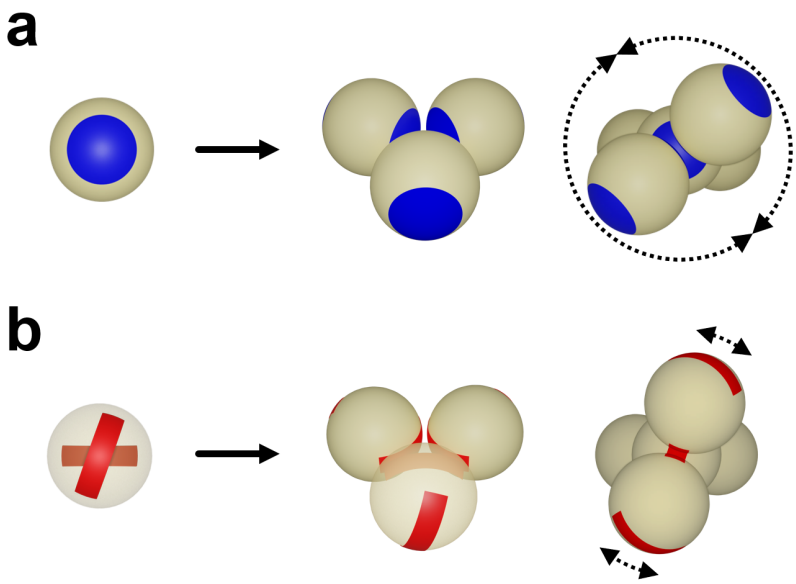


Figure 4.1: **Inter-trimer dihedral angle selection using rectangular patches.** Single particles and the nature of corresponding trigonal and five-particle motifs that they can form. (**a**) Particles with two trimer-forming circular patches. (**b**) Particles with two trimer-forming rectangular patches, where the core of the single particle and the front particle of the trigonal unit are shown in translucent to reveal the orientation of the patch on the back face. The dotted arrows around the five-particle motifs represent the accessible inter-trimer dihedral angles in each system.

If successful, the use of rectangular patches in this manner can essentially fix the inter-trimer dihedral angles that can form to a predetermined angle encoded into the building blocks. By choosing appropriate dihedrals, crystal selection can be achieved *via* the removal of competing structures from the energy surface.

4.2.2 Rectangular Kern-Frenkel

In order to model particles with rectangular patches, the angular component of the widely used Kern-Frenkel model [104] (detailed in Section 2.1.1) can be modified to account for the non-circular patch geometry.

4.2.2.1 Parametrising rectangular patches

In this modified model, the geometry and surface coverage of each patch p is defined by two half-opening angles θ_{p} and ϕ_{p}, which define the latitudinal and longitudinal bounds of the patch respectively on a spherical coordinate frame. Figure 4.2**a** shows this coordinate frame, how ϕ and θ are defined, and how these two angles can be used to define any point on the surface of a sphere. Latitudinal angles (θ) are defined with respect to the equator (shown in red), while longitudinal angles (ϕ) are defined relative to a reference known as the prime meridian (shown in green). Latitudinal lines are parallel great circles defined by points with a given θ value, where $\theta = 0$ defines the equator. Longitudinal lines are half great circles which connect the two poles, defined by points with a given ϕ value where $\phi = 0$ defines the prime meridian. Where the equator and prime meridian intersect defines (0, 0), which is taken to be the centre of the patch.

Figure 4.2**b-d** demonstrates how latitudinal and longitudinal line pairs can be combined to define quadrilateral regions on the surface of a sphere. Figure 4.2**b** shows longitudinal lines at 10° intervals, where the prime meridian is green, and the lines defined by $\phi = +20°$ and $-20°$ are shown in blue. Figure 4.2**c** shows latitudinal lines also at 10° intervals, where the equator is red, and the lines defined by $\theta = +10°$ and $-10°$ are shown in yellow. Figure 4.2**d** then shows how these latitudinal (yellow) and longitudinal (blue) lines can be combined to inscribe a patch (shaded in red), the geometry of which is characterised by the corresponding half-opening angle values of $\theta_p = 10°$ and $\phi_p = 20°$.

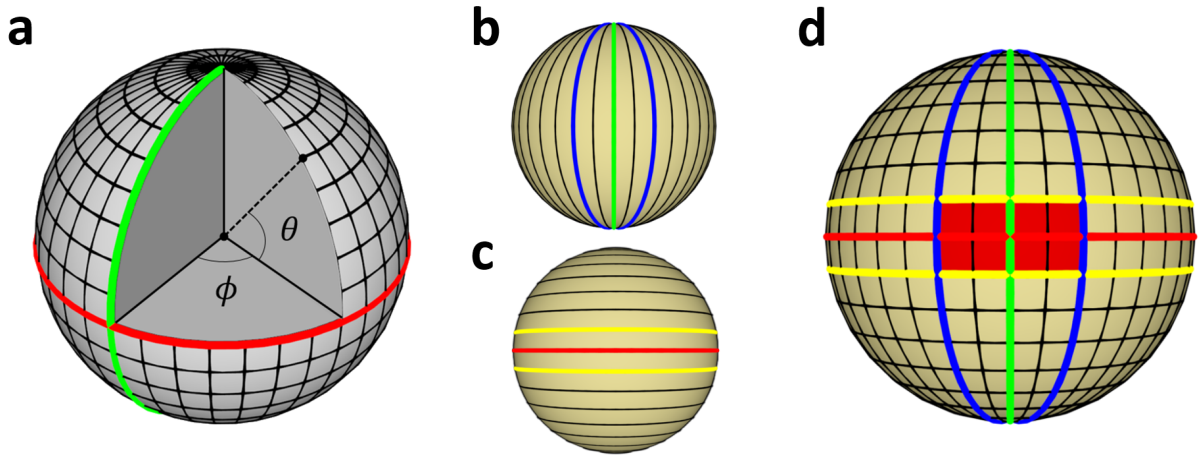


Figure 4.2: **Defining rectangular patches using latitudinal and longitudinal lines.** (**a**) Schematic illustration of the latitudinal angle θ, and longitudinal angle ϕ, where the lines at which $\theta = 0$ (the equator) and $\phi = 0$ (the prime meridian) are highlighted in red and green respectively. (**b-d**) Combination of longitudinal and latitudinal lines to define a rectangular patch where: longitudinal lines at $\phi = +20°$ and $-20°$ in blue inscribe a lune in **b**; latitudinal lines at $\theta = +10°$ and $-10°$ in yellow inscribe a zone in **c**; and **d** shows these together inscribing a patch shaded in red which corresponds to a latitudinal half-angle of $\theta_p = 10°$ and a longitudinal half-angle of $\phi_p = 20°$.

In this scheme each resulting patch can be thought of as being given by the overlap of a zone and a lune on the surface of the particle, where the zone is associated with θ_p and the lune with ϕ_p. As such, the parameter ranges that make geometrical sense are $0° \leq \theta_p \leq 90°$ and $0° \leq \phi_p \leq 180°$.

It is important to note that since θ_p and ϕ_p are distinct, corresponding to the latitudinal and longitudinal bounds respectively, the values of these half-angles are non-interchangeable when defining a patch geometry. In other words ($\theta_p = 60°$, $\phi_p = 20°$) defines a patch with a distinct geometry and orientation to that of one defined by ($\theta_p = 20°$, $\phi_p = 60°$) as displayed in Figure 4.3.

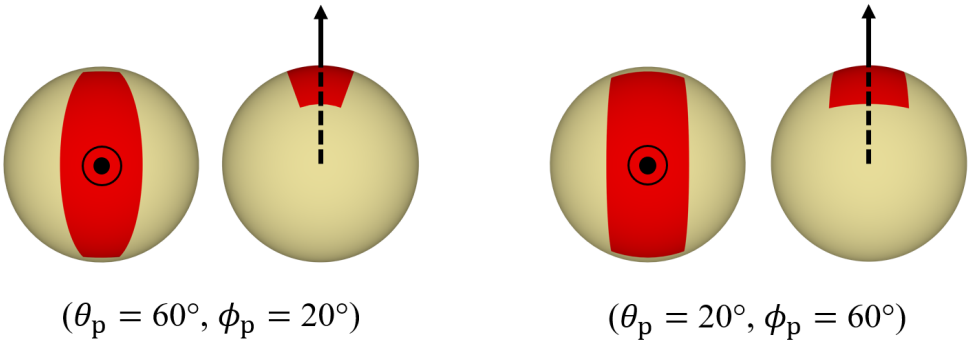


Figure 4.3: **Two distinct patch geometries corresponding to two pairs of half-opening angles where the values are swapped.** The surface coverage of patches corresponding to ($\theta_p = 60°$, $\phi_p = 20°$) and ($\theta_p = 20°$, $\phi_p = 60°$) is shaded in red.

The surface coverage of a patch defined in this manner, using the half-opening angles θ_p and ϕ_p, is given by:

$$A_{\text{patch}}/A_{\text{particle}} = \frac{\phi_p{}^\circ}{180°} \sin\theta_p \equiv \frac{\phi_p}{\pi} \sin\theta_p \tag{4.1}$$

where A_{patch} is the area of the patch, and A_{particle} is the total area of the spherical particle surface.

The potential makes use of three orthogonal unit vectors associated with each patch: $\hat{\boldsymbol{p}}_{\mathrm{p},1}$, $\hat{\boldsymbol{p}}_{\mathrm{p},2}$, and $\hat{\boldsymbol{p}}_{\mathrm{p},3}$. The unit vector $\hat{\boldsymbol{p}}_{\mathrm{p},1}$ is aligned with the vector from the centre of the particle to the centre of the patch ($\theta = 0°$, $\phi = 0°$); $\hat{\boldsymbol{p}}_{\mathrm{p},2}$ is aligned with the vector from the centre to the point ($\theta = 0°$, $\phi = 90°$); and $\hat{\boldsymbol{p}}_{\mathrm{p},3}$ is aligned with the vector from the centre to the pole of the patch ($\theta = 90°$). Note that at the poles all values of ϕ are equivalent, therefore it can be defined as simply $\theta = 90°$.

4.2.2.2 Defining two rectangular patches on the particle surface

Throughout this thesis, two-patch particles with one rectangular patch centred on each hemisphere are considered. The relative orientation of these patches is critical to their self-assembly behaviour, and can be defined *via* a skew angle χ.

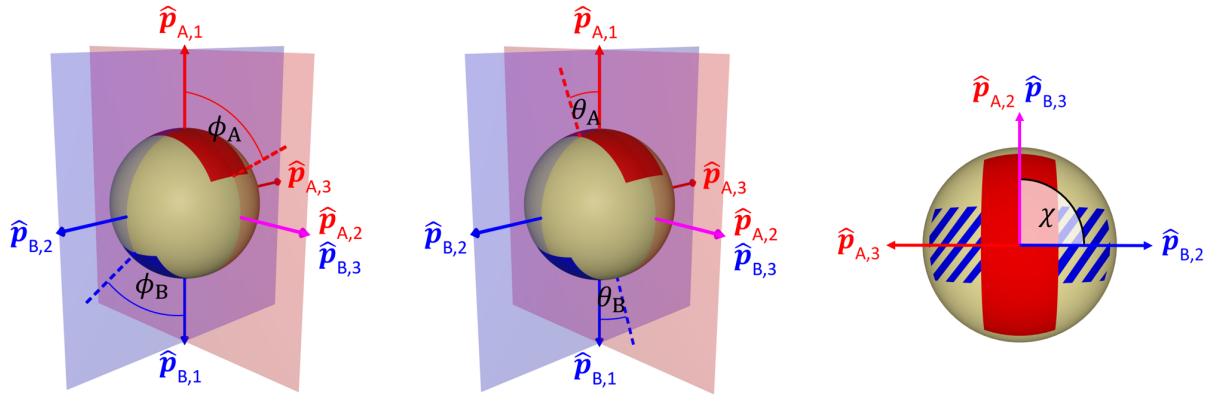


Figure 4.4: **Fully labelled schematics of a patchy particle with two rectangular patches.** The two patches, labelled A and B, are shown in red and blue respectively along with their pair of half-opening angles (θ_A, ϕ_A) and (θ_B, ϕ_B); their local coordinate frames; and the skew angle χ which defines the relative orientation of the patches. Here $\theta_A = \theta_B = 20°$, $\phi_A = \phi_B = 60°$ and $\chi = 90°$. In the right panel, the blue patch is dashed to indicate its location on the back face of the particle.

In order to obtain the patch vectors $\hat{\boldsymbol{p}}_{\mathrm{p}}$ for two-patch particles of a given skew angle χ, the coordinate frame of the first patch (A) given by $\hat{\boldsymbol{p}}_{\mathrm{A},1}$, $\hat{\boldsymbol{p}}_{\mathrm{A},2}$, and $\hat{\boldsymbol{p}}_{\mathrm{A},3}$ is used to define the coordinate frame of the second patch (B) such that:

$$\hat{\boldsymbol{p}}_{\mathrm{B},1} = -\hat{\boldsymbol{p}}_{\mathrm{A},1} \tag{4.2}$$

$$\hat{\boldsymbol{p}}_{\mathrm{B},2} = \boldsymbol{R}(\chi) \cdot \hat{\boldsymbol{p}}_{\mathrm{A},2} \tag{4.3}$$

$$\hat{\boldsymbol{p}}_{\mathrm{B},3} = \boldsymbol{R}(\chi) \cdot \hat{\boldsymbol{p}}_{\mathrm{A},3} \tag{4.4}$$

where $\boldsymbol{R}(\chi)$ is a rotation matrix describing a clockwise rotation by the angle χ about the axis $\hat{\boldsymbol{p}}_{\mathrm{A},1}$. Labelled schematics showing all six patch vectors along with the parameters defining the patch coverage (θ_{p}, ϕ_{p}) and orientation (χ) for an example two-patch particle are shown in Figure 4.4.

4.2.2.3 The modified angular component and its computation

For "rectangular" patches p and p′ on particles i and j respectively, the angular modulation factor $f_{\mathrm{pp}'}$ for the interaction between these patches is defined by:

$$f_{\mathrm{pp}'}(\boldsymbol{r}_{ij}, \hat{\boldsymbol{\Omega}}_i, \hat{\boldsymbol{\Omega}}_j) = \begin{cases} 1 \quad \text{if} \quad \begin{cases} & |\cos(\vartheta_{ij}^{\mathrm{p}})| < \cos(\vartheta_{\mathrm{p}}) \quad \text{(Criterion 1 on particle } i\text{)} \\ \text{and} & \cos(\phi_{ij}^{\mathrm{p}}) > \cos(\phi_{\mathrm{p}}) \quad \text{(Criterion 2 on particle } i\text{)} \\ \text{and} & |\cos(\vartheta_{ji}^{\mathrm{p}'})| < \cos(\vartheta_{\mathrm{p}'}) \quad \text{(Criterion 1 on particle } j\text{)} \\ \text{and} & \cos(\phi_{ji}^{\mathrm{p}'}) > \cos(\phi_{\mathrm{p}'}) \quad \text{(Criterion 2 on particle } j\text{)} \end{cases} \\ 0 \quad \text{otherwise} \end{cases} \tag{4.5}$$

where ϑ_{p} is the co-latitude of patch p;

$$\vartheta_{\mathrm{p}} = \pi/2 - \theta_{\mathrm{p}} \tag{4.6}$$

$\vartheta_{ij}^{\mathrm{p}}$ is the co-latitude of $\boldsymbol{r}_{ij}$ with respect to patch p (i.e., angle between $\boldsymbol{r}_{ij}$ and $\hat{\boldsymbol{p}}_{\mathrm{p},3}$);

$$\cos(\vartheta_{ij}^{\mathrm{p}}) = \hat{\boldsymbol{r}}_{ij} \cdot \hat{\boldsymbol{p}}_{\mathrm{p},3} \tag{4.7}$$

and ϕ_{ij}^{p} is the longitude of $\boldsymbol{r}_{ij}$ with respect to patch p (i.e., the angle between $\hat{\boldsymbol{p}}_{\mathrm{p},1}$ and the projection of $\boldsymbol{r}_{ij}$ into the ($\hat{\boldsymbol{p}}_{p,1}$, $\hat{\boldsymbol{p}}_{p,2}$) plane).

$$\cos(\phi_{ij}^{\mathrm{p}}) = \hat{\boldsymbol{r}}_{ij}^{\mathrm{p}_{1,2}} \cdot \hat{\boldsymbol{p}}_{\mathrm{p},1} \tag{4.8}$$

$$\text{where} \quad \boldsymbol{r}_{ij}^{\mathrm{p}_{1,2}} = \big(\hat{\boldsymbol{p}}_{\mathrm{p},1} \cdot \boldsymbol{r}_{ij}\big)\hat{\boldsymbol{p}}_{\mathrm{p},1} + \big(\hat{\boldsymbol{p}}_{\mathrm{p},2} \cdot \boldsymbol{r}_{ij}\big)\hat{\boldsymbol{p}}_{\mathrm{p},2} \tag{4.9}$$

$$\text{or equivalently} \quad \boldsymbol{r}_{ij}^{\mathrm{p}_{1,2}} = \boldsymbol{r}_{ij} - \big(\hat{\boldsymbol{p}}_{\mathrm{p},3} \cdot \boldsymbol{r}_{ij}\big)\hat{\boldsymbol{p}}_{\mathrm{p},3} \tag{4.10}$$

Similar expressions can be written in order to define $\vartheta_{ji}^{\mathrm{p}'}$ and $\phi_{ji}^{\mathrm{p}'}$.

In summary, this angular dependence simply determines if $\boldsymbol{r}_{ij}$ passes through patch surface on both particles – which is the orientational condition for bonding in Kern-Frenkel.

Within $f_{\mathrm{pp}\prime}$ each patch is subject to two criteria (as labelled in Equation 4.5). In terms of patch p on particle i, the first criterion checks if $\boldsymbol{r}_{ij}$ passes through the region on the surface of particle inscribed by the latitudinal lines given by the patch half-opening angle θ_{p}. The second criterion checks if $\boldsymbol{r}_{ij}$ passes through the region on the surface of particle inscribed by the longitudinal lines given by the patch half-opening angle ϕ_{p}. The parameters associated with each criterion for an example case are displayed in Figure 4.5. Figure 4.5**a** shows the first criterion, where the co-latitude of $\boldsymbol{r}_{ij}$ is given by Equation 4.7. Note the moduli in this first criteria take care of cases when $\vartheta_{ij}^{\mathrm{p}} > 90°$. Figure 4.5**b** shows the second criterion, where the configuration is shown with particle j in translucent yellow (left), and viewed along the pole of the patch $\hat{\boldsymbol{p}}_{p,3}$ (right) such that the ($\hat{\boldsymbol{p}}_{p,1}$, $\hat{\boldsymbol{p}}_{p,2}$) projection plane is within the page. Note the longitude of $\boldsymbol{r}_{ij}$ is given by Equation 4.8.

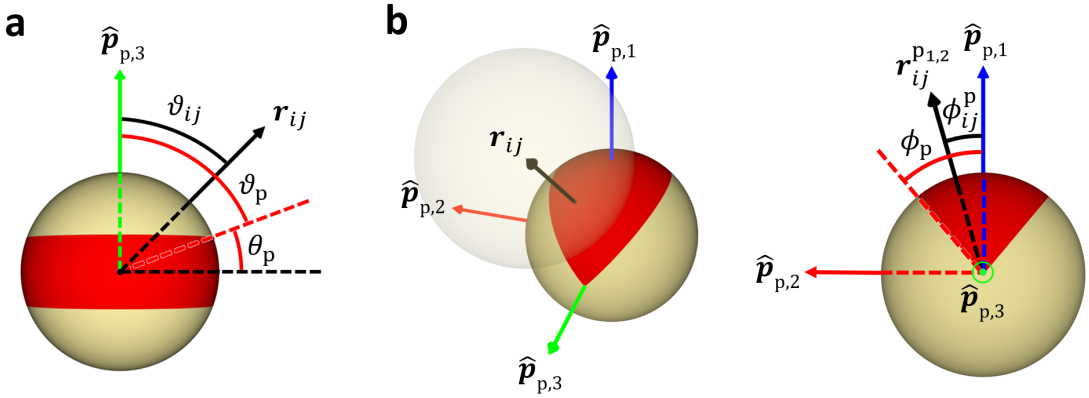


Figure 4.5: **Orientational criteria for rectangular patches.** Schematics of an example particle pair, where the variables and parameters appearing in the orientational criteria for rectangular patches are labelled. The separation vector $\mathbf{r}_{ij}$ must pass through patch surface on both particles in order for the patches to interact. (**a**) Example case of the first criterion where $\mathbf{r}_{ij}$ does not pass through the zone surface area shaded in red, which is defined by θ_{p}. (**b**) Example case of the second criterion where $\mathbf{r}_{ij}$ passes through the lune surface area shaded in red, which is defined by ϕ_{p}. (left) The particle j considered for interaction, which defines $\mathbf{r}_{ij}$, is shown in translucent yellow to help visualise how the particles are positioned. (right) Viewed along the pole of the patch $\hat{\boldsymbol{p}}_{p,3}$, so that the ($\hat{\boldsymbol{p}}_{p,1}$, $\hat{\boldsymbol{p}}_{p,2}$) projection plane is within the page itself, showing how this projection is used to extract ϕ_{ij}^{p}.

4.2.2.4 Extending this model to more complex patch geometries

As mentioned above, the non-circular patches considered in this thesis are obtained *via* the overlap of a lune and a zone on the surface of a sphere. Under this scheme, for a patch p, zone orientations are defined by a single vector ($\hat{\boldsymbol{p}}_{\mathrm{p},3}$) and lune orientations are defined by two vectors ($\hat{\boldsymbol{p}}_{\mathrm{p},1}$ and $\hat{\boldsymbol{p}}_{\mathrm{p},2}$). Together these orthogonal vectors give the patch frame, but they need not be orthogonal and individual vectors can be altered to give different patch geometries. Various numbers and combinations of patch components can also be used in combination with different set operators ($\cup$, $\cap$, etc.) to give rise to complex patch coverages.

4.2.3 Parametrisation of particles with two rectangular patches

Throughout this thesis (unless stated otherwise) particles with two rectangular patches are defined as shown in Figure 4.6 *via* the patch half-opening angles θ_p and ϕ_p which define the patch geometries (where both patches are identical), and the skew angle χ which gives the relative orientation of these patches.

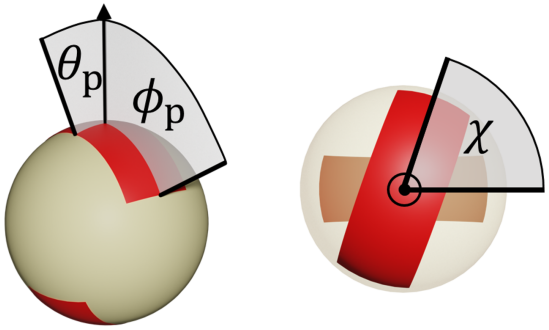


Figure 4.6: **Parametrisation of particles with two rectangular patches.** Patch geometries are defined by the half-opening angles θ_p and ϕ_p (where both patches are identical), and their relative orientation is defined *via* the skew angle χ.

4.2.4 Self-assembly of particles with two rectangular patches at various skew angles (χ)

Section 4.2.1 proposes that particles with two trimer-forming rectangular patches can selectively form corner-shared trimer structures with controlled inter-trimer dihedral angles. The use of these particles as parametrised in Section 4.2.3 means that the skew angle of the patches χ directly translates to the inter-trimer dihedral angle that is selectively formed.

To investigate this dihedral angle restriction and the self-assembly behaviour of these particles, a series of Monte Carlo simulations in the NVT ensemble were performed using

patchy particles with two rectangular patches over the entire range of skew angles $\chi = [0^\circ$ to $178^\circ]$ (with a resolution of 2°). Note that $\chi = 0^\circ \equiv 180^\circ$. In these simulations systems of $N = 768$ particles were considered with patch coverage parameters appropriate for the formation of trigonal units ($\theta_\mathrm{p} = 10^\circ$, $\phi_\mathrm{p} = 44^\circ$) at a density of $\rho^* = 0.3$, and were subjected to a one-step quench from $T^* = 1$.

Measuring the inter-trimer dihedral angle distributions of fluid configurations confirms that dihedral angle selection is indeed observed, where dihedrals are limited to a small range around the skew angle χ of the particles under consideration – despite the lack of long range order. It is worth noting that these systems, where the dihedral angle control essentially results in the selective formation of a single specific angle, ring control is also achieved since the corner-shared trigonal networks are forced to form a specific arrangement. It is therefore useful to calculate the ring distributions for systems in which the formation of long range order is observed.

The final ring distributions for systems dropped to a temperature of $T^* = 0.11$ are plotted in Figure 4.7**a** as a function of particle skew angle χ, and they reveal five distinct structural regions (eight if enantiomorphic regions are considered to be unique). The different regions are labelled and highlighted in Figure 4.7**b** on a χ number line, and these various structures formed are explored in following subsections. Note the self-assembly of crystals formed from $\chi = [66^\circ$ to $76^\circ]$ and $[104^\circ$ to $114^\circ]$ is explored in Chapter 5.

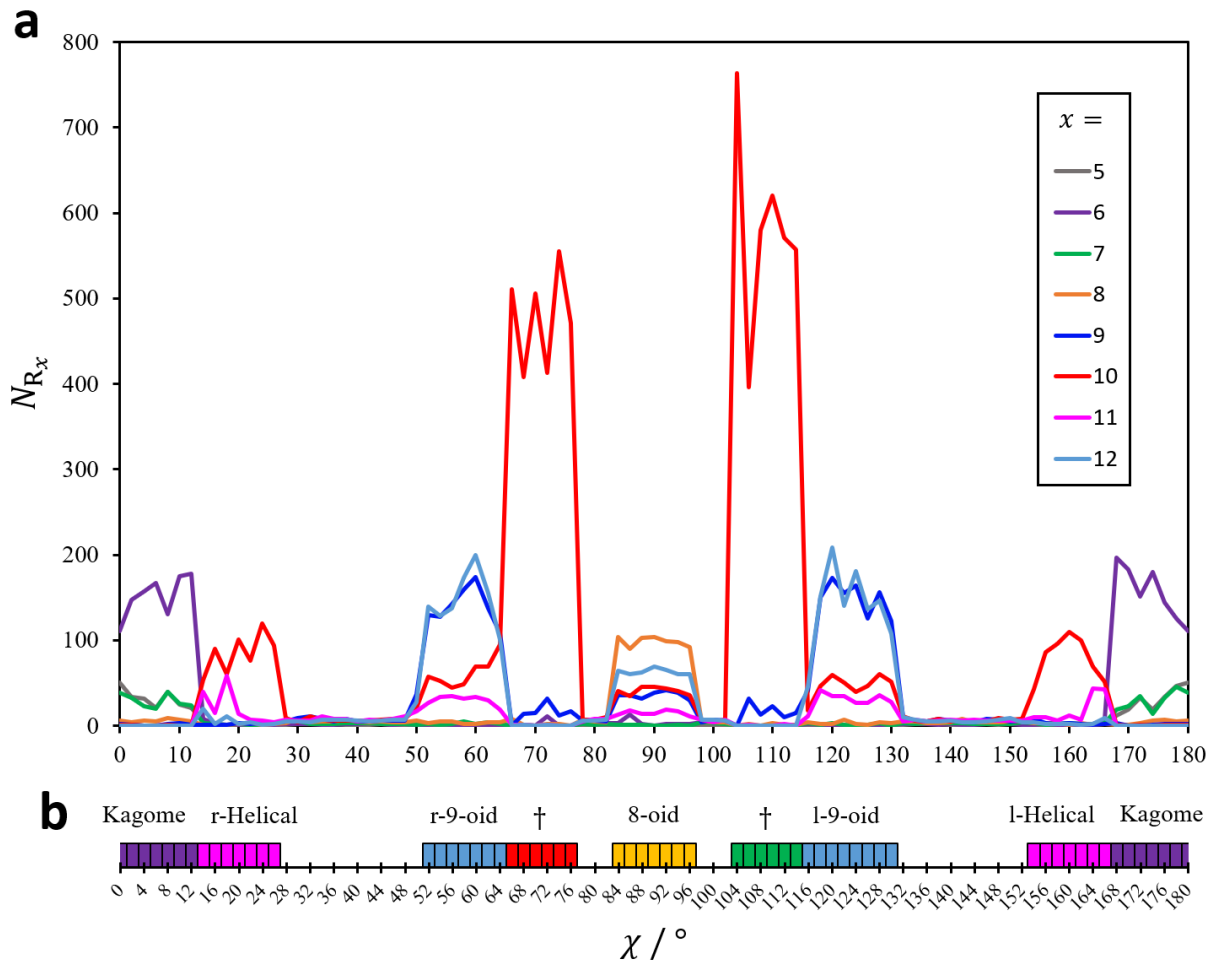


Figure 4.7: **Structures self-assembled from particles with two rectangular patches at various skew angles (χ).** (**a**) Final ring counts N_{R_x} (where x is the ring size) as a function of skew angle χ for systems of $N = 768$ particles with two rectangular patches ($\theta_{\mathrm{p}} = 10°$, $\phi_{\mathrm{p}} = 44°$) at a density of $\rho^* = 0.3$, after 100 million MC cycles following a one-step quench from $T^* = 1$ to $T^* = 0.11$ (note final ring counts were averaged over the last 1 million MC cycles). (**b**) Structural regions within **a** highlighted and labelled on a χ number line. † Right and left handed gyroid crystals formed from $\chi = [66°$ to $76°]$ and $[104°$ to $114°]$ are covered in Chapter 5.

4.2.4.1 Kagome

Stacked kagome sheets are observed up to 12° from $\chi = 0°$ (in either direction) which is demonstrated by the final ring distributions displayed in Figure 4.8**a**, which clearly show the dominance of 6-membered rings with 5- and 7-membered rings being the major source of defects. Figure 4.8**b** shows particles corresponding to $\chi = 12°$, which is on the edge of the kagome region, where the core is translucent to show the skew angle. Figure 4.8**c** shows a typical 6-membered ring within the $\chi = 12°$ system, and Figure 4.8**d** shows a snapshot of the entire final configuration.

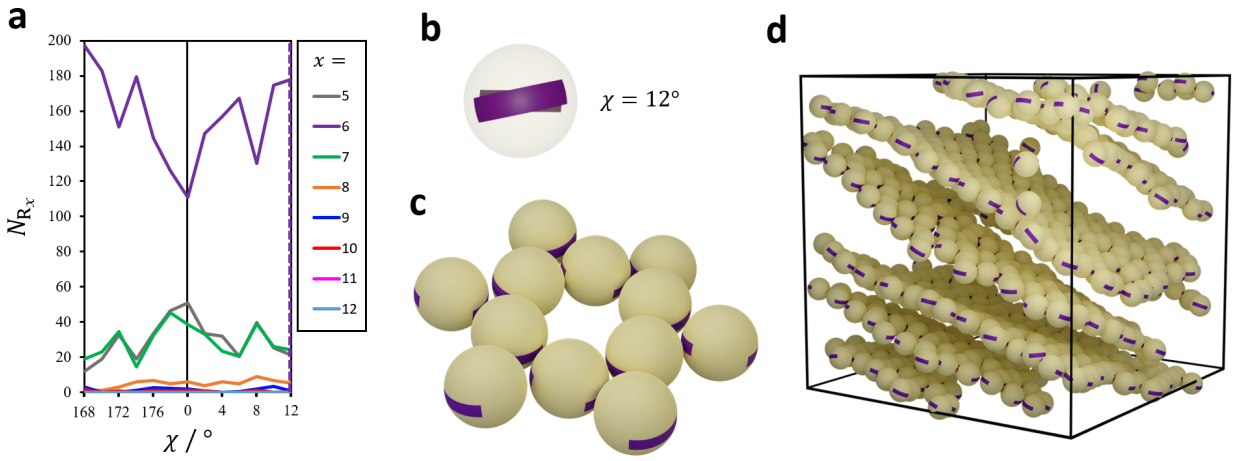


Figure 4.8: **Kagome region of skew angle space for particles with two trimer-forming rectangular patches.** (**a**) Final ring counts N_{R_x} (where x is the ring size) as a function of skew angle χ for systems of $N = 768$ particles with two rectangular patches ($\theta_p = 10°$, $\phi_p = 44°$) at a density of $\rho^* = 0.3$, after 100 million MC cycles following a one-step quench from $T^* = 1$ to $T^* = 0.11$ (note final ring counts were averaged over the last 1 million MC cycles). (**b-d**) Visualisation of the kagome structure for the $\chi = 12°$ system where: **b** shows the particles under consideration with a translucent core to show the skew angle; **c** shows the 6-membered ring kagome substructure; and **d** shows a snapshot of the final configuration.

The ring distributions in Figure 4.8**a** display a trend where 6-membered ring counts decrease closer to $\chi = 0°$, whereas 5- and 7-membered ring defects increase. This suggests that within the kagome region, systems further from the ideal skew angle ($\chi = 0°$) generally display less defects. To investigate this, systems were considered at various quenching temperatures and the final ring distributions for $T^* = 0.1175$, 0.115, 0.1125, and the already considered $T^* = 0.11$ are displayed in Figure 4.9. The distributions show that increasing temperature narrows the χ window for kagome assembly, revealing that the transition temperature for kagome is skew angle dependent. This explains the trend of increased defects nearer $\chi = 0°$ at a given temperature, since these systems are more under-cooled and hence result in increased 5- and 7-membered ring kinetic traps.

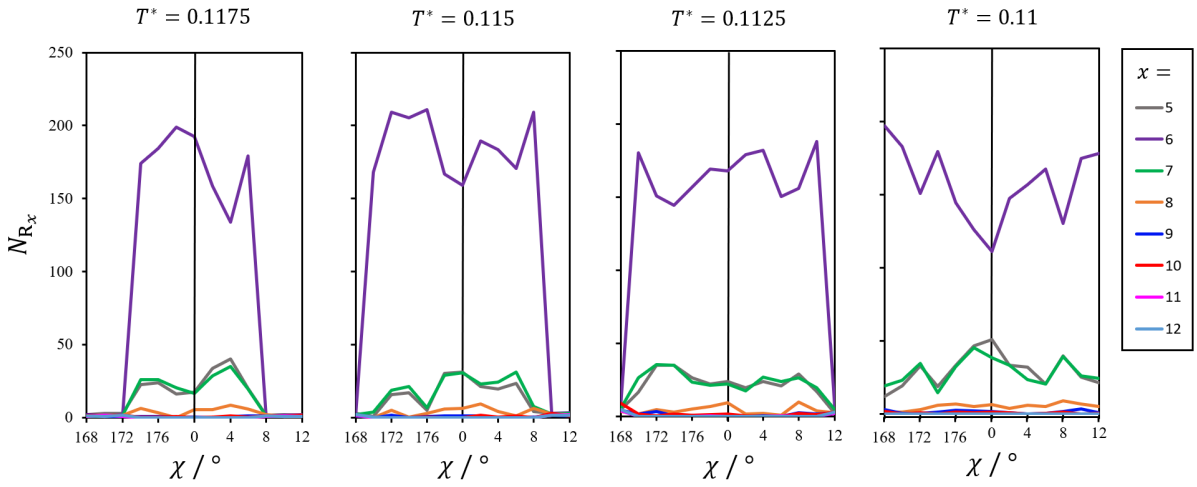


Figure 4.9: **Ring distributions at various temperatures for the kagome region of skew angle space.** Final ring counts N_{R_x} (where x is the ring size) as a function of skew angle χ for systems of $N = 768$ particles with two rectangular patches ($\theta_{\mathrm{p}} = 10°$, $\phi_{\mathrm{p}} = 44°$) at a density of $\rho^* = 0.3$, after 100 million MC cycles following a one-step quench from $T^* = 1$ to a range of temperatures, as labelled. Note final ring counts were averaged over the last 1 million MC cycles.

4.2.4.2 Helical

Just past the kagome skew angle limit of $\chi \approx 12°$, inter-trimer dihedral angles are restricted such that the formation of planes is no longer geometrically allowed, as such the would-be 6-membered kagome rings cannot close and instead form infinite helical corner-shared trimer substructures. These "helical" structures are observed in two enantiomorphic regions from $\chi = [14°$ to $26°]$ and $[154°$ to $166°]$, and the final ring distributions for these regions are displayed in Figure 4.10**a**. Figure 4.10**b** shows particles just past the kagome regime, corresponding to $\chi = 14°$, where the core is translucent to show the skew angle. Figure 4.10**c**

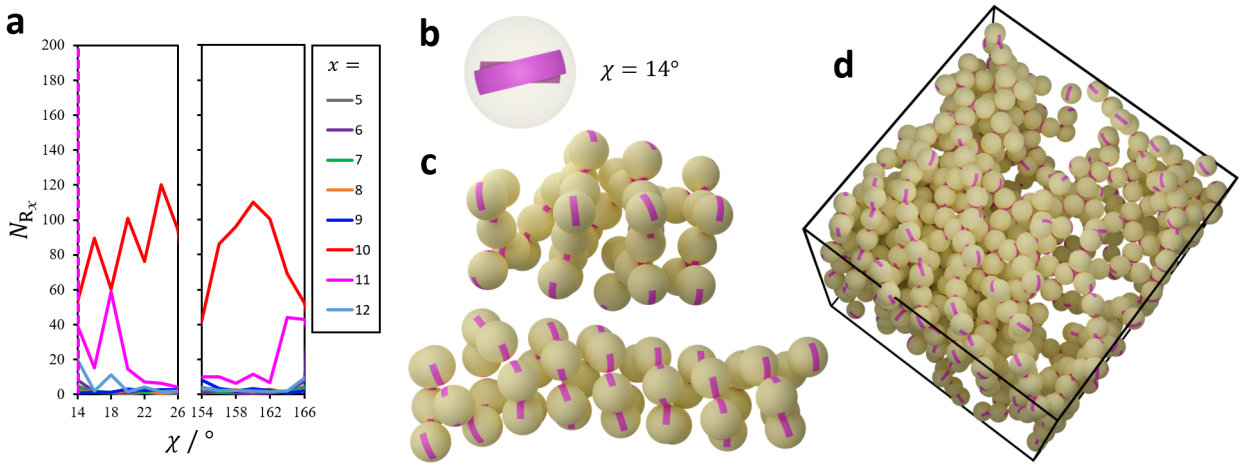


Figure 4.10: **Helical regions of skew angle space for particles with two trimer-forming rectangular patches.** (**a**) Final ring counts N_{R_x} (where x is the ring size) as a function of skew angle χ for systems of $N = 768$ particles with two rectangular patches ($\theta_p = 10°$, $\phi_p = 44°$) at a density of $\rho^* = 0.3$, after 100 million MC cycles following a one-step quench from $T^* = 1$ to $T^* = 0.11$ (note final ring counts were averaged over the last 1 million MC cycles). (**b-d**) Visualisation of the Helical structure for the $\chi = 14°$ system where: **b** shows the particles under consideration with a translucent core to show the skew angle; **c** shows representative helical substructures both with (top) and without (bottom) the trimer capping particles; and **d** shows a snapshot of the final configuration.

shows typical helical substructures within the $\chi = 12°$ system both with (top) and without (bottom) the trimer capping particles, and Figure 4.10**d** shows a snapshot of the entire final configuration.

The helical substructure is stabilised, and interconnected, *via* 10-membered rings and also 11-membered rings to a lesser extent at shallower skew angles. As the skew angle of the particles increases, the geometry of the helices changes, and eventually they are no longer observed since the inter-trimer dihedral angles under consideration do not geometrically allow for the formation of stabilising rings.

4.2.4.3 9-oid

The 9-oid regions – named after their dominant ring size – occur in two enantiomorphic windows from $\chi = [52°$ to $64°]$ and $[116°$ to $130°]$, and the final ring distributions for these regions are displayed in Figure 4.11**a**. These distributions clearly show the dominance of 9- and 12-membered rings, with 10- and 11-membered rings being the major source of defects. Figure 4.11**b** shows particles corresponding to $\chi = 60°$, where the core is translucent to show the skew angle. Figure 4.11**c** shows the characteristic fused 9- and 12-membered ring substructure within the $\chi = 60°$ system, and Figure 4.11**d** shows a snapshot of the entire final configuration.

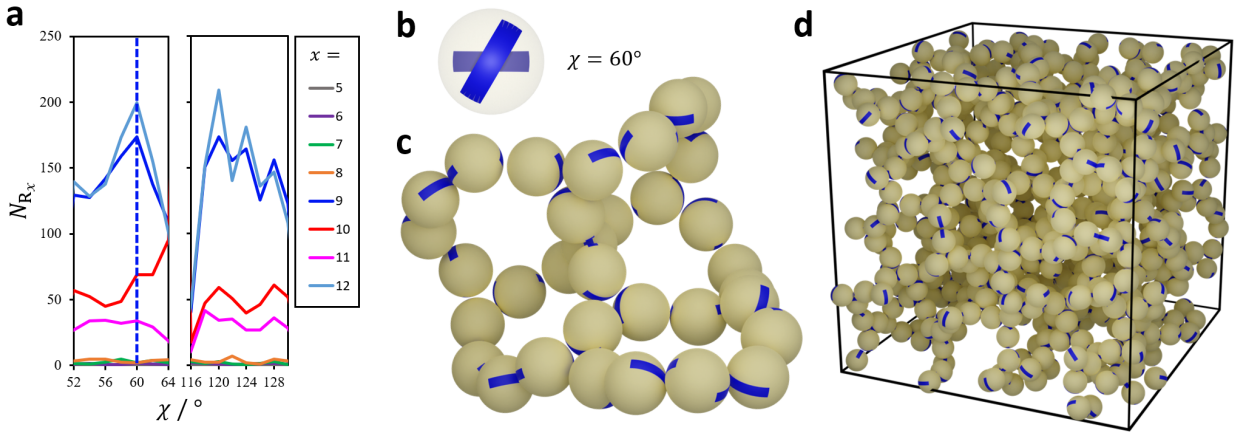


Figure 4.11: **9-oid regions of skew angle space for particles with two trimer-forming rectangular patches.** (**a**) Final ring counts N_{R_x} (where x is the ring size) as a function of skew angle χ for systems of $N = 768$ particles with two rectangular patches ($\theta_{\mathrm{p}} = 10°$, $\phi_{\mathrm{p}} = 44°$) at a density of $\rho^* = 0.3$, after 100 million MC cycles following a one-step quench from $T^* = 1$ to $T^* = 0.11$ (note final ring counts were averaged over the last 1 million MC cycles). (**b-d**) Visualisation of the 9-oid structure for the $\chi = 60°$ system where: **b** shows the particles under consideration with a translucent core to show the skew angle; **c** shows the fused 9-membered ring substructure (without the trimer capping particles for clarity); and **d** shows a snapshot of the final configuration.

4.2.4.4 8-oid

The 8-oid region – named after its dominant ring size – occurs from $\chi = [84°$ to $96°]$, and the final ring distributions for this region are displayed in Figure 4.12**a**. These distributions clearly show the dominance of 8-membered rings, with 12-, 9-, 10-, and 11-membered rings being minor components. Figure 4.12**b** shows particles corresponding to $\chi = 90°$, where the core is translucent to show the skew angle. Figure 4.12**c** shows the characteristic 8-membered ring substructure within the $\chi = 90°$ system, and Figure 4.12**d** shows a snapshot of the entire final configuration.

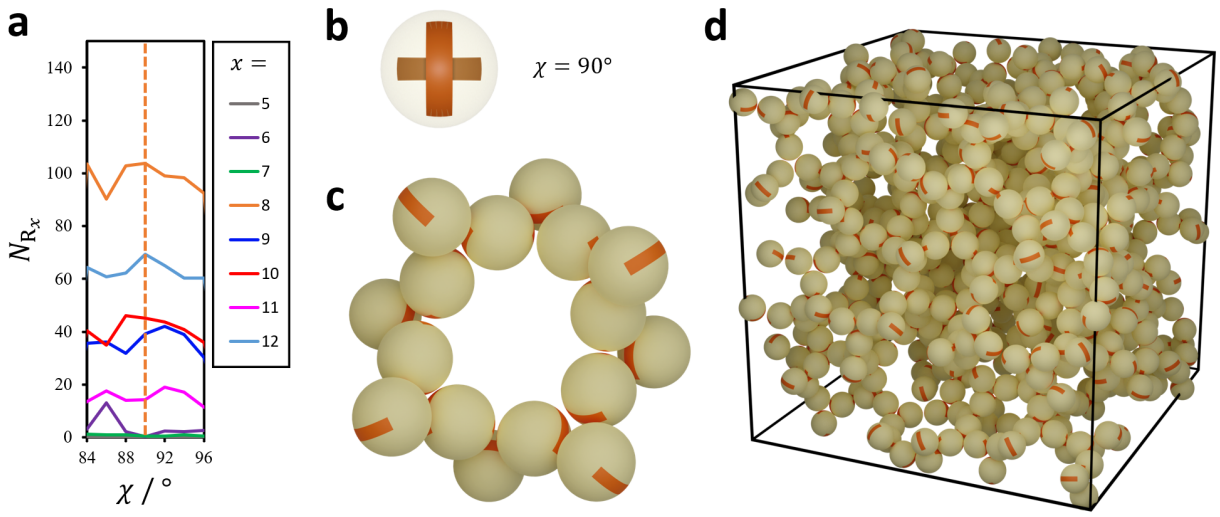


Figure 4.12: **8-oid region of skew angle space for particles with two trimer-forming rectangular patches.** (**a**) Final ring counts N_{R_x} (where x is the ring size) as a function of skew angle χ for systems of $N = 768$ particles with two rectangular patches ($\theta_{\mathrm{p}} = 10°$, $\phi_{\mathrm{p}} = 44°$) at a density of $\rho^* = 0.3$, after 100 million MC cycles following a one-step quench from $T^* = 1$ to $T^* = 0.11$ (note final ring counts were averaged over the last 1 million MC cycles). (**b-d**) Visualisation of the 8-oid structure for the $\chi = 90°$ system where: **b** shows the particles under consideration with a translucent core to show the skew angle; **c** shows the predominant 8-membered ring substructure; and **d** shows a snapshot of the final configuration.

4.3 Conclusions

In an attempt to obtain a self-assembly route to the single colloidal gyroid crystal proposed in Chapter 3, this chapter proposes that the use of particles with two trimer-forming rectangular patches oriented at well-defined skew angles can give rise to inter-trimer dihedral angle selection. The competing structures outlined in Chapter 3 can be distinguished *via* their inter-trimer dihedral angles, and therefore this proposed dihedral angle control could offer a method of structure selection.

A pair potential for rectangular patches based upon the principles of the widely used Kern-Frenkel model for circular patches [104] is then presented. This potential can easily be further modified to study various non-circular patches, and investigate their self-assembly both in line with and in an attempt to motivate synthetic advances. The proposed method of dihedral angle selection herein is then validated using this developed pair potential to study the self-assembly behaviour of particles with two trimer-forming rectangular patches at various skew angles. These particles are shown to form a range of chiral and achiral structures which are stabilised at different patch skew angles.

Chapter Five

Self-Assembly Routes to Single Colloidal Gyroid

5.1 Introduction

The self-assembly of a single gyroid structure poses a significant challenge. Despite the fact that double gyroid self-assembly is common in systems with elements of frustration, such as surfactants, block copolymers, and mesogens [90, 98–100], direct self-assembly of a single gyroid structure remains elusive [95–97]. The targeted self-assembly of a single gyroid from colloidal building blocks is a highly attractive prospect with regards to the fabrication of 3D photonic crystals, which operate in the visible region [30] – for which there is currently no efficient fabrication means [92]. Such structures have a range of potential applications for example in light-harvesting technology [31], energy storage [32], sensing [33], and optical circuits [34, 35], with the chirality of single gyroid in particular also offering additional applications over achiral alternatives such as diamond [92–94].

In Chapter 3 discretised single gyroid crystals are proposed along with potential building blocks which stabilise said crystals, but the systems investigated are found to be insuf-

ficient to self-assemble single gyroid. In Chapter 4 it is established that the use of particles with non-circular patches can selectively form structures with predetermined dihedral angles, *via* control of their relative patch orientation, thus offering a form of structure selection.

This chapter uses Monte Carlo simulations in combination with the potential detailed in Chapter 4, and standard Kern-Frenkel [104], to investigate the self-assembly of single colloidal gyroid from particles with synthetically reasonable patches. Further studies are then performed in order to establish the parameter space appropriate for crystallisation and the tolerance for polydispersity – which is inevitable in experimental systems. A significant parameter space window for crystallisation which is also robust to various types of polydispersity is key to reasonably envision experimental self-assembly.

5.2 Results and discussion

5.2.1 Self-assembly of colloidal gyroid using two rectangular patches

To determine if the particles with rectangular patches proposed in Chapter 4 can achieve appropriate inter-trimer dihedral angle restriction resulting in the selective formation of an enantiomorphic single gyroid crystal, Monte Carlo simulations in the NVT ensemble were performed using patchy particles with two staggered rectangular patches at the ideal gyroid dihedral angle ($\chi = 70.5°$). In these simulations systems of $N = 1500$ particles were considered over a range of patch geometries at the approximate colloidal gyroid density of $\rho^* = 0.3$, and were subjected to a one-step quench from $T^* = 1$. Enantiomorphic crystallisation of colloidal gyroid is indeed observed, with Figure 5.1 showing data for a system with patch half-opening angles of $\theta_\mathrm{p} = 10°$ and $\phi_\mathrm{p} = 44°$. Figure 5.1**a** (top) shows the evolution of the number of trigonal planar clusters N_trig, and the potential energy per particle U^*/N,

after the temperature is dropped to $T^* = 0.11$. The sharp drop in energy and corresponding growth in the number of trigonal units, suggested the occurrence of a phase transition, and the final ring distribution showed practically all 10-membered rings, confirming that a gyroid crystal had formed. The 10-membered ring count $N_{\mathrm{R}_{10}}$ and global Steinhardt bond-order parameter Q_4 are effective order parameters for the transition and their evolution is shown in Figure 5.1**a** (bottom), capturing the growth of crystalline order.

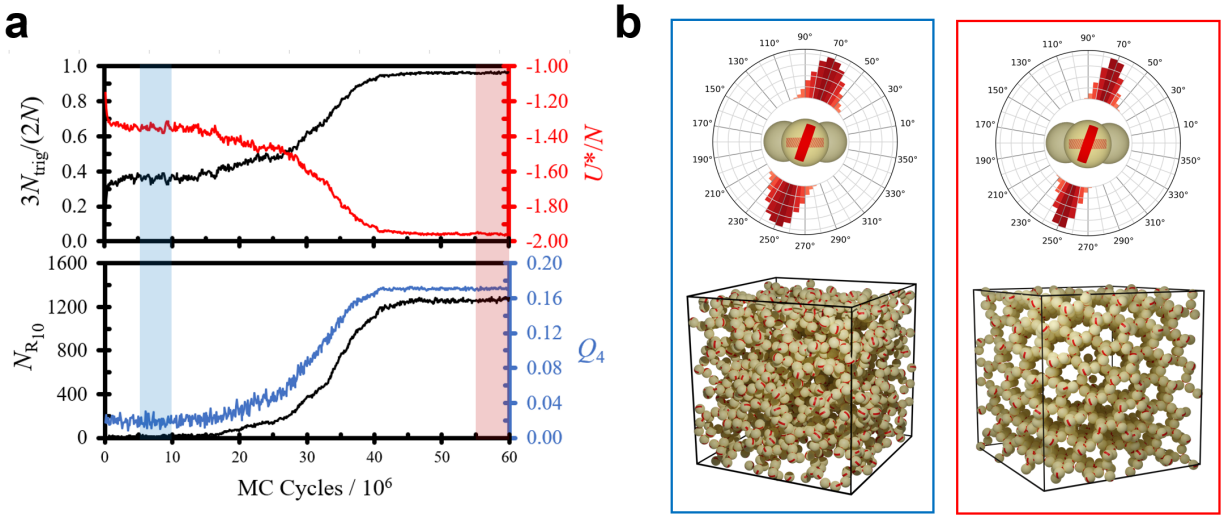


Figure 5.1: **Self-assembly of single colloidal gyroid from particles with two staggered rectangular patches.** (**a**) Evolution of the number of trigonal planar clusters N_{trig} (black line), the potential energy per particle U^*/N (red line), the number of 10-membered rings $N_{\mathrm{R}_{10}}$ (black line), and the global Steinhardt bond-order parameter Q_4 (blue line) for a system of $N = 1500$ patchy particles with two equal-size staggered rectangular patches with half-opening angles $\theta_{\mathrm{p}} = 10°$, $\phi_{\mathrm{p}} = 44°$ and skew parameter $\chi = 70.5°$, at a density of $\rho^* = 0.3$, following one-step quenching from a temperature of $T^* = 1$ to $T^* = 0.11$. (**b**) Polar histograms (top) of the inter-trimer dihedral angles over two intervals of 5 million MC cycles at the pre- and post-nucleation stages (as indicated by the blue and red borders and corresponding shading in **a**), and representative configurations (bottom) within the two intervals.

In order to probe the evolution of local order within the system, the inter-trimer dihedral angle distribution was calculated at various intervals throughout the simulation, and the results of this are shown as polar histograms in Figure 5.1**b** (top). The dihedral angle distributions are taken over intervals of 5 million MC cycles at pre- and post-nucleation stages (as indicated by blue and red borders respectively, and corresponding shaded regions in Figure 5.1**a**). The pre-nucleation distribution (left) shows that despite the lack of any long range order, the dihedral angles are restricted to a small range around the skew angle of the patches ($\chi = 70.5°$) – this demonstrates the design principles in action and is in stark contrast to what is observed in the case of circular patches (Chapter 3 Section 3.2.4). The distribution then becomes narrower around the ideal gyroid angle post-nucleation (right), as the size of fluctuations become limited by the crystalline structure. Figure 5.1**b** also shows corresponding representative fluid and crystalline configurations (bottom).

5.2.1.1 Rectangular patch parameter space for crystallisation

To investigate the range of size and geometry of rectangular patches over which the crystallisation of single colloidal gyroid is observed, a series of Monte Carlo simulations were performed using various combinations of patch half-opening angles θ_p and ϕ_p. Systems of $N = 768$ patchy particles with two staggered rectangular patches at the ideal gyroid skew angle ($\chi = 70.5°$ or $109.5°$) at a density of $\rho^* = 0.3$, were subjected to one-step quenching from $T^* = 1$. Figure 5.2 shows these results in (θ_p, ϕ_p) space where green filled points indicate crystallisation within 100 million MC cycles, as identified *via* a final global Steinhardt bond-order parameter value of $Q_4 > 0.1$ (averaged over the final 1 million MC cycles). This data clearly shows that systems of colloidal patchy spheres with rectangular patches have a significant range of (θ_p, ϕ_p) space over which crystallisation of single colloidal gyroid is observed.

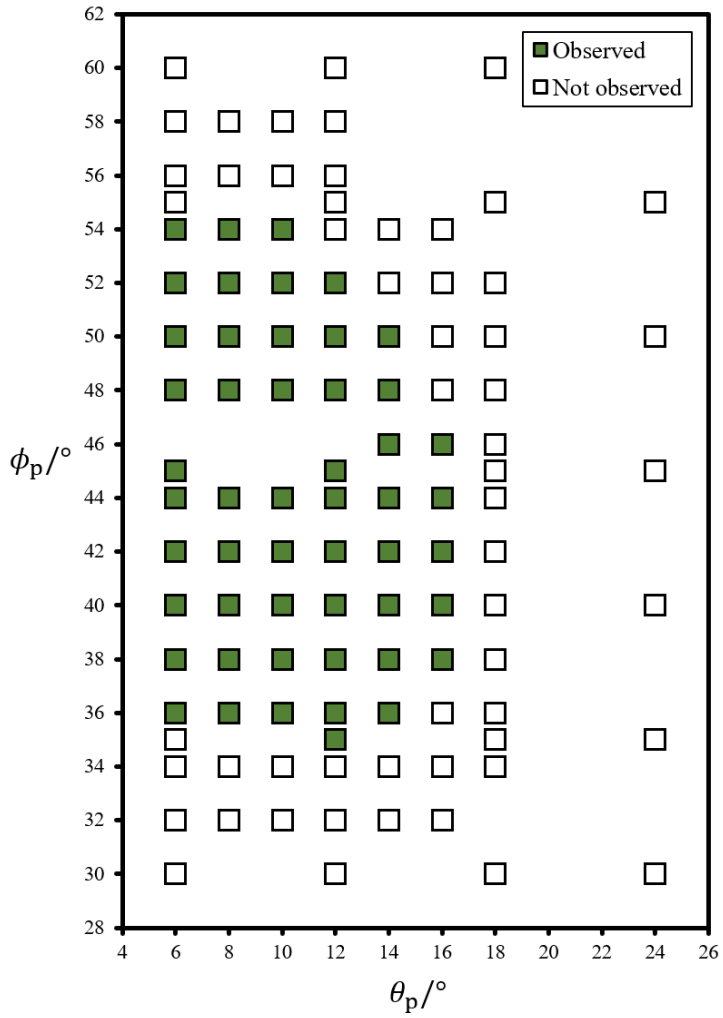


Figure 5.2: **Robustness of rectangular patch coverage space for crystallising single colloidal gyroid.** Green filled points indicate crystallisation within 100 million MC cycles following a one-step quench from $T^* = 1$, for various systems of $N = 768$ particles with staggered rectangular patches at the ideal gyroid skew angle ($\chi = 70.5°$ or $109.5°$) at a density of $\rho^* = 0.3$, as identified *via* a final global Steinhardt bond-order parameter value of $Q_4 > 0.1$ (averaged over the final 1 million MC cycles).

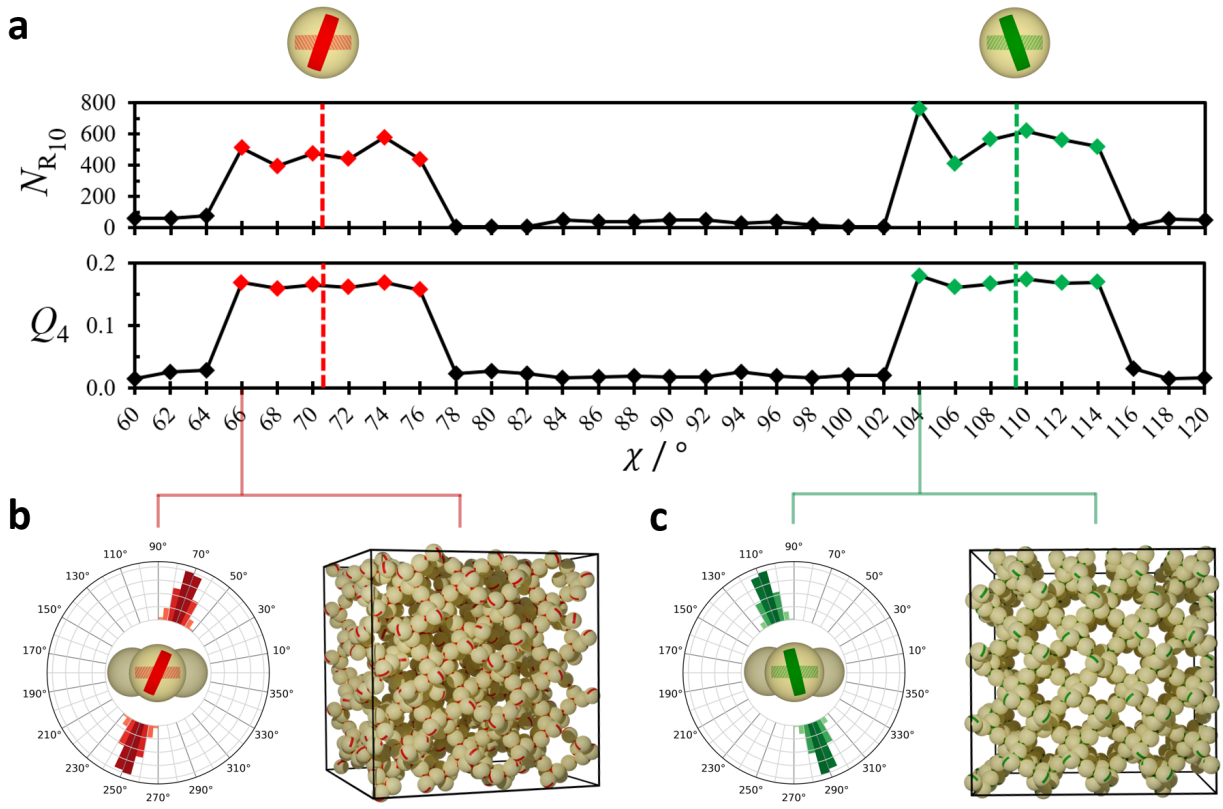


Figure 5.3: **Robustness of skew angle space for crystallising single colloidal gyroid structures.** (**a**) Final 10-membered ring counts $N_{R_{10}}$, and global Steinhardt bond-order parameter Q_4 values, as a function of skew angle χ, for systems of $N = 768$ particles with two rectangular patches ($\theta_p = 10°$, $\phi_p = 44°$) at a density of $\rho^* = 0.3$, after the temperature is dropped from $T^* = 1$ to $T^* = 0.11$. Red and green dashed lines indicate the ideal χ values for right and left-handed gyroid respectively, and red and green points indicate corresponding crystalline configurations (as identified *via* a value of $Q_4 > 0.1$). (**b-c**) Inter-trimer dihedral angle distributions (taken over the last 10 million MC cycles), and final configurations for the $\chi = 66°$ **b**, and $\chi = 104°$ **c** systems, as labelled.

A similar investigation was carried out to determine the robustness of single colloidal gyroid crystallisation with respect to the skew angle χ. As such, a series of Monte Carlo simulations were performed using systems of $N = 768$ particles at a density of $\rho^* = 0.3$ with fixed patch half-opening angles of $\theta_{\mathrm{p}} = 10^\circ$ and $\phi_{\mathrm{p}} = 44^\circ$, but with various skew angles from $\chi = [60^\circ$ to $120^\circ]$ (with a resolution of 2°). Figure 5.3**a** shows the final 10-membered ring counts $N_{\mathrm{R}_{10}}$, and global Steinhardt bond-order parameter Q_4 values, for each system after equilibration upon quenching from $T^* = 1$ to $T^* = 0.11$. The plots clearly show the two enantiomorphic regions, which yield colloidal gyroid from $\chi = [66^\circ$ to $76^\circ]$ and $[104^\circ$ to $114^\circ]$. Figure 5.3**b** and Figure 5.3**c** show the inter-trimer dihedral angle distributions, and final configurations for the $\chi = 66^\circ$ and $\chi = 104^\circ$ systems respectively. It is worth noting that the distributions peak at the ideal gyroid angles and not at the χ values under consideration, which indicates that particles possessing non-ideal χ values which form gyroid do not distort the resulting crystal.

5.2.1.2 Effects of number density on crystallisation

So far, Monte Carlo simulations have been performed in the NVT ensemble at the approximate colloidal gyroid density of $\rho^* = 0.3$. In order to investigate the effects of density on crystallization, sets of one-step quenches were also carried out over a range of densities. As such, systems of $N = 768$ particles with two staggered rectangular patches at the ideal gyroid skew angle ($\chi = 70.5^\circ$), at various number densities (ρ^*), with patch half-opening angles of $\theta_{\mathrm{p}} = 10^\circ$ and $\phi_{\mathrm{p}} = 44^\circ$ were subjected to one-step quenching from $T^* = 1$. Figure 5.4 shows the final global Steinhardt bond-order parameter Q_4 values, for each system as a function of the reduced number density ρ^*. It is evident that the crystallization of single colloidal gyroid is observed over a wide range of densities up to the maximum considered here ($\rho^* = 0.35$), which is slightly above the maximum single colloidal gyroid density ($\rho^* \approx 0.34$) corresponding to touching spheres in the perfect crystal. The final configurations corresponding to

$\rho^* = 0.1$ and $\rho^* = 0.35$ are also shown above. Note that the system above the touching spheres density ($\rho^* = 0.35$) results in the self-assembly of a lower quality crystal, as evident from its lower Q_4 value, which is intuitive since a perfect crystal cannot physically fit into a simulation cell at this density.

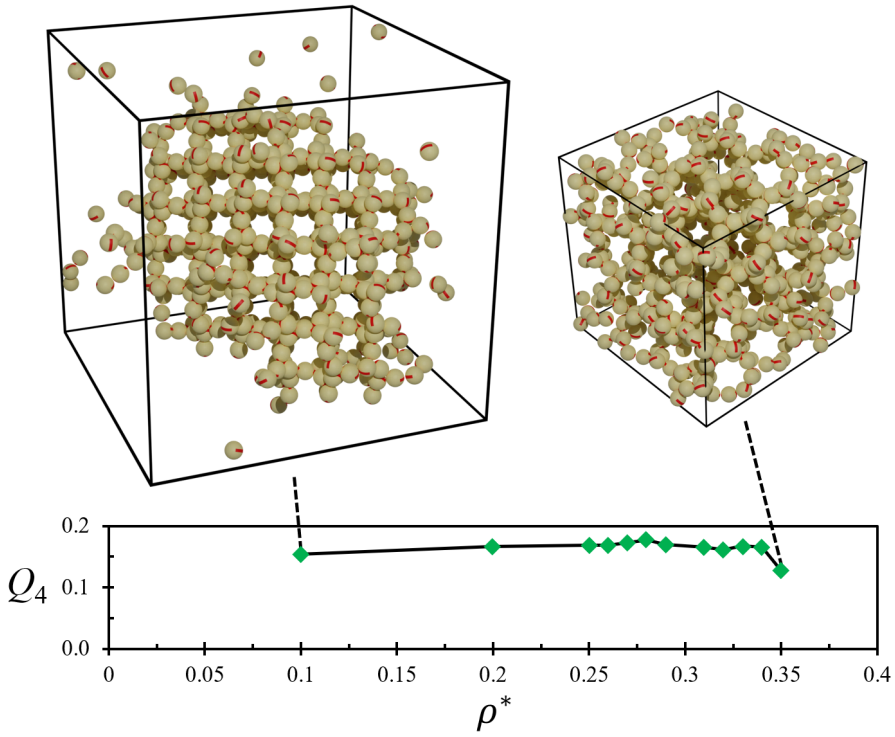


Figure 5.4: **Single colloidal gyroid crystallization at various number densities.** Final global Steinhardt bond-order parameter Q_4 values, as a function of reduced number density ρ^*, for systems of $N = 768$ particles with two rectangular patches ($\theta_p = 10°$, $\phi_p = 44°$) at a skew angle of $\chi = 70.5°$. Systems were subject to 100 million Monte Carlo cycles following a one-step quench from $T^* = 1$ and the global Steinhardt bond-order parameter values were evaluated by averaging over the final 1 million Monte Carlo cycles. Green points indicate crystalline configurations (as identified *via* a value of $Q_4 > 0.1$). Snapshots of the final configurations for the $\rho^* = 0.1$ and $\rho^* = 0.35$ systems (as labelled) are shown above.

5.2.1.3 Polydispersity in rectangular patch coverage

To investigate how robust single gyroid crystallisation is with regards to dispersity in patch coverage and/or orientation – which is inevitable in experimental systems – sets of Monte Carlo simulations were carried out with polydisperse patch parameters. Firstly, sets of "target" rectangular patch parameters for each system where chosen. Target values for θ_{p} and ϕ_{p} were chosen in the context of results from the monodisperse patch-coverage space study (Section 5.2.1.1), to give "ideal" values of $\theta_{\mathrm{p}} = 10°$ and $\phi_{\mathrm{p}} = 44°$ (corresponding to an approximate central point in Figure 5.2). These values along with the ideal χ for gyroid were used as population mean values ($\mu_{\theta_{\mathrm{p}}} = 10°$, $\mu_{\phi_{\mathrm{p}}} = 44°$, and $\mu_{\chi} = 70.5°$) from which different degrees of dispersity were obtained by pulling from normal distributions centred around these means with varying standard deviations ($\sigma_{\theta_{\mathrm{p}}}$, $\sigma_{\phi_{\mathrm{p}}}$, and σ_{χ}).

In the following studies, systems of $N = 768$ particles were considered at a density of $\rho^* = 0.3$ following a one-step quench from $T^* = 1$, where each patch is distinct (i.e., N particles give rise to $N\chi$, $2N\theta_{\mathrm{p}}$, and $2N\phi_{\mathrm{p}}$ values since each particle has two rectangular patches). Note that negative values of θ_{p} and ϕ_{p} have no physical meaning and therefore were set to equal 0, in which case the corresponding patches are non-existent.

To assess the tolerance for dispersity in rectangular patch half-opening angles alone, systems with fixed skew angles ($\chi = 70.5°$, where $\sigma_{\chi} = 0$) were considered with various ($\sigma_{\theta_{\mathrm{p}}}$, $\sigma_{\phi_{\mathrm{p}}}$) standard deviation pairs at means of $\mu_{\theta_{\mathrm{p}}} = 10°$ and $\mu_{\phi_{\mathrm{p}}} = 44°$. Figure 5.5**a** shows the results of this in ($\sigma_{\theta_{\mathrm{p}}}$, $\sigma_{\phi_{\mathrm{p}}}$) space where green filled points indicate crystallisation within 100 million MC cycles, as identified *via* a final global Steinhardt bond-order parameter value of $Q_4 > 0.1$ (averaged over the final 1 million MC cycles).

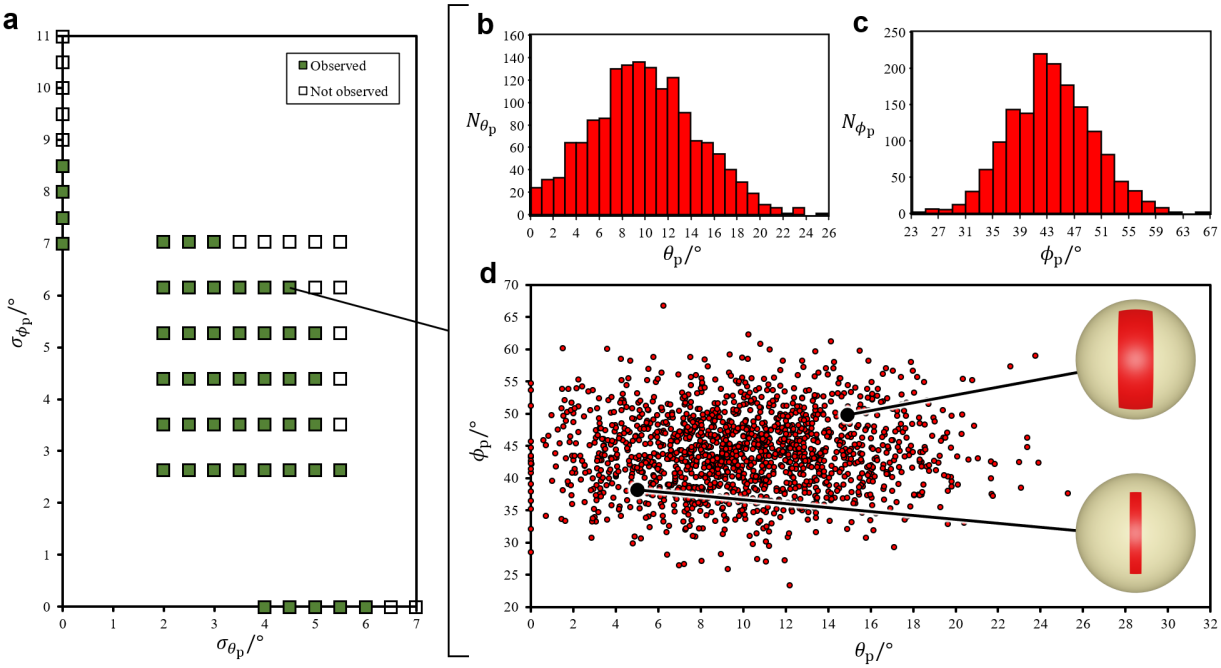


Figure 5.5: **Single colloidal gyroid crystallisation from particles with two rectangular patches of polydisperse coverage.** (**a**) Green filled points indicate crystallisation within 100 million MC cycles following a one-step quench from $T^* = 1$ for systems of $N = 768$ two-patch particles at a density of $\rho^* = 0.3$ with polydisperse (normally distributed) rectangular patch coverage parameters θ_p and ϕ_p, all at the ideal gyroid skew angle ($\chi = 70.5°$). Systems have identical mean patch coverage parameters ($\mu_{\theta_p} = 10°$ and $\mu_{\phi_p} = 44°$) with various standard deviations (σ_{θ_p} and σ_{ϕ_p}). Crystallisation is identified *via* a final global Steinhardt bond-order parameter value of $Q_4 > 0.1$ (averaged over the final 1 million MC cycles). (**b-d**) Distributions of patch parameters for simulations corresponding to ($\sigma_{\theta_p} = 4.5°$, $\sigma_{\phi_p} = 6.16°$), where **b** and **c** show histograms of θ_p and ϕ_p respectively, and **d** shows a scatter graph of the (θ_p, ϕ_p) pairs with schematic particles corresponding to two of the points (as labelled) to visually demonstrate the degree of patch dispersity within the system.

The points where either $\sigma_{\theta_p} = 0$ or $\sigma_{\phi_p} = 0$ reveal the maximum tolerances at which crystallisation is still observed for each isolated half-angle, which are approximately $\sigma_{\theta_p} \leq 6°$ and $\sigma_{\phi_p} \leq 8.5°$. The data shows that combining dispersity in both parameters, as it is reasonable to expect, reduces the maximum tolerance for each parameter. To demonstrate this combined tolerance, Figure 5.5**b-d** shows the corresponding distributions of patch parameters for a point on the boundary corresponding to ($\sigma_{\theta_p} = 4.5°$, $\sigma_{\phi_p} = 6.16°$). Figure 5.5**b** and Figure 5.5**c** show histograms of θ_p and ϕ_p respectively, and Figure 5.5**d** shows a scatter graph of the (θ_p, ϕ_p) pairs with schematic particles corresponding to two of the points (as labelled) to visually demonstrate the degree of patch dispersity within the system.

5.2.1.4 Polydispersity in rectangular patch orientation

To assess the tolerance for dispersity in skew angle alone, a similar study was performed where systems of fixed patch coverage and geometry ($\theta_p = 10°$ and $\phi_p = 44°$, where $\sigma_{\theta_p} = \sigma_{\phi_p} = 0$) were considered with various standard deviations in skew angle σ_χ at a mean of $\mu_\chi = 70.5°$. Figure 5.6**a** shows the final global Steinhardt bond-order parameter Q_4 values, for each system as a function of standard deviation in skew angle σ_χ. The plot clearly shows a crystalline region, which yields colloidal gyroid up to $\sigma_\chi = 13.8°$. Figure 5.6**b** shows the skew angle distribution corresponding to the $\sigma_\chi = 13.8°$ system, and a snapshot of the final configuration. Note that two χ values towards the ends of the distribution are labelled with corresponding patch arrangements to visually demonstrate the degree of skew angle dispersity within the system.

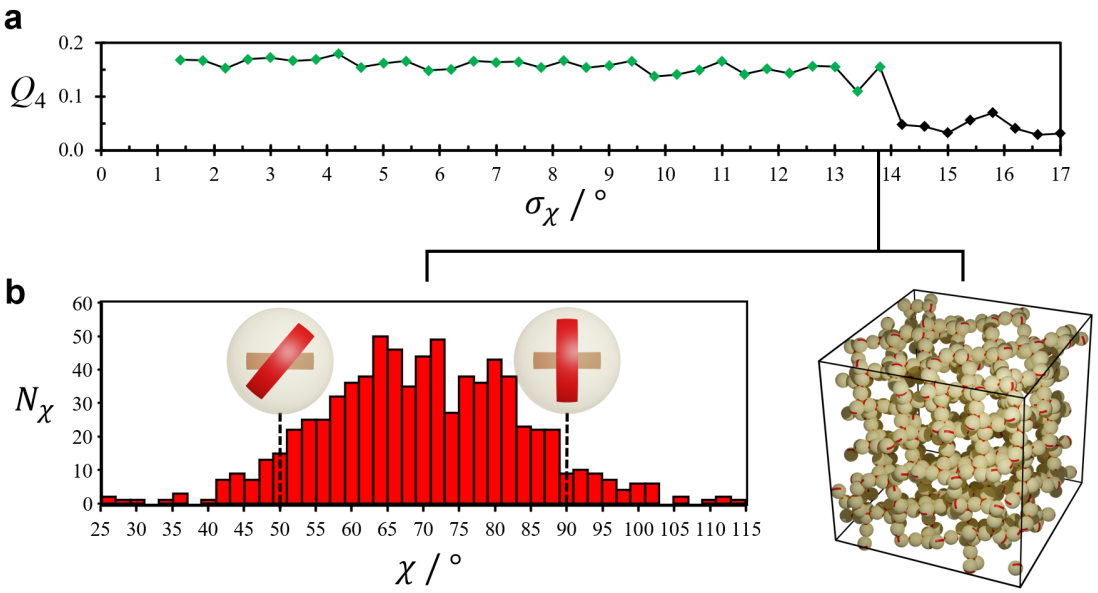


Figure 5.6: **Single colloidal gyroid crystallisation from particles with two rectangular patches of polydisperse skew angle.** (**a**) Final global Steinhardt bond-order parameter Q_4 values, as a function of standard deviation in skew angle σ_χ, for systems of $N = 768$ two-patch particles at a density of $\rho^* = 0.3$ with polydisperse (normally distributed) rectangular patch skew angles χ, all with patch coverage parameters of $\theta_\mathrm{p} = 10°$ and $\phi_\mathrm{p} = 44°$ following a one-step quench from $T^* = 1$. Systems have identical mean skew angles ($\mu_\chi = 70.5°$) with various standard deviations (σ_χ) and green points indicate crystalline configurations (as identified *via* a value of $Q_4 > 0.1$). (**b**) Histogram of skew angles (χ) and a snapshot of the final configuration, for the $\sigma_\chi = 13.8°$ system. Two χ values towards the ends of the distribution are labelled with corresponding patch arrangements to visually demonstrate the degree of skew angle dispersity within the system. Note particles in the snapshot are shown with patch parameter means.

5.2.1.5 Polydispersity in rectangular patch coverage and orientation

To investigate the combination of dispersity in all three rectangular patch parameters, another similar study was performed where systems with ($\sigma_{\theta_\mathrm{p}}$, σ_{ϕ_p}, σ_χ) triples from all possible combinations of $\sigma_{\theta_\mathrm{p}} = 2°, 2.75°, 3.5°$; $\sigma_{\phi_\mathrm{p}} = 4°, 5°, 6°$; and $\sigma_\chi = 5°, 6°, 7°, 9°, 11°, 13°$ were considered at means of $\mu_{\theta_\mathrm{p}} = 10°$, $\mu_{\phi_\mathrm{p}} = 44°$, and $\mu_\chi = 70.5°$.

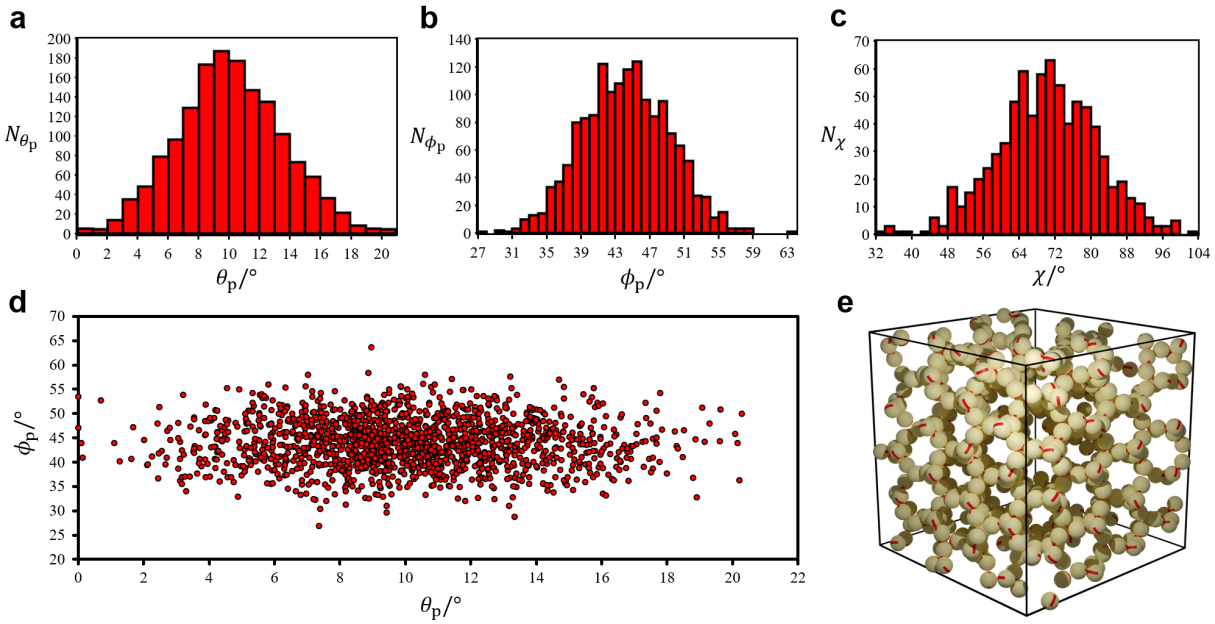


Figure 5.7: **Single colloidal gyroid crystallisation from particles with two rectangular patches of polydisperse coverage and orientation.** (**a-d**) Parameter distributions for a system of $N = 768$ two-patch particles with polydisperse (normally distributed) rectangular patch parameters, which crystallised single gyroid following a one-step quench from $T^* = 1$ to $T^* = 0.105$ at a density of $\rho^* = 0.3$. The patch parameters are centred around means of $\mu_{\theta_\mathrm{p}} = 10°$, $\mu_{\phi_\mathrm{p}} = 44°$, and $\mu_\chi = 70.5°$ with standard deviations of $\sigma_{\theta_\mathrm{p}} = 3.5°$, $\sigma_{\phi_\mathrm{p}} = 5°$, and $\sigma_\chi = 11°$. Histograms of θ_p, ϕ_p, and χ are shown in **a**, **b**, and **c** respectively, and **d** shows a scatter graph of the (θ_p, ϕ_p) pairs. (**e**) Snapshot of the final configuration (where particles are shown with patch parameter means).

In order to demonstrate the levels of dispersity that can be tolerated, data for an edge case system which crystallised colloidal gyroid corresponding to ($\sigma_{\theta_\mathrm{p}} = 3.5°$, $\sigma_{\phi_\mathrm{p}} = 5°$, $\sigma_\chi = 11°$) is shown in Figure 5.7. Figure 5.7**a-d** shows the distributions of patch parameters, where Figure 5.7**a**, Figure 5.7**b**, and Figure 5.7**c** show histograms of θ_p, ϕ_p, and χ respectively, and Figure 5.7**d** shows a scatter graph of the (θ_p, ϕ_p) pairs. Figure 5.7**e** shows a snapshot of the final configuration.

5.2.2 Self-assembly of colloidal gyroid using four circular patches

Particles with two rectangular patches are not the only patch decoration in which the formation of five-particle corner-shared trimer motifs can potentially be restricted to a pre-defined inter-trimer dihedral angle, as conceptualised in Chapter 4 (Section 4.2.1). Another synthetically reasonable [43] patch configuration which can achieve this selection of dihedral angles, is one in which a circular patch, predisposed to form a single contact, is centred on each of the four points of contact formed by the central particle in the desired five-particle motif. Such an arrangement is shown visually in Figure 5.8**a**.

In the following studies these designer particles were modelled using the Kern-Frenkel potential, and Figure 5.8**b** shows the parametrisation used to define such four-patch spherical particles. In this scheme, each hemisphere has two circular patches, each with a half-opening angle α which defines the patch coverage. The centres of these pairs of patches subtend an angle β at the centre of the colloidal sphere, and the relative orientation of the patch pairs is defined in a similar manner as the rectangular-patch case, *via* a skew angle χ.

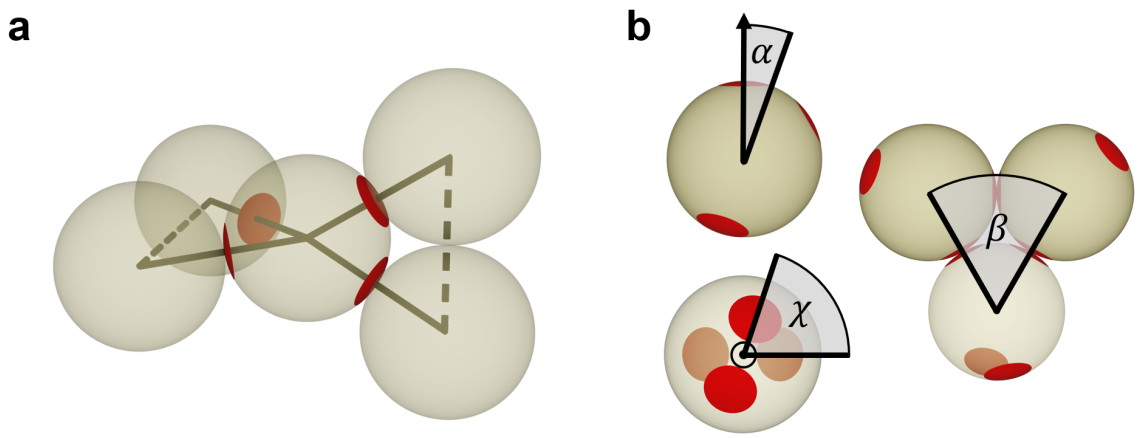


Figure 5.8: **Design and parametrisation of particles with four circular patches.** (**a**) Spherical patchy particles with four circular patches to encode the characteristic five-particle structural motif of the target single gyroid crystal structure. The patches are arranged such that the bonds to the central particle pass through the centres of the patches. These associated bonds are shown in black, where the dashed lines show the bonds which complete the two trigonal units. (**b**) Parametrisation of the size and arrangement of the patches for a four-patch spherical particle with the set of angles α, β and χ.

To investigate the self-assembly behaviour of these designer particles, and determine if they can also self-assemble a single gyroid crystal, a series of Monte Carlo simulations were performed in the NVT ensemble at the approximate colloidal gyroid density of $\rho^* = 0.3$. Systems of $N = 768$ four-patch particles with patch arrangements appropriate for single gyroid formation ($\beta = 60°$, $\chi = 70.5°$ or $109.5°$) over a range of patch coverages ($\alpha = 8°, 10°, 15°, 20°, 22°$) were subjected to a one-step quench from $T^* = 1$. Crystallisation of a single gyroid structure was indeed observed up to $\alpha = 20°$, and Figure 5.9 shows data for an $\alpha = 10°$ system after the temperature was dropped to $T^* = 0.113$. Figure 5.9**a** (top) shows the evolution of the number of trigonal units N_{trig}, and the potential energy per particle U^*/N, where the drop in energy and corresponding growth in trigonal unit count signal a phase transition. Figure 5.9**a** (bottom) shows the evolution of the global Steinhardt bond-

order parameter Q_4, and the number of 10-membered rings $N_{\mathrm{R}_{10}}$, both of which capture the growth of crystalline order. Figure 5.9**b** shows a representative crystalline configuration.

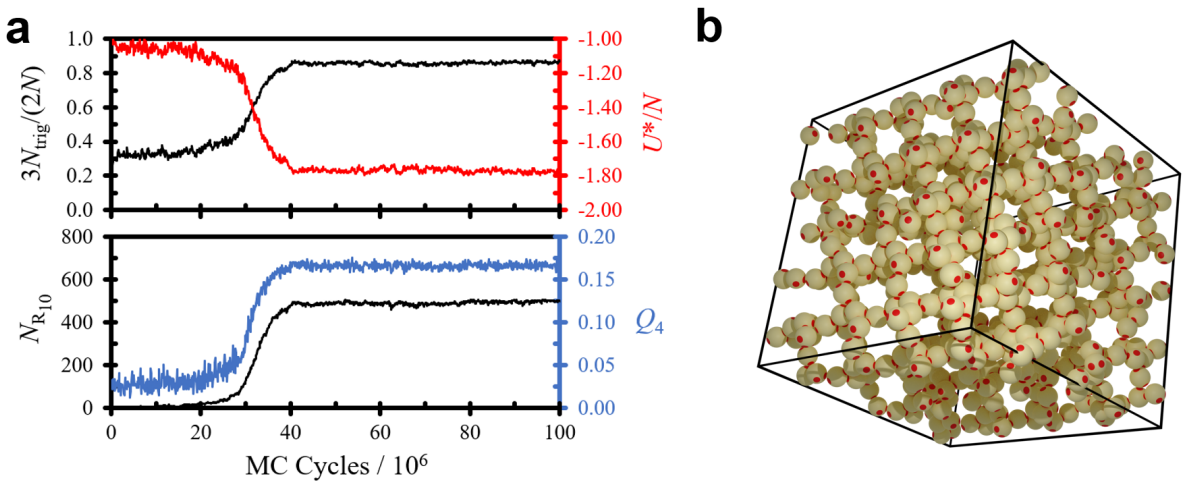


Figure 5.9: **Self-assembly of single colloidal gyroid from particles with four circular patches.** (**a**) Evolution of the number of trigonal planar units N_{trig}, the potential energy per particle U^*/N, the number of 10-membered rings $N_{\mathrm{R}_{10}}$, and the global Steinhardt bond-order parameter Q_4, for a system of $N = 768$ four-patch particles ($\alpha = 10°$, $\beta = 60°$, $\chi = 109.5°$) at a density of $\rho^* = 0.3$ following a one-step quench from $T^* = 1$ to $T^* = 0.113$. (**b**) Representative crystalline configuration.

5.2.2.1 Patch-pair separation angle parameter space for crystallisation

To investigate the range of patch-pair separation angles over which the crystallisation of single colloidal gyroid is observed, a series of Monte Carlo simulations were performed using various patch-pair separations from $\beta = [40°$ to $90°]$. Systems of $N = 768$ four-patch particles at the ideal gyroid skew angle $\chi = 70.5°$, with half-opening angles $\alpha = 15°$ were subjected to a one-step quench from $T^* = 1$ at a density of $\rho^* = 0.3$. Figure 5.10 shows the results of this, where final global Steinhardt bond-order parameter Q_4 values, for each

system are shown as a function of patch-pair separation angle β. The plot shows a clear crystalline region, yielding colloidal gyroid within $\beta = [50° \text{ to } 65°]$.

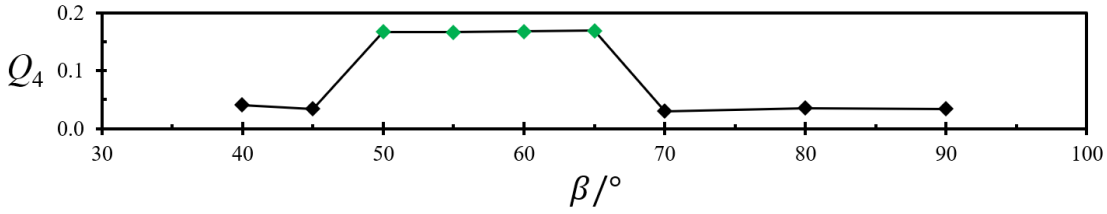


Figure 5.10: **Robustness of patch-pair separation angle space for crystallising single colloidal gyroid.** Final global Steinhardt bond-order parameter values Q_4, as a function of patch-pair separation β, for systems of $N = 768$ four-patch particles with patch parameters of $\alpha = 15°$ and $\chi = 70.5°$ following a one-step quench from $T^* = 1$ at a density of $\rho^* = 0.3$. Green points indicate crystalline configurations (as identified *via* a value of $Q_4 > 0.1$).

5.2.2.2 Polydispersity in circular patch coverage

To investigate how robust single gyroid crystallisation is with regards to dispersity in patch coverage, sets of Monte Carlo simulations were carried out with polydisperse patch coverages. Firstly, a "target" half-opening angle α was chosen to give a population mean of $\mu_\alpha = 15°$. This value was chosen so as to strike a balance between being central (within the range which results in crystallisation) but also far from zero in order to minimise the number of absent patches ($\alpha = 0$) at high levels of dispersity. In the same manner as the rectangular patch system, different degrees of dispersity were obtained by pulling from normal distributions centred around this mean using various standard deviations (σ_α).

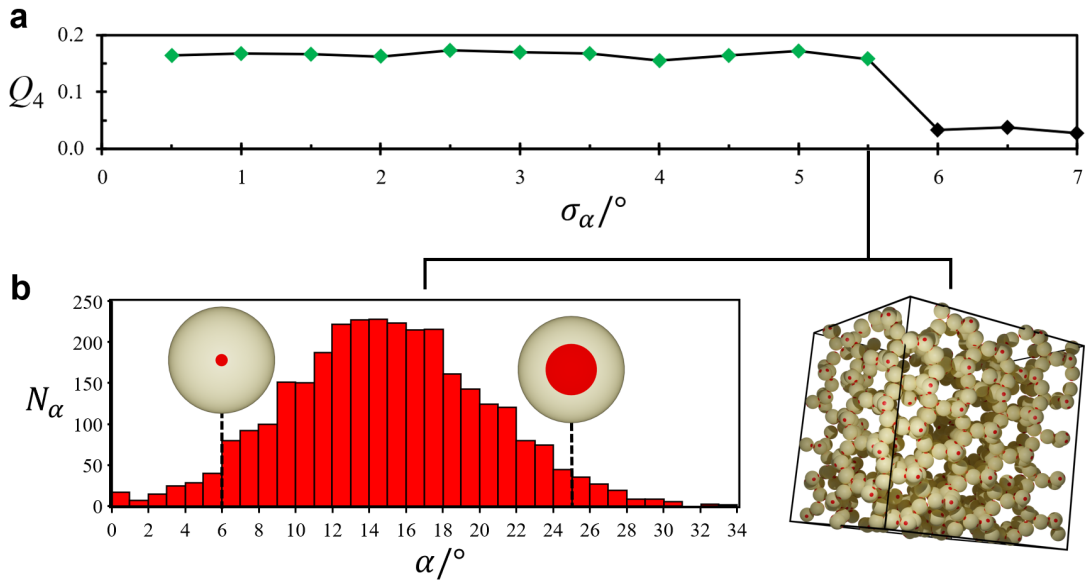


Figure 5.11: **Single colloidal gyroid crystallisation from particles with four circular patches of polydisperse coverage.** (**a**) Final global Steinhardt bond-order parameter Q_4 values, as a function of standard deviation in patch half-opening angles σ_α, for systems of $N = 768$ four-patch particles with polydisperse (normally distributed) patch half-opening angles α, all with patch arrangement parameters of $\beta = 60°$ and $\chi = 70.5°$ following a one-step quench from $T^* = 1$ at a density of $\rho^* = 0.3$. Systems have identical mean patch half-opening angles ($\mu_\alpha = 15°$) with various standard deviations (σ_α) and green points indicate crystalline configurations (as identified *via* a value of $Q_4 > 0.1$). (**b**) Histogram of patch half-opening angles (α) and a snapshot of the final configuration, for the $\sigma_\alpha = 5.5°$ system. Two α values towards the ends of the distribution are labelled with corresponding patch sizes to visually demonstrate the degree of dispersity within the system. Note particles in the snapshot are shown with patch parameter means.

In the following study, systems of $N = 768$ particles were considered at a density of $\rho^* = 0.3$ following a one-step quench from $T^* = 1$, where each patch is distinct (i.e., N particles give rise to $4N\alpha$ values since each particle has four circular patches). Note again that negative values of α have no physical meaning and therefore were set to equal 0, in which case the corresponding patches are non-existent.

To assess the tolerance for dispersity in circular patch coverages, systems with fixed patch arrangements ($\beta = 60°$, $\chi = 70.5°$) were considered with various standard deviations in patch half-opening angle (σ_α) around a mean of $\mu_\alpha = 15°$. Figure 5.11**a** shows the final global Steinhardt bond-order parameter Q_4 values, for each system as a function of standard deviation in patch half-opening angle σ_α. The plot clearly shows a crystalline region, which yields colloidal gyroid up to $\sigma_\alpha = 5.5°$. In order to demonstrate the levels of dispersity that can be tolerated, Figure 5.11**b** shows the patch half-opening angle distribution corresponding to the $\sigma_\alpha = 5.5°$ system, along with a snapshot of the final configuration. Note that two α values towards the ends of the distribution are labelled with corresponding patches to visually demonstrate the degree of patch coverage dispersity within the system.

5.3 Conclusions

In this chapter, two distinct routes to colloidal gyroid are established. The first employs spherical particles with two attractive rectangular patches, where each patch is predisposed to form trigonal units and the patches are oriented such that inter-trimer dihedral angles are enforced to form at the ideal gyroid angles (70.5° or 109.5°). This dihedral angle selection removes competing trimer-based crystals (detailed in Chapter 3) from the energy landscape. The second route uses particles of a similar fundamental design but with four circular patches, where each rectangular patch has essentially been replaced by a pair of circular patches.

The Monte Carlo simulations herein demonstrate the enantiomorphic self-assembly of colloidal gyroid for both systems, and show that crystallisation occurs over a significant parameter space. Particles with rectangular patches are modelled using the modified Kern-Frenkel model developed in Chapter 4, and the four-patch system is modelled using standard Kern-Frenkel [104]. Studies into the effects of patch polydispersity are undertaken, and it is established that appropriate selection of target patch parameters yield an impressive tolerance for patch dispersity in both coverage and orientation. This along with the patch arrangements being proposed in line with synthetic advancements [43, 63] lends the self-assembly of single colloidal gyroid, *via* the routes established here, to experimental realisation.

Chapter Six

Self-Assembly Routes to Double Colloidal Gyroid

6.1 Introduction

In Chapter 5, Monte Carlo simulations demonstrate the programmed self-assembly of chiral patchy spheres, with either two rectangular or four circular attractive patches in an appropriate arrangement into single gyroid crystals. The success of these bottom-up routes poses the question as to whether these designer particles could also offer self-assembly routes to double gyroid crystals. Though double gyroid structures are not uncommon with regards to self-assembly [90, 98–100], making use of building blocks capable of assembling a single network opens up the prospect of a staged assembly route to double gyroid, which potentially offers a platform to investigate the templated self-assembly of single gyroid.

In this chapter, it is established that a racemic mixture of the chiral patchy particles with rectangular attractive patches considered in Chapter 5 can stabilise a double colloidal gyroid crystal, but a simple racemic mixture alone is insufficient to self-assemble into one. Two alternative and synthetically viable routes to a double colloidal gyroid crystal are then

proposed, and both are demonstrated to result in the self-assembly of the target structure *in silico*. The self-assembly of corner-shared trimer-forming particles with circular patches (considered in Chapter 3) is also investigated, in the presence of a single colloidal gyroid template.

6.2 Results and discussion

6.2.1 Stabilising double colloidal gyroid using a racemic mixture

A double gyroid crystal consists of two interpenetrating single gyroids of opposing chirality. Chapter 5 demonstrates the enantiomorphic self-assembly of single colloidal gyroid crystals from designer chiral spheres, as shown schematically in Figure 6.1**a** for the case of particles with rectangular patches. It therefore follows that a racemic mixture of single colloidal gyroid stabilising particles can stabilise a double colloidal gyroid crystal, as shown in the form of a cubic unit cell in Figure 6.1**b**, where the yellow and pink particles are of opposing chirality as indicated by their red and green patches respectively.

To determine if a racemic mixture of chiral patchy spheres with two rectangular patches alone is sufficient to result in the self-assembly of a double colloidal gyroid crystal, Monte Carlo simulations in the NVT ensemble were performed at a density of $\rho^* = 0.6$ (double the approximate single colloidal gyroid density). Systems of $N = 648$ particles with rectangular patch parameters appropriate for crystallising single gyroid ($\theta_\mathrm{p} = 10°$, $\phi_\mathrm{p} = 44°$) in a 1:1 mixture of χ values ($\chi_1 = 70.5°$, $\chi_2 = 109.5°$), were subjected to one-step quenching from $T^* = 1$ to various temperatures around the approximate transition for single gyroid for the patch geometry under consideration ($T^* = [0.1$ to $0.13]$ with a resolution of 0.0025). Note that the interactions between patches on the two types of particles here are identical

(i.e., the only difference between the particle types is their relative patch placement). These simulations were run up to 400 million MC cycles, and crystallisation was not observed. Amorphous corner-shared trimer networks are formed instead, and bonding analysis reveals that there are no signs of de-mixing throughout the simulations. The reason crystallisation is not observed here is likely related to this need to de-mix the particles in order to form a double gyroid nucleus, which involves an entropy cost.

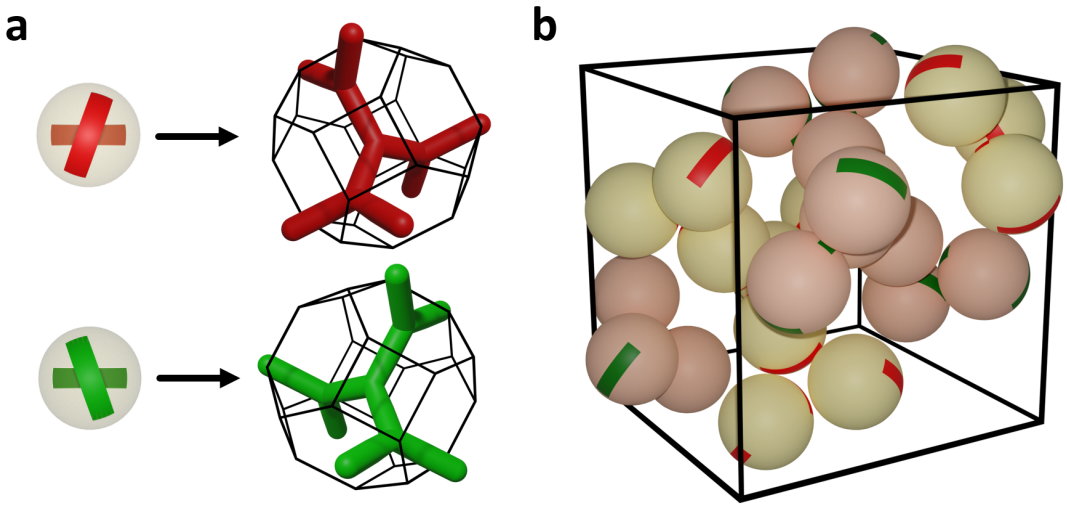


Figure 6.1: **Stabilising double colloidal gyroid using a racemic mixture.** (**a**) Rationally designed particles with staggered rectangular patches and the Wigner-Seitz cells of the corresponding single gyroid enantiomorphs (represented as tubular network gyroid structures) that they selectively form. (**b**) Conventional unit cell of double colloidal gyroid, highlighting the racemic mixture of designer particles required to stabilise it, where the two distinct chiral networks are shaded differently.

To investigate if the nucleation barrier alone is the reason double gyroid crystallisation is not observed in a simple racemic mixture of chiral single gyroid-forming particles, Monte Carlo simulations were carried out from an initial configuration where half the simulation cell contains crystallised double gyroid (i.e., the fluid particles are interfaced between slabs

of double gyroid crystal). To achieve this an orthorhombic simulation cell is generated from the addition of two cubic cells, one being a double colloidal gyroid crystal and the other a fluid equilibrated at $T^* = 1$.

Systems of $N = 1296$ particles with two equal-size staggered rectangular patches of appropriate geometry for crystallising single gyroid ($\theta_p = 10°$, $\phi_p = 44°$) in a 1:1 mixture of χ values ($\chi_1 = 70.5°$, $\chi_2 = 109.5°$) were subjected to one-step quenching from $T^* = 1$ to various temperatures around the approximate transition for single gyroid for the patch geometry under consideration ($T^* = [0.1$ to $0.13]$ with a resolution of 0.001). It is worth noting that the density of the orthorhombic cell under consideration here is $\rho^* \approx 0.5467$ as a result of lengthening the simulation cell in the dimension along which the two cubic cells were added. This was done to remove the possibility of overlapping particles in the initial configuration of the interfaced simulation.

In order to probe changes in the size of the double gyroid crystal, the largest cluster of particles involved in the formation of two trimers was tracked, considering either only χ_1 particles or only χ_2 particles. This is an effective measure of the size of each single gyroid network. Figure 6.2 shows data for a system after the temperature is dropped to $T^* = 0.121$, where Figure 6.2**a** shows the evolution of the largest clusters of particles involved in the formation of two trimers considering only χ_1 particles (red line) and only χ_2 particles (blue line). The growth is clearly demonstrated. It is worth noting that initial sizes of the largest clusters in Figure 6.2**a** are less than $N/4$, since the addition of the fluid cell resulted in the creation of two crystal surfaces which were previously connected due to the periodic boundaries in the cubic crystalline cell. Figure 6.2**b-c** shows the growth visually with snapshots of the largest clusters of particles which form two trimers considering χ_1 particles (Figure 6.2**b**) and χ_2 particles (Figure 6.2**c**) after 100 thousand (top) and 250 million (bottom) MC cycles.

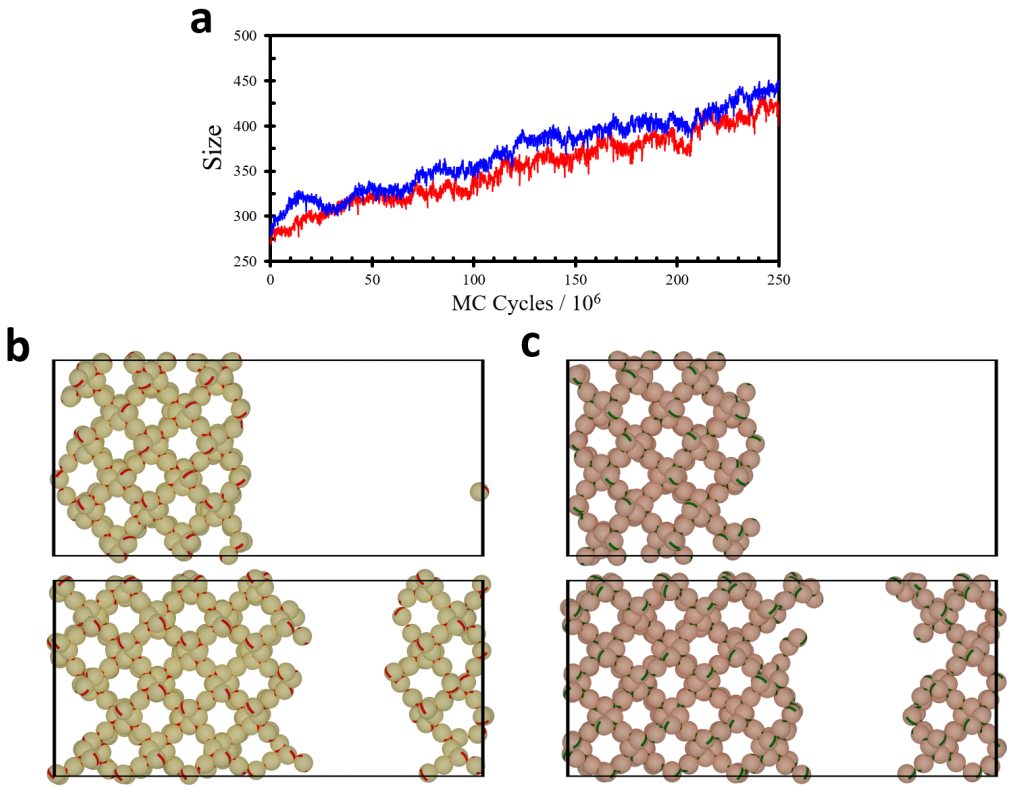


Figure 6.2: **Growth of a double colloidal gyroid crystal interfaced with a racemic fluid.** A double colloidal gyroid crystal interfaced with a racemic fluid of $N = 648$ patchy spheres with two equal-size staggered rectangular patches ($N = 1296$ particles in total at a density of $\rho^* \approx 0.5467$). The particles considered have patches with half-opening angles $\theta_p = 10°$ and $\phi_p = 44°$ with patch-patch interaction strengths of $\epsilon = 1$, and have a 1:1 mixture of χ values ($\chi_1 = 70.5°$, $\chi_2 = 109.5°$). The fluid part of the cell was equilibrated at $T^* = 1$ prior to the construction of the orthorhombic interfaced cell. (**a**) Evolution of the largest cluster of particles involved in the formation of two trimers after the temperature is dropped to $T^* = 0.121$, considering only χ_1 particles (red line), and only χ_2 particles (blue line). (**b-c**) Snapshots showing the growth of the largest clusters in **a**, where the largest clusters shown in **b** (yellow) and **c** (pink) correspond to χ_1 and χ_2 particles respectively. The top and bottom snapshots are after 100 thousand and 250 million MC cycles respectively.

It appears then that altering the system to provide a driving-force for de-mixing of the particles, such that bonding between patches of like χ values is promoted, could potentially provide a self-assembly route to double colloidal gyroid crystals.

6.2.2 Self-assembly *via* DNA-mediated interactions

One method of providing a driving force for de-mixing is to alter the interaction matrix by "switching off" interactions between patches on particles of one chirality with patches on particles of the opposing chirality. Such an interaction matrix can be achieved experimentally, using DNA-mediated interactions where the patches are functionalised with appropriate DNA sequences [117].

To investigate the self-assembly of these DNA-coated chiral patchy particles, Monte Carlo simulations in the NVT ensemble were performed at a density of $\rho^* = 0.6$ (double the approximate single colloidal gyroid density) for systems of $N = 1536$ particles with rectangular patch parameters appropriate for crystallising single gyroid ($\theta_\mathrm{p} = 10°$, $\phi_\mathrm{p} = 44°$). In this case, particles were in a 1:1 mixture of χ values ($\chi_1 = 70.5°$, $\chi_2 = 109.5°$), where patches belonging to particles of like χ values had patch-patch interaction strengths of $\epsilon_{\chi_1-\chi_1} = \epsilon_{\chi_2-\chi_2} = 1$, and patch-patch interactions between different χ valued particles had a strength of zero ($\epsilon_{\chi_1-\chi_2} = 0$). Systems were equilibrated at a temperature of $T^* = 1$ and subjected to a one-step quench.

Figure 6.3**a** shows the evolution of the number of trigonal units N_trig, and the potential energy per particle U^*/N, for a system after the temperature is dropped to $T^* = 0.115$. The significant drop in energy and corresponding growth in trigonal unit count suggest the occurrence of a phase transition. The final configuration is almost exclusively comprised of 10-membered rings, and the RDF confirms that a double gyroid crystal has formed. The

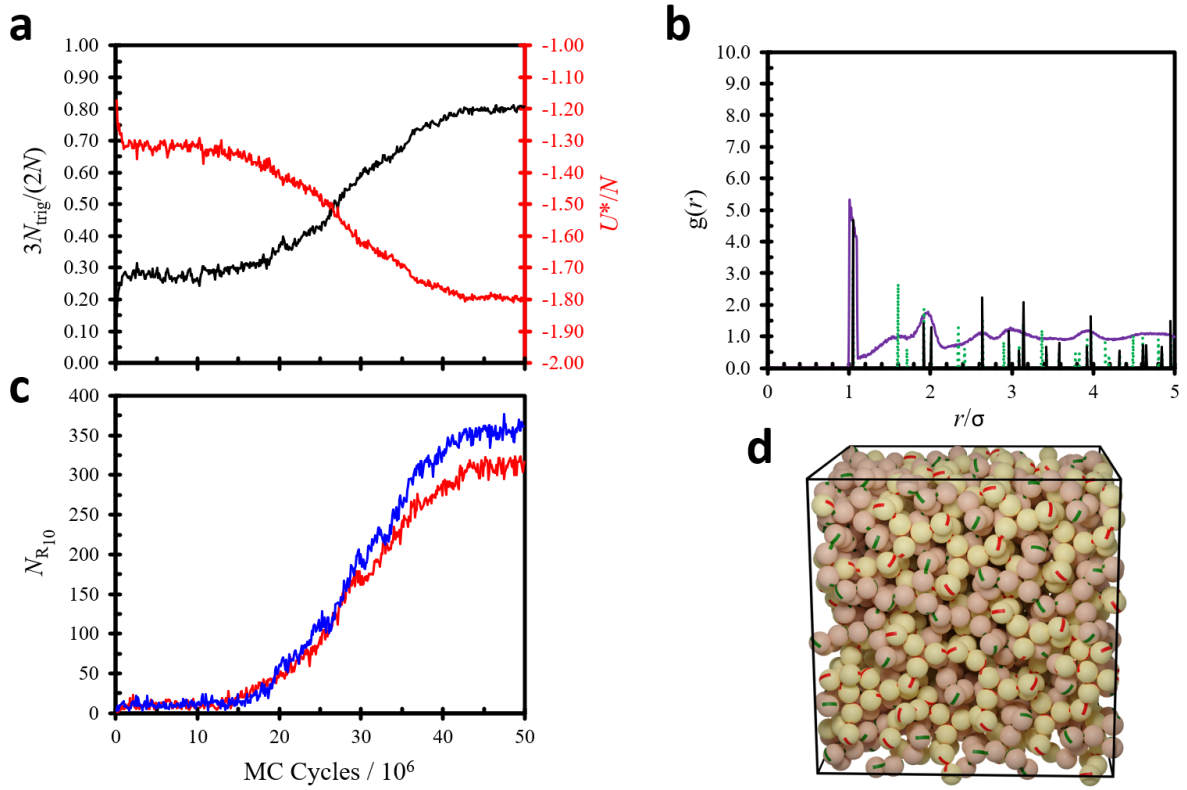


Figure 6.3: **Self-assembly of double colloidal gyroid *via* DNA-mediated interactions.** A system of $N = 1536$ DNA-coated patchy spheres with two equal-size staggered rectangular patches with half-opening angles ($\theta_p = 10°$, $\phi_p = 44°$), with a 1:1 mixture of χ values ($\chi_1 = 70.5°$, $\chi_2 = 109.5°$) with patch-patch interaction strengths $\epsilon_{\chi_1-\chi_1} = \epsilon_{\chi_2-\chi_2} = 1$ and $\epsilon_{\chi_1-\chi_2} = 0$, at a density of $\rho^* = 0.6$. Showing data after the temperature is dropped from $T^* = 1$ to $T^* = 0.115$. (**a**) Evolution of the number of trigonal planar units N_{trig}, and the potential energy of the system U^*/N. (**b**) RDF averaged over the last 1 million MC cycles for all particles (purple line), and RDF of ideal single (black line) and double (dashed green line) colloidal gyroid scaled by an arbitrary factor for visibility. (**c**) Evolution of the number of 10-membered rings, considering χ_1 particles only (red line), and χ_2 particles only (blue line). (**d**) Snapshot of the final configuration.

RDF of all particles is displayed in Figure 6.3**b** along with the ideal single and double colloidal gyroid peak positions. In order to probe the growth of the constituent single gyroid networks, the 10-membered rings considering only χ_1 particles, and only χ_2 particles were tracked and their evolution along the same trajectory is shown in Figure 6.3**c**. From this it is clear that the networks nucleate and grow together. A snapshot of the final configuration is displayed in Figure 6.3**d**, where the constituent χ_1 and χ_2 particles are shaded in yellow and pink respectively.

6.2.3 Self-assembly *via* a hierarchy of interactions

Another way to introduce a driving force for de-mixing is to alter the interaction matrix by introducing a hierarchy of interaction strengths, where the interaction strength of patches on particles of one chirality is stronger than that of patches on particles of the opposing chirality. With such an interaction matrix, the assembly is anticipated to proceed *via* two stages upon cooling [76, 82, 85]. If successful, the first stage of assembly would take place at a temperature where the stronger interactions between one enantiomorph dominate, driving their crystallisation into a single colloidal gyroid structure of a given chirality. This leaves a fluid of weaker interacting particles of the opposing chirality in the pores of the crystal. The second stage would then take place at a lower temperature where the weaker interactions come into play, driving their crystallisation into a second single colloidal gyroid, thus yielding a double colloidal gyroid crystal.

To investigate the feasibility of this approach, a series Monte Carlo simulations were performed for systems of $N = 1536$ particles with a 1:1 mixture of χ values ($\chi_1 = 70.5°$, $\chi_2 = 109.5°$) with patch-patch interaction strengths $\epsilon_{\chi_1-\chi_1} = 5$ and $\epsilon_{\chi_2-\chi_2} = 1$ at a density of $\rho^* = 0.6$, for patch geometries known to crystallise single gyroid ($\theta_\mathrm{p} = 10°$, $\phi_\mathrm{p} = 44°$). Note that the strength of mixed interactions was taken to be $\epsilon_{\chi_1-\chi_2} = \sqrt{\epsilon_{\chi_1-\chi_1}\epsilon_{\chi_2-\chi_2}} \approx 2.236$.

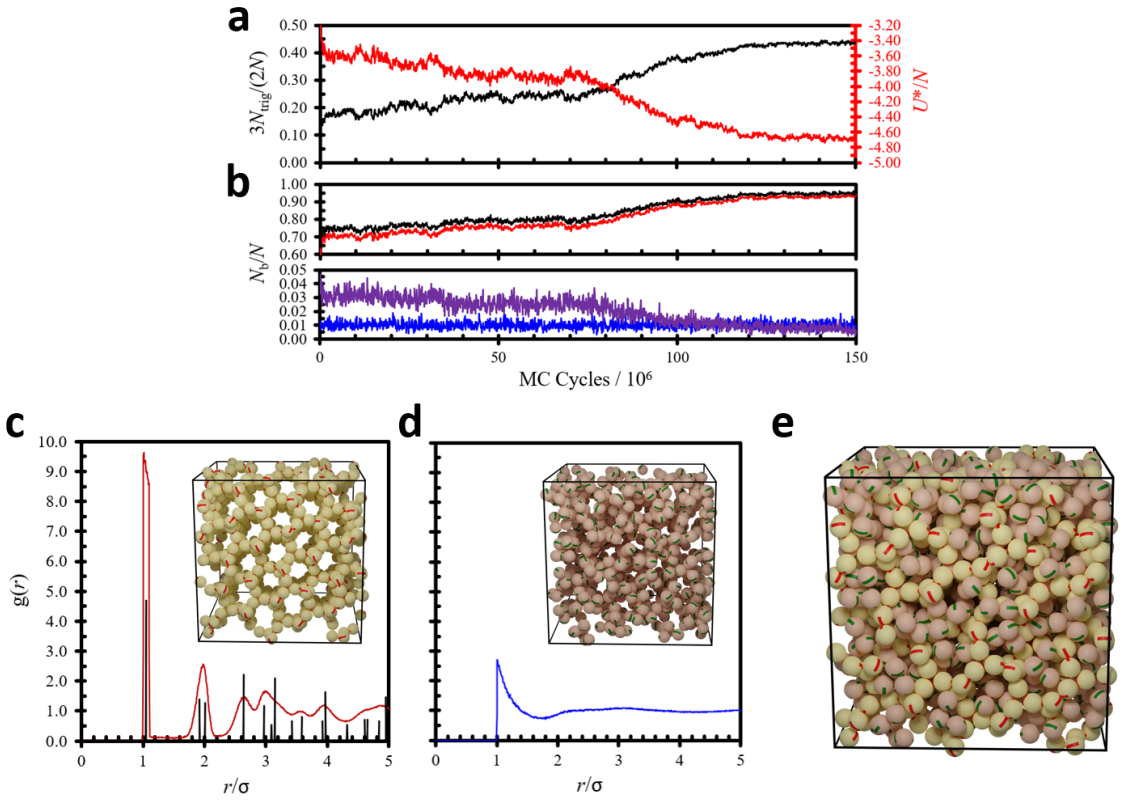


Figure 6.4: **First stage of assembly of double colloidal gyroid.** For a system of $N = 1536$ patchy spheres with two equal-size staggered rectangular patches with half-opening angles ($\theta_p = 10°$, $\phi_p = 44°$), with a 1:1 mixture of χ values ($\chi_1 = 70.5°$, $\chi_2 = 109.5°$) with patch-patch interaction strengths $\epsilon_{\chi_1-\chi_1} = 5$ and $\epsilon_{\chi_2-\chi_2} = 1$, at a density of $\rho^* = 0.6$. Showing data after the temperature is dropped from $T^* = 2$ to $T^* = 0.56$. (**a**) Evolution of the number of trigonal planar units N_{trig} (black line), and the potential energy per particle U^*/N (red line). (**b**) Evolution of the number of bonds (black line), strong-strong/χ_1-χ_1 bonds (red line), strong-weak/χ_1-χ_2 bonds (purple line), and weak-weak/χ_2-χ_2 bonds (blue line) along the same trajectory. (**c**) RDF averaged over the last 10 million MC cycles for strong-patch/χ_1 particles (red line), and RDF of ideal single colloidal gyroid scaled by an arbitrary factor for visibility (black line). (**d**) RDF averaged over the last 10 million MC cycles for weak-patch/χ_2 particles (blue line). (**e**) Snapshot of the final configuration. Note the RDF insets show representative snapshots of the corresponding particles under consideration.

Systems were subjected to a one-step quenching from a temperature of $T^* = 2$. Figure 6.4**a** shows the evolution of the number of trigonal planar units N_{trig}, and the potential energy per particle U^*/N, for a system after the temperature is dropped to $T^* = 0.56$ (i.e., during the first stage of assembly). Figure 6.4**b** shows the number of bonds by their nature along the same trajectory. The significant drop in energy and corresponding growth in the number of trigonal units signals the occurrence of a phase transition, supported by the growth in the number of strong-strong/χ_1-χ_1 bonds and the suppression of mixed bonds as the strong patches are saturated by the formation of a strong-patch/χ_1 crystal. Figure 6.4**c** shows the RDF of strong-patch/χ_1 particles only (averaged over the last 10 million cycles), along with the ideal single colloidal gyroid peak positions which match closely confirming that a strong-patch/χ_1 single colloidal gyroid crystal has been formed. Figure 6.4**d** shows the RDF of weak-patch/χ_2 particles only, displaying hard-sphere fluid-like character. Figure 6.4**e** shows a representative configuration after the first stage of assembly.

Figure 6.5**a** shows the evolution of the number of trigonal planar units N_{trig}, and the potential energy per particle U^*/N, after the temperature is dropped from $T^* = 0.56$ to $T^* = 0.13$ (i.e., during the second stage of assembly). The drop in energy and corresponding growth in the number of trigonal units signals the occurrence of a phase transition, and is notably much sharper than the first stage. Figure 6.5**b** displays the number of bonds by their nature along the same trajectory, showing that the number of strong-strong/χ_1-χ_1 bonds remains essentially unchanged and that weak-weak/χ_2-χ_2 bonds are being formed. The discrepancy between strong-strong/χ_1-χ_1 and weak-weak/χ_2-χ_2 bonds is due to an amplification of the grain boundaries already present in the strong-patch/χ_1 crystal, which are mostly due to the crystalline growth being misaligned with the simulation box. The small growth in the number of mixed bonds is likely due to interactions at these grain boundaries, where the strong-patch/χ_1 particles are unsaturated and it is therefore possible and also energetically favourable for mixed bonds to form as opposed to alternative weak-weak/χ_2-χ_2

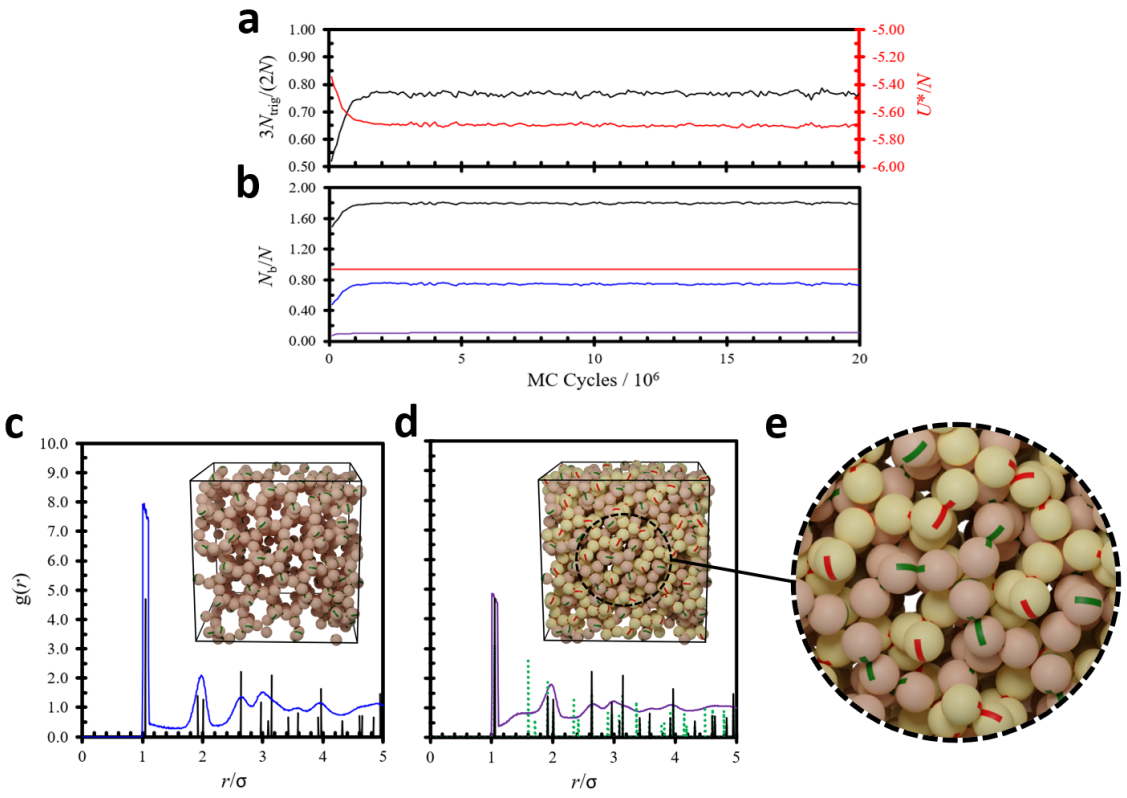


Figure 6.5: **Second stage of assembly of double colloidal gyroid.** Following from the system in Figure 6.4. Showing data after the temperature is dropped from $T^* = 0.56$ to $T^* = 0.13$. (**a**) Evolution of the number of trigonal planar units N_{trig} (black line), and the potential energy per particle U^*/N (red line). (**b**) Evolution of the number of bonds (black line), strong-strong/χ_1-χ_1 bonds (red line), strong-weak/χ_1-χ_2 bonds (purple line), and weak-weak/χ_2-χ_2 bonds (blue line) along the same trajectory. (**c**) RDF averaged over the last 10 million MC cycles for weak-patch/χ_2 particles (blue line), and RDF of ideal single colloidal gyroid scaled by an arbitrary factor for visibility (black line). (**d**) RDF averaged over the last 10 million MC cycles for all particles (purple line), and RDF of ideal single (black line) and double (dashed green line) colloidal gyroid scaled by an arbitrary factor for visibility. (**e**) Zoom-in of snapshot which highlights the interlocking crystals. Note the RDF insets show representative snapshots of the corresponding particles under consideration.

bonds. Figure 6.5**c** shows the RDF of weak-patch/χ_2 particles only (averaged over the last 10 million cycles), along with the ideal single colloidal gyroid peak positions which match closely confirming that a second single colloidal gyroid crystal has now been formed. Figure 6.5**d** shows the RDF of all particles, along with the ideal single and double colloidal gyroid peak positions which confirm the formation of double colloidal gyroid crystal. The ideal peaks present in double gyroid but not in single gyroid are inter-crystal peaks, and therefore due to the movement of one constituent crystal relative to the other are very broad. Figure 6.5**e** shows a zoom-in of a representative configuration of the double gyroid crystal formed, highlighting the interlocking single colloidal gyroids.

6.2.4 Templated self-assembly from particles with circular patches

Noting that, for the patch parameters considered in Section 6.2.3, the second stage of assembly is observed as high as $T^* = 0.135$, whereas assembly in absence of the first network (i.e., assembly of single colloidal gyroid) is observed in simulations only as high as $T^* = 0.11$. It was suspected that there could be a strong templating effect resulting from the presence of the first single gyroid crystal. To investigate whether this is indeed the case, a series of Monte Carlo simulations were carried out using systems of two-patch spheres with a circular patch on each hemisphere (triblock patchy particles) – which have been shown to form kagome crystals for patch coverages predisposed to from trimer units (as demonstrated in Chapter 3). These simulations are initialised from a double colloidal gyroid crystal, where the A particles which comprise one of the constituent single gyroids are distinct from the B particles which make up the other. The patch-patch interaction strengths are set such that one single gyroid is strongly bound ($\epsilon_{\mathrm{AA}} = 5$) and the remaining gyroid is weakly bound ($\epsilon_{\mathrm{BB}} = 1$). Note that mixed interactions were allowed, where $\epsilon_{\mathrm{AB}} = \sqrt{\epsilon_{\mathrm{AA}}\epsilon_{\mathrm{BB}}} \approx 2.236$. The weakly bound single gyroid is then melted at $T^* = 0.3$, to yield a weak-patch particle fluid

dispersed within the pores of the strongly bound single gyroid crystal (which does not melt at this temperature).

Figure 6.6 presents data for a system of $N = 1536$ two-patch particles with circular patches on each hemisphere defined by a half-opening angle of $\theta = 34°$ at a density of $\rho^* = 0.6$. Figure 6.6a shows the evolution of the number of trigonal planar units N_{trig}, and the potential energy per particle U^*/N, after the temperature is dropped from $T^* = 0.3$ to $T^* = 0.12$. A sharp drop in energy is observed alongside a corresponding growth in the number of trigonal units as they both approximately reach the values for a perfect double gyroid crystal. To probe changes in the local order of the system, the inter-trimer dihedral angle distributions of the weak-patch/B particles averaged over different intervals of the simulation were calculated. The distributions over the first and last 2 million MC cycles are shown in Figure 6.6b, where it can be seen that within the first 2 million cycles (before crystallisation is complete) there is a clear promotion of dihedral angles which correspond to the opposite handedness of the template gyroid crystal. Once crystallisation is complete the dihedral angle distribution becomes much narrower around the ideal angle (approximately 109.5°), due to the crystalline structure limiting localised distortions. Figure 6.6**c** shows the RDF of weak-patch/B particles only (averaged over the last 10 million cycles), along with the ideal single colloidal gyroid peak positions which match closely confirming that a second single colloidal gyroid crystal has been been formed. Figure 6.6**d** shows a snapshot of the resulting double gyroid crystal (i.e., the final configuration).

When investigating the nucleation pathway, tracking the largest cluster of non-template particles does not reveal much since at temperatures where the transition can be observed the system quickly becomes essentially interconnected through short-lived reversible bonding. A much more revealing metric is the largest cluster of particles involved in the formation of trigonal units, which is from hereon referred to as the largest trimer cluster. Figure 6.7 shows higher resolution data for the first 5 million MC cycles of the trajectory in Figure 6.6,

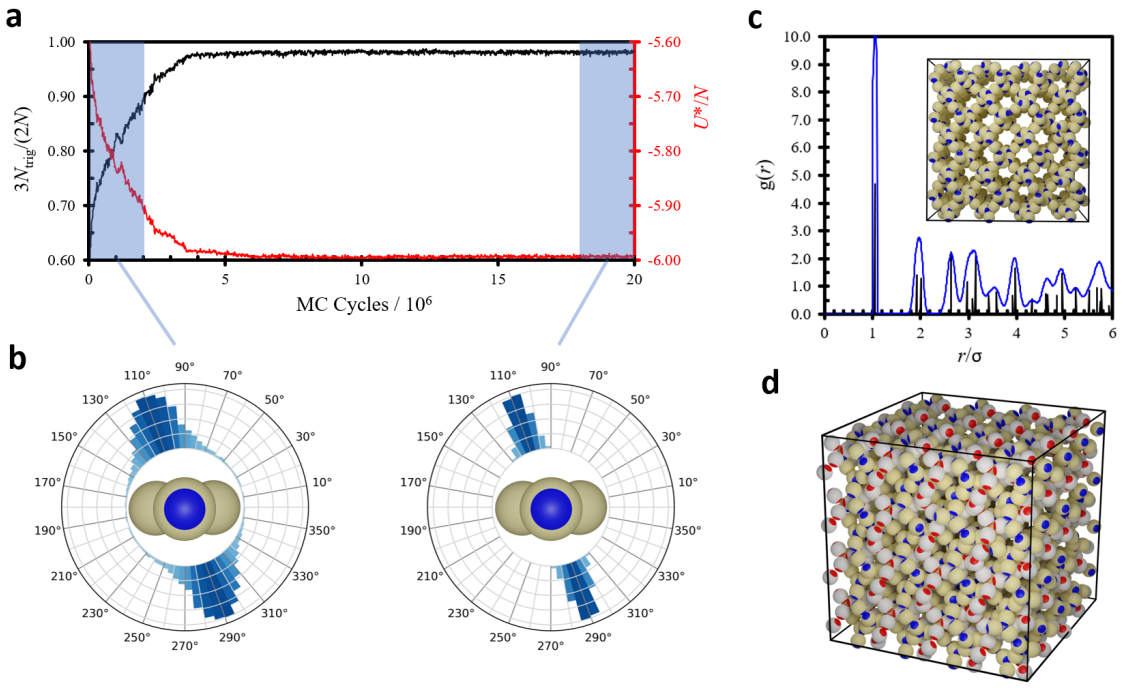


Figure 6.6: **Templating colloidal gyroid self-assembly from patchy particles with two circular patches.** For a system of $N = 1536$ two-patch particles with circular patches on each hemisphere defined by a half-opening angle of $\theta = 34°$ at a density of $\rho^* = 0.6$, where half of the particles are distinct. The simulation is initialised from a double colloidal gyroid crystal where the A particles which comprise one of the constituent single gyroids are distinct from the B particles which make up the other, where the patch-patch interaction strengths are $\epsilon_{AA} = 5$ and $\epsilon_{BB} = 1$. The system was equilibrated at $T^* = 0.3$ so that the weakly bound single gyroid melts. Showing data after the temperature is dropped from $T^* = 0.3$ to $T^* = 0.12$. (**a**) Evolution of the number of trigonal planar units N_{trig}, and the potential energy per particle U^*/N. (**b**) weak-patch/B particle inter-trimer dihedral angle distributions averaged over the first and last 2 million MC cycles, as shaded in **a**. (**c**) RDF of weak-patch/B particles averaged over the last 10 million MC cycles (blue line), and RDF of ideal single colloidal gyroid scaled by an arbitrary factor for visibility (black line). (**d**) Snapshot of the final configuration, where the white particles comprise the artificially inserted strong-patch/A particle single gyroid crystal. Note the RDF inset shows a representative snapshot of the corresponding particles under consideration.

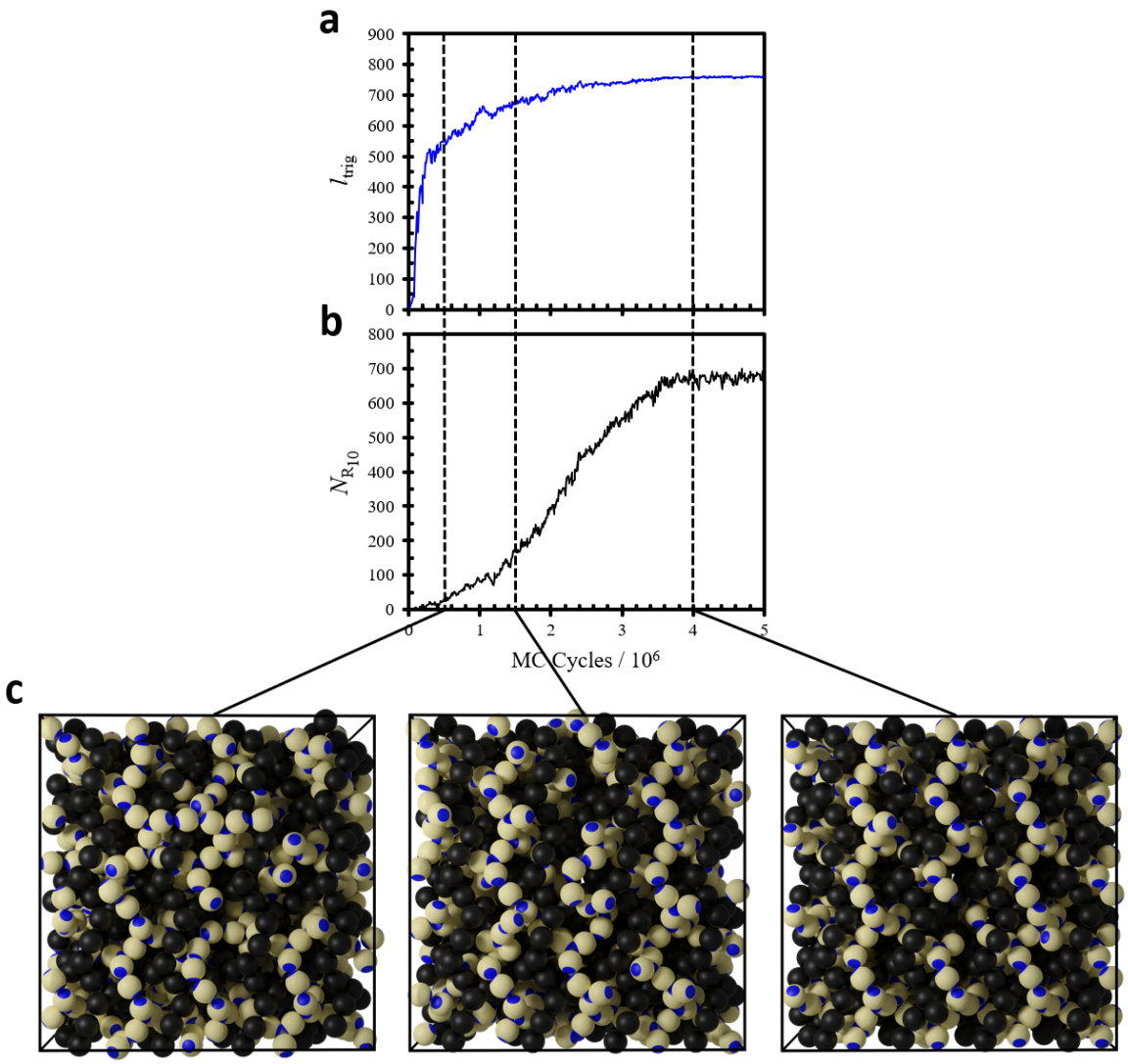


Figure 6.7: **Probing the self-assembly pathway of templated double colloidal gyroid from patchy particles with two circular patches.** Data for the first 5 million MC cycles of the same trajectory as Figure 6.6 (**a**) Evolution of the largest trimer cluster l_{trig}, considering only non-template particles. (**b**) Evolution of the 10-membered ring count $N_{\mathrm{R_{10}}}$, considering only non-template particles. (**c**) Snapshots of configurations after 500 thousand, 1.5 million, and 4 million MC cycles (as labelled in **a** and **b**), where the template particles are shown in black.

where Figure 6.7**a** shows the evolution of the largest trimer cluster l_{trig}. Comparing this to the evolution of 10-membered rings $N_{\text{R}_{10}}$, displayed in Figure 6.7**b**, shows that growth in the largest trimer cluster precedes crystallisation – revealing a non-classical nucleation pathway. Figure 6.7**b** shows snapshots after 500 thousand, 1.5 million, and 4 million MC cycles (as labelled), where the template particles are shown in black. The first snapshot (after 500 thousand MC cycles) is pre-10-membered ring growth, but after the large increase in the largest trimer cluster begins levelling off, and it reveals the solid-like interconnected structure within the template pores. The second and third snapshots (after 1.5 million and 4 million MC cycles respectively) are shortly after 10-membered ring growth occurs, and after it has levelled off respectively. These snapshots capture the formation of a non-template solid-like structure which then gradually re-configures into a single colloidal gyroid crystal of opposite handedness to the template – maximising the number of patch-patch contacts and resulting in a double colloidal gyroid crystal. Dihedral angle analysis at this higher resolution reveals that chirality develops immediately, which is also the case for, and principle behind, the chiral patch arrangements explored in Chapter 5. An explanation for this emerging chirality from the non-template particles, is that the chiral pores within template crystal promote the formation of dihedral angles of opposing chirality to the template.

6.3 Conclusions

This chapter builds on the results of Chapter 5 and establishes that a racemic mixture of chiral patchy spheres with two staggered rectangular patches, can stabilise a double colloidal gyroid crystal. Monte Carlo simulations demonstrate that a simple racemic mixture of these particles is insufficient to self-assemble a double gyroid crystal within the length of the trajectories simulated. This is attributed to the entropy cost associated with the formation of a double gyroid nucleus, in which particles of one chirality must only bond to those of the

same chirality.

Two alternative modifications to the system are proposed, in order to provide a driving-force for de-mixing the particles and hence a self-assembly pathway to double colloidal gyroid. The first modification involves a racemic mixture in which the interactions between particles of opposing chirality are "switched off". Experimentally this can be accomplished *via* the use of DNA-mediated interactions with appropriate DNA sequences [117]. The alternative modification invokes a hierarchical self-assembly approach [76, 82, 85], in which patches belonging to particles of one chirality interact more strongly than patches on particles of the opposing chirality, breaking the assembly down into two stages. Both modifications result in the self-assembly of a double colloidal gyroid crystal *in silico*.

It is identified that the second stage of assembly in the hierarchical approach (Section 6.2.3) is very abrupt, and it was suspected that the single gyroid network assembled in the first stage was templating the second stage of assembly. To investigate this, particles with a trimer-forming circular patch on each hemisphere were dispersed within a template single gyroid crystal and shown to self-assemble into a single colloidal gyroid crystal of opposing handedness to the template crystal. This is in contrast to the self-assembly of the same particles in absence of the template crystal, which are shown to form kagome planes in Chapter 3.

This ability to template the formation of a single colloidal gyroid crystal, from simpler patchy particles with an achiral patch arrangement, has potential applications in the fabrication of single colloidal gyroid crystals. In Chapter 5, it is established that designer particles with chiral patch arrangements are required for the self-assembly of single colloidal gyroid to take place. These chiral particles are much more challenging to synthesise than the relatively simplistic triblock patchy particles [64], therefore a possible method of scaling-up and reducing the cost of single colloidal gyroid fabrication is to first synthesise a batch of

chiral patchy particles capable of self-assembling single gyroid. This crystal can then be used as a template to assemble a single gyroid crystal of opposing chirality from more simplistic achiral particles. If this template crystal can then be disassembled and recovered, then essentially only one batch of chiral particles is required to self-assemble single colloidal gyroid crystals. A possible method of releasing the templated crystal is to introduce labile linker groups to the patch coatings of the chiral particles, such that the coatings of the template particle patches can be chemically or photochemically cleaved – resulting in a disassembly of the template crystal.

Chapter Seven

Summary and Outlook

The primary goal of this thesis was to investigate the targeted self-assembly of a single gyroid structure from colloidal building blocks. A single gyroid structure constructed on the colloidal scale is a highly attractive prospect as a 3D photonic crystal which operates in the visible region [30]. Such a material – though there is currently no efficient fabrication means [92] – has a wide range of applications as a chiral photonic crystal and metamaterial at optical frequencies [92–94]. The flexibility provided by patchy particles through control over various attributes such as, patch size, shape, number, orientation, and interaction, yields a wide design space for building blocks [40, 45] capable of stabilising diverse structures [66, 67]. This sets the context to explore potential self-assembly routes to single gyroid from patchy particles.

Chapter 3 presents our reverse engineering approach, which proposes a transformation of the single network gyroid structure into single gyroid crystal structures built from discrete synthetically available patchy spheres. Crystal structure prediction for triblock patchy particles identifies the "single colloidal gyroid" structure, and a library of isoenergetic competing trimer-based colloidal crystal structures. It is worth noting that a gyroid structure was not reported in a previous study into the phase behaviour of trivalent patchy particles

[66]. An investigation into the self-assembly behaviour of these triblock patchy particles with two equal-size circular patches reveals that, although patches can be optimised to form the required trigonal bonding motif, they form stacked kagome planes instead of the colloidal gyroid target. The formation of trigonal units, 6-membered rings, and shallow inter-trimer dihedral angles is identified as key to the self-assembly of the kagome structure.

Chapter 4 establishes a synthetically reasonable [62, 63] particle design consisting of two rectangular patches, the relative orientations of which encode inter-trimer dihedral angle selection into the particles. An effective pair potential capable of describing the interactions between these designer patchy particles with rectangular patches is then developed, based on the principles of the widely used Kern-Frenkel [104]. This is then used to validate the design principles behind the dihedral angle selection, and the self-assembled structures obtained from particles with various patch skew angles are explored. We envision the modified Kern-Frenkel potential developed here to find use in investigating the self-assembly behaviour of particles with non-circular patches, both in line with and in an attempt to motivate synthetic advances.

Chapter 5 builds on the design principles behind achieving dihedral angle selection, and establishes two distinct self-assembly routes to enantiomorphic single colloidal gyroid crystals *in silico*. The first route employs spherical particles with two attractive rectangular patches, where each patch is predisposed to form trigonal units and the patches are oriented such that inter-trimer dihedral angles are enforced to form at the ideal gyroid angles (70.5° or 109.5°). The second route also implements inter-trimer dihedral angle selection but with four circular patches instead, where each rectangular patch can be thought of as being replaced by a pair of circular patches. In both cases, the key here is that the dihedral angle selection essentially removes competing trimer-based structures from the energy landscape. In summary, the critical aspects for programming the self-assembly of single colloidal gyroid from patchy particles are: allowing for the patch-patch contacts required to stabilise the

target crystal; whilst sufficiently restricting inter-trimer dihedral angles (in order to suppress competing structures); and efficiently assembling trigonal units (so as to avoid kinetic traps). The two particle designs established here are both synthetically reasonable [43, 63], and we anticipate these results to drive any synthetic advancements required for the cost-effective and scalable fabrication of chiral 3D photonic crystals, which operate in the visible region. The extensive Monte Carlo simulations performed here demonstrate a wide parameter space for the enantiomorphic crystallisation of single colloidal gyroid, and it is established that an appropriate selection of target patch parameters yields an impressive tolerance for patch dispersity in both coverage and orientation. This is critical for the prospect of experimental realisation, since some degree of imprecision and polydispersity is inevitable.

Having demonstrated routes to enantiomorphic single colloidal gyroid, Chapter 6 explores routes to double colloidal gyroid using the rectangular patchy system. It is demonstrated that a racemic mixture of the chiral single gyroid forming building blocks can stabilise a double colloidal gyroid crystal. However, this simple racemic mixture alone is insufficient to self-assemble said crystal (within the length of the trajectories simulated) due to the entropy cost associated with de-mixing the particles. Two modifications to the interactions are proposed, in order to provide a driving-force for the de-mixing of particles of opposite handedness, and both are shown to result in the self-assembly of a double colloidal gyroid crystal *in silico*. The first modification involves a racemic mixture in which the interactions between particles of opposing chirality are "switched off". Experimentally this can be achieved *via* the use of DNA-mediated interactions with appropriate DNA sequences [117]. The alternative system proceeds *via* a hierarchical self-assembly approach [76, 82, 85], in which patches belonging to particles of one chirality interact more strongly than patches on particles of the opposing chirality, breaking the assembly down into two stages. These two systems require further investigation in order to ascertain the critical amount of bias towards de-mixing required to result in double colloidal gyroid crystallisation, i.e., how much

residual mixed interactions, and what ratio of patch strength hierarchy, fails to result in crystallisation?

Finally, particles with two trimer-forming circular patches dispersed within a template single gyroid crystal, are shown to self-assemble into a single colloidal gyroid crystal of opposing handedness to the template. This is in contrast to the self-assembly of the same particles in absence of the template crystal, which are shown to form kagome planes in Chapter 3. This templated formation of a single colloidal gyroid crystal, from simpler patchy particles with an achiral patch arrangement has potential applications in the fabrication of single colloidal gyroid crystals. The chiral particles required for self-assembly in absence of a template are much more challenging to synthesise than the relatively simplistic particles with circular patches [64], therefore a possible method of scaling-up and reducing the cost of single colloidal gyroid fabrication is to first synthesise a batch of chiral patchy particles capable of self-assembling into single colloidal gyroid. This crystal can then template the self-assembly of a single gyroid crystal of opposing chirality from achiral circular patchy particles. The disassembly and recovery of the template crystal then essentially results in only one batch of chiral particles being required for the self-assembly of single colloidal gyroid crystals. A possible method of releasing the templated crystal is to introduce labile linker functionality into the patch coatings of the chiral particles, such that the coatings can selectively be chemically or photochemically cleaved resulting in disassembly.

References

1. *colloidal* in *The IUPAC Compendium of Chemical Terminology* (International Union of Pure and Applied Chemistry (IUPAC), 2006).
2. Brown, R. XXVII. A brief account of microscopical observations made in the months of June, July and August 1827, on the particles contained in the pollen of plants; and on the general existence of active molecules in organic and inorganic bodies. *The Philosophical Magazine* **4,** 161–173 (1828).
3. Einstein, A. Über die von der molekularkinetischen Theorie der Wärme geforderte Bewegung von in ruhenden Flüssigkeiten suspendierten Teilchen. *Annalen der Physik* **322,** 549–560 (1905).
4. R., E. Brownian Movement and Molecular Reality. *Nature* **86,** 105–105 (1911).
5. Perrin, J. B. in *Physics 1922–1941* 133–166 (Elsevier, 2013).
6. Poon, W. Colloids as Big Atoms. *Science* **304,** 830–831 (2004).
7. Harland, J. L. & van Megen, W. Crystallization kinetics of suspensions of hard colloidal spheres. *Physical Review E* **55,** 3054–3067 (1997).
8. Tan, P., Xu, N. & Xu, L. Visualizing kinetic pathways of homogeneous nucleation in colloidal crystallization. *Nature Physics* **10,** 73–79 (2013).
9. Anderson, V. J. & Lekkerkerker, H. N. W. Insights into phase transition kinetics from colloid science. *Nature* **416,** 811–815 (2002).

10. Poon, W. C. Colloidal Glasses. *MRS Bulletin* **29,** 96–99 (2004).

11. Weeks, E. R., Crocker, J. C., Levitt, A. C., Schofield, A. & Weitz, D. A. Three-Dimensional Direct Imaging of Structural Relaxation Near the Colloidal Glass Transition. *Science* **287,** 627–631 (2000).

12. Whitesides, G. M. & Grzybowski, B. Self-Assembly at All Scales. *Science* **295,** 2418–2421 (2002).

13. Cademartiri, L. & Bishop, K. J. M. Programmable self-assembly. *Nature Materials* **14,** 2–9 (2014).

14. Boles, M. A., Engel, M. & Talapin, D. V. Self-Assembly of Colloidal Nanocrystals: From Intricate Structures to Functional Materials. *Chemical Reviews* **116,** 11220–11289 (2016).

15. Pusey, P. N. & van Megen, W. Phase behaviour of concentrated suspensions of nearly hard colloidal spheres. *Nature* **320,** 340–342 (1986).

16. Wood, W. W. & Jacobson, J. D. Preliminary Results from a Recalculation of the Monte Carlo Equation of State of Hard Spheres. *The Journal of Chemical Physics* **27,** 1207–1208 (1957).

17. Hoover, W. G. & Ree, F. H. Melting Transition and Communal Entropy for Hard Spheres. *The Journal of Chemical Physics* **49,** 3609–3617 (1968).

18. Alder, B. J. & Wainwright, T. E. Phase Transition for a Hard Sphere System. *The Journal of Chemical Physics* **27,** 1208–1209 (1957).

19. Frenkel, D. Entropy-driven phase transitions. *Physica A: Statistical Mechanics and its Applications* **263,** 26–38 (1999).

20. He, Y., Olivier, B. & Ackerson, B. J. Morphology of Crystals Made of Hard Spheres. *Langmuir* **13,** 1408–1412 (1997).

21. Woodcock, L. V. Entropy difference between the face-centred cubic and hexagonal close-packed crystal structures. *Nature* **385,** 141–143 (1997).

22. Rocklin, D. Z. & Mao, X. Self-assembly of three-dimensional open structures using patchy colloidal particles. *Soft Matter* **10,** 7569–7576 (2014).

23. Guo, S. *et al.* Research status and development trend of three-dimensional colloidal crystals. *Journal of Industrial and Engineering Chemistry* **96,** 34–58 (2021).

24. Aryana, K. & Zanjani, M. B. Diamond family of colloidal supercrystals as phononic metamaterials. *Journal of Applied Physics* **123,** 185103 (2018).

25. Stahley, J. B. & Zanjani, M. B. Multifarious colloidal structures: new insight into ternary and quadripartite ordered assemblies. *Nanoscale* **13,** 16554–16563 (39 2021).

26. Joannopoulos, J. D., Johnson, S. G., Winn, J. N. & Meade, R. D. *Photonic Crystals: Molding the Flow of Light - Second Edition* (2008).

27. Men, H., Lee, K. Y. K., Freund, R. M., Peraire, J. & Johnson, S. G. Robust Topology Optimization of Three-Dimensional Photonic-Crystal Band-Gap Structures. *Opt. Express* **22,** 22632–22648 (2014).

28. Han, L. *1D Photonic Crystals: Principles and Applications in Silicon Photonics* (InTech, 2018).

29. Wang, X., Li, S., Cheng, T. & Li, J. Overview of photonic devices based on functional material-integrated photonic crystal fibers. *Journal of Physics D: Applied Physics* **55,** 273001 (2022).

30. Von Freymann, G., Kitaev, V., Lotsch, B. V. & Ozin, G. A. Bottom-up assembly of photonic crystals. *Chem. Soc. Rev.* **42,** 2528–2554 (2013).

31. Deparis, O., Mouchet, S. R. & Su, B.-L. Light harvesting in photonic crystals revisited: why do slow photons at the blue edge enhance absorption? *Physical Chemistry Chemical Physics* **17,** 30525–30532 (2015).

32. Collins, G. *et al.* 2D and 3D photonic crystal materials for photocatalysis and electrochemical energy storage and conversion. *Science and Technology of Advanced Materials* **17,** 563–582 (2016).

33. Nair, R. V. & Vijaya, R. Photonic crystal sensors: An overview. *Progress in Quantum Electronics* **34,** 89–134 (2010).

34. Keil, R. *et al.* All-optical routing and switching for three-dimensional photonic circuitry. *Scientific Reports* **1** (2011).

35. Robinson, S. & Balaji, V. in *Micro- and Nanotechnology Enabled Applications for Portable Miniaturized Analytical Systems* 217–258 (Elsevier, 2022).

36. Chutinan, A. & Noda, S. Spiral three-dimensional photonic-band-gap structure. *Physical Review B* **57,** R2006–R2008 (1998).

37. Maldovan, M., Urbas, A. M., Yufa, N., Carter, W. C. & Thomas, E. L. Photonic Properties of Bicontinuous Cubic Microphases. *Phys. Rev. B* **65,** 165123 (2002).

38. Mao, X., Chen, Q. & Granick, S. Entropy favours open colloidal lattices. *Nature Materials* **12,** 217–222 (2013).

39. Cates, M. E. Entropy stabilizes open crystals. *Nature Materials* **12,** 179–180 (2013).

40. Glotzer, S. C. & Solomon, M. J. Anisotropy of building blocks and their assembly into complex structures. *Nature Materials* **6,** 557–562 (2007).

41. Pawar, A. B. & Kretzschmar, I. Fabrication, Assembly, and Application of Patchy Particles. *Macromolecular Rapid Communications* **31,** 150–168 (2010).

42. Bianchi, E., Blaak, R. & Likos, C. N. Patchy colloids: state of the art and perspectives. *Physical Chemistry Chemical Physics* **13,** 6397 (2011).

43. Chen, Q. *et al.* Triblock Colloids for Directed Self-Assembly. *J. Am. Chem. Soc.* **133,** 7725–7727 (2011).

44. Takei, H. & Shimizu, N. Gradient Sensitive Microscopic Probes Prepared by Gold Evaporation and Chemisorption on Latex Spheres. *Langmuir* **13,** 1865–1868 (1997).

45. Chen, Q., Yan, J., Zhang, J., Bae, S. C. & Granick, S. Janus and Multiblock Colloidal Particles. *Langmuir* **28,** 13555–13561 (2012).

46. Yi, G.-R., Pine, D. J. & Sacanna, S. Recent progress on patchy colloids and their self-assembly. *Journal of Physics: Condensed Matter* **25,** 193101 (2013).

47. Ravaine, S. & Duguet, E. Synthesis and assembly of patchy particles: Recent progress and future prospects. *Current Opinion in Colloid &amp Interface Science* **30,** 45–53 (2017).

48. Hueckel, T., Hocky, G. M. & Sacanna, S. Total synthesis of colloidal matter. *Nature Reviews Materials* **6,** 1053–1069 (2021).

49. Li, W. *et al.* Colloidal molecules and patchy particles: complementary concepts, synthesis and self-assembly. *Chemical Society Reviews* **49,** 1955–1976 (2020).

50. Cui, F., Marbach, S., Zheng, J. A., Holmes-Cerfon, M. & Pine, D. J. Comprehensive view of microscopic interactions between DNA-coated colloids. *Nature Communications* **13,** 2304 (2022).

51. Samanta, D., Zhou, W., Ebrahimi, S. B., Petrosko, S. H. & Mirkin, C. A. Programmable Matter: The Nanoparticle Atom and DNA Bond. *Advanced Materials* **34,** 2107875 (2022).

52. Laramy, C. R., O'Brien, M. N. & Mirkin, C. A. Crystal engineering with DNA. *Nature Reviews Materials* **4,** 201–224 (2019).

53. Macfarlane, R. J., Jones, M. R., Lee, B., Auyeung, E. & Mirkin, C. A. Topotactic Interconversion of Nanoparticle Superlattices. *Science* **341,** 1222–1225 (2013).

54. Wang, Y. *et al.* Crystallization of DNA-coated colloids. *Nature Communications* **6,** 7253 (2015).

55. Ducrot, É., He, M., Yi, G.-R. & Pine, D. J. Colloidal alloys with preassembled clusters and spheres. *Nature Materials* **16,** 652–657 (2017).

56. Wang, Y. *et al.* Synthetic Strategies Toward DNA-Coated Colloids that Crystallize. *Journal of the American Chemical Society* **137,** 10760–10766 (2015).

57. Wang, Y. *et al.* Colloids with valence and specific directional bonding. *Nature* **491,** 51–55 (2012).

58. Feng, L., Dreyfus, R., Sha, R., Seeman, N. C. & Chaikin, P. M. DNA Patchy Particles. *Advanced Materials* **25,** 2779–2783 (2013).

59. Gong, Z., Hueckel, T., Yi, G.-R. & Sacanna, S. Patchy particles made by colloidal fusion. *Nature* **550,** 234–238 (2017).

60. Romano, F. & Sciortino, F. Patterning Symmetry in the Rational Design of Colloidal Crystals. *Nat. Commun.* **3,** 975 (2012).

61. He, M., Gales, J. P., Shen, X., Kim, M. J. & Pine, D. J. Colloidal Particles with Triangular Patches. *Langmuir* **37,** 7246–7253 (2021).

62. Pawar, A. B. & Kretzschmar, I. Patchy Particles by Glancing Angle Deposition. *Langmuir* **24,** 355–358 (2008).

63. Pawar, A. B. & Kretzschmar, I. Multifunctional Patchy Particles by Glancing Angle Deposition. *Langmuir* **25,** 9057–9063 (2009).

64. Chen, Q., Bae, S. C. & Granick, S. Directed Self-Assembly of a Colloidal Kagome Lattice. *Nature* **469,** 381–384 (2011).

65. Vissers, T., Preisler, Z., Smallenburg, F., Dijkstra, M. & Sciortino, F. Predicting crystals of Janus colloids. *The Journal of Chemical Physics* **138,** 164505 (2013).

66. Romano, F., Sanz, E., Tartaglia, P. & Sciortino, F. Phase diagram of trivalent and pentavalent patchy particles. *Journal of Physics: Condensed Matter* **24,** 064113 (2012).

67. Reinhart, W. F. & Panagiotopoulos, A. Z. Equilibrium crystal phases of triblock Janus colloids. *The Journal of Chemical Physics* **145,** 094505 (2016).

68. Kim, Y.-J., Moon, J.-B., Hwang, H., Kim, Y. S. & Yi, G.-R. Advances in Colloidal Building Blocks: Toward Patchy Colloidal Clusters. *Advanced Materials,* 2203045 (2022).

69. Noya, E. G., Vega, C., Doye, J. P. K. & Louis, A. A. The stability of a crystal with diamond structure for patchy particles with tetrahedral symmetry. *The Journal of Chemical Physics* **132,** 234511 (2010).

70. Romano, F., Sanz, E. & Sciortino, F. Phase diagram of a tetrahedral patchy particle model for different interaction ranges. *The Journal of Chemical Physics* **132,** 184501 (2010).

71. Zhang, Keys, A. S., Chen, T. & Glotzer, S. C. Self-Assembly of Patchy Particles into Diamond Structures through Molecular Mimicry. *Langmuir* **21,** 11547–11551 (2005).

72. Romano, F., Sanz, E. & Sciortino, F. Crystallization of tetrahedral patchy particles in silico. *The Journal of Chemical Physics* **134,** 174502 (2011).

73. Noya, E. G., Zubieta, I., Pine, D. J. & Sciortino, F. Assembly of clathrates from tetrahedral patchy colloids with narrow patches. *The Journal of Chemical Physics* **151,** 094502 (2019).

74. Ngo, T. T., Liddell, C. M., Ghebrebrhan, M. & Joannopoulos, J. D. Tetrastack: Colloidal diamond-inspired structure with omnidirectional photonic band gap for low refractive index contrast. *Applied Physics Letters* **88,** 241920 (2006).

75. Ho, K. M., Chan, C. T. & Soukoulis, C. M. Existence of a Photonic Gap in Periodic Dielectric Structures. *Phys. Rev. Lett.* **65,** 3152–3155 (1990).

76. Rao, A. B. *et al.* Leveraging Hierarchical Self-Assembly Pathways for Realizing Colloidal Photonic Crystals. *ACS Nano* **14,** 5348–5359 (2020).

77. Patra, N. & Tkachenko, A. V. Programmable self-assembly of diamond polymorphs from chromatic patchy particles. *Physical Review E* **98** (2018).

78. Mahynski, N. A., Rovigatti, L., Likos, C. N. & Panagiotopoulos, A. Z. Bottom-Up Colloidal Crystal Assembly with a Twist. *ACS Nano* **10,** 5459–5467 (2016).

79. Russo, J. *et al.* SAT-assembly: a new approach for designing self-assembling systems. *Journal of Physics: Condensed Matter* **34,** 354002 (2022).

80. Rovigatti, L. *et al.* A simple solution to the problem of self-assembling cubic diamond crystals. *Nanoscale* **14,** 14268–14275 (2022).

81. Romano, F., Russo, J., Kroc, L. & Šulc, P. Designing Patchy Interactions to Self-Assemble Arbitrary Structures. *Physical Review Letters* **125,** 118003 (2020).

82. Neophytou, A., Manoharan, V. N. & Chakrabarti, D. Self-Assembly of Patchy Colloidal Rods into Photonic Crystals Robust to Stacking Faults. *ACS Nano* **15,** 2668–2678 (2021).

83. Frenkel, D. & Wales, D. J. Designed to yield. *Nature Materials* **10,** 410–411 (2011).

84. O'Brien, M. N., Jones, M. R. & Mirkin, C. A. The nature and implications of uniformity in the hierarchical organization of nanomaterials. *Proceedings of the National Academy of Sciences* **113,** 11717–11725 (2016).

85. Morphew, D., Shaw, J., Avins, C. & Chakrabarti, D. Programming Hierarchical Self-Assembly of Patchy Particles into Colloidal Crystals via Colloidal Molecules. *ACS Nano* **12,** 2355–2364 (2018).

86. Neophytou, A., Chakrabarti, D. & Sciortino, F. Facile self-assembly of colloidal diamond from tetrahedral patchy particles via ring selection. *Proceedings of the National Academy of Sciences* **118** (2021).

87. He, M. *et al.* Colloidal diamond. *Nature* **585,** 524–529 (2020).

88. Schoen, A. H. *Infinite Periodic Minimal Surfaces without Self-Intersections* tech. rep. NASA TN D-5541 (National Aeronautics and Space Administration, 1970).

89. Hyde, S. T., O'Keeffe, M. & Proserpio, D. M. A Short History of an Elusive Yet Ubiquitous Structure in Chemistry, Materials, and Mathematics. *Angew. Chem. Int. Ed.* **47,** 7996–8000 (2008).

90. Feng, X. *et al.* Seeing Mesoatomic Distortions in Soft-Matter Crystals of a Double-Gyroid Block Copolymer. *Nature* **575,** 175–179 (2019).

91. Lu, L., Fu, L., Joannopoulos, J. D. & Soljacić, M. Weyl Points and Line Nodes in Gyroid Photonic Crystals. *Nat. Photonics* **7,** 294–299 (2013).

92. Goi, E., Cumming, B. P. & Gu, M. Gyroid "srs" Networks: Photonic Materials Beyond Nature. *Advanced Optical Materials* **6,** 1800485 (2018).

93. Dolan, J. A. *et al.* Optical Properties of Gyroid Structured Materials: From Photonic Crystals to Metamaterials. *Adv. Optical Mater.* **3,** 12–32 (2015).

94. Turner, M. D. *et al.* Miniature Chiral Beamsplitter Based on Gyroid Photonic Crystals. *Nat. Photonics* **7,** 801–805 (2013).

95. Saranathan, V., Narayanan, S., Sandy, A., Dufresne, E. R. & Prum, R. O. Evolution of single gyroid photonic crystals in bird feathers. *Proceedings of the National Academy of Sciences* **118** (2021).

96. Sunada, T. Crystals that Nature might miss creating. *Notices Amer. Math. Soc,* 209–215 (2007).

97. Schuetrumpf, B. *et al.* Appearance of the single gyroid network phase in "nuclear pasta" matter. *Physical Review C* **91** (2015).

98. Fontell, K. Cubic Phases in Surfactant and Surfactant-Like Lipid Systems. *Colloid Polym. Sci.* **268,** 264–285 (1990).

99. Bates, F. S. & Fredrickson, G. H. Block Copolymers — Designer Soft Materials. *Phys. Today* **52(2),** 32–38 (1999).

100. Kutsumizu, S. Recent Progress in the Synthesis and Structural Clarification of Thermotropic Cubic Phases. *Isr. J. Chem.* **52,** 844–853 (2012).

101. Michielsen, K. & Stavenga, D. G. Gyroid Cuticular Structures in Butterfly Wing Scales: Biological Photonic Crystals. *J. R. Soc. Interface* **5,** 85–94 (2008).

102. Saranathan, V. *et al.* Structure, function, and self-assembly of single network gyroid ($I4_132$) photonic crystals in butterfly wing scales. *Proceedings of the National Academy of Sciences* **107,** 11676–11681 (2010).

103. Urbas, A., Maldovan, M., DeRege, P. & Thomas, E. Bicontinuous Cubic Block Copolymer Photonic Crystals. *Advanced Materials* **14,** 1850–1853 (2002).

104. Kern, N. & Frenkel, D. Fluid-Fluid Coexistence in Colloidal Systems with Short-Ranged Strongly Directional Attraction. *J. Chem. Phys.* **118,** 9882–9889 (2003).

105. Wales, D. J. & Doye, J. P. K. Global Optimization by Basin-Hopping and the Lowest Energy Structures of Lennard-Jones Clusters Containing up to 110 Atoms. *The Journal of Physical Chemistry A* **101,** 5111–5116 (1997).

106. Liu, D. C. & Nocedal, J. On the limited memory BFGS method for large scale optimization. *Mathematical Programming* **45,** 503–528 (1989).

107. Price, S. L. Predicting crystal structures of organic compounds. *Chemical Society Reviews* **43,** 2098–2111 (2014).

108. Prasad, I., Jinnai, H., Ho, R.-M., Thomas, E. L. & Grason, G. M. Anatomy of triply-periodic network assemblies: characterizing skeletal and inter-domain surface geometry of block copolymer gyroids. *Soft Matter* **14,** 3612–3623 (18 2018).

109. Rao Jammalamadaka, S. & Sengupta, A. *Topics in Circular Statistics* (World Scientific, Singapore, 2001).

110. Lechner, W. & Dellago, C. Accurate Determination of Crystal Structures Based on Averaged Local Bond Order Parameters. *J. Chem. Phys.* **129,** 114707 (2008).

111. Steinhardt, P. J., Nelson, D. R. & Ronchetti, M. Bond-Orientational Order in Liquids and Glasses. *Phys. Rev. B* **28,** 784–805 (1983).

112. ten Wolde, P. R., Ruiz-Montero, M. J. & Frenkel, D. Numerical Calculation of the Rate of Crystal Nucleation in a Lennard-Jones System at Moderate Undercooling. *J. Chem. Phys.* **104,** 9932–9947 (1996).

113. Xu, Z., Wang, L., Fang, F., Fu, Y. & Yin, Z. A Review on Colloidal Self-Assembly and their Applications. *Current Nanoscience* **12,** 725–746 (2016).

114. Duguet, É., Hubert, C., Chomette, C., Perro, A. & Ravaine, S. Patchy colloidal particles for programmed self-assembly. *Comptes Rendus Chimie* **19,** 173–182 (2016).

115. Damasceno, P. F., Engel, M. & Glotzer, S. C. Predictive Self-Assembly of Polyhedra into Complex Structures. *Science* **337,** 453–457 (2012).

116. Wang, Y. *et al.* Colloids with valence and specific directional bonding. *Nature* **491,** 51–55 (2012).

117. Rogers, W. B. & Crocker, J. C. Direct measurements of DNA-mediated colloidal interactions and their quantitative modeling. *Proceedings of the National Academy of Sciences* **108,** 15687–15692 (2011).

118. Van Blaaderen, A., Ruel, R. & Wiltzius, P. Template-directed colloidal crystallization. *Nature* **385,** 321–324 (1997).